Addis Ababa University
አዲስ አበባ ዩኒቨርሲቲ
Seek Wisdom, Elevate your Intellect and Serve Humanity

COLLEGE OF NATURAL AND COMPUTATIONAL SCIENCES

SCHOOL OF EARTH SCIENCES

GROUNDWATER POTENTIAL STUDY USING GEOPHYSICAL METHODS AROUND HARBU TOWN, SOUTH WOLLO, ETHIOPIA

A THESIS SUBMITTED TO SCHOOL OF EARTH SCIENCES IN PARTIAL FULFILMENT OF THE REQUIREMENTS FOR DEGREE OF MASTER OF SCIENCE IN APPLIED GEOPHYSICS

BY: AWOL MOHAMMED

ADVISOR: DR. MEBATESYON SHAWEL

CO-ADVISOR: DR. BEHAILU BIRHANU

JUNE, 2024

ADDIS ABABA, ETHIOPIA

DECLARATION

I affirm that the thesis entitled "**Groundwater potential study using geophysical methods around Harbu town, South Wollo, Ethiopia**" is my original work conducted under the supervision of Dr. Mebatseyon Shawel and Dr. Behailu Birhanu. I confirm that this thesis has not been previously submitted to any university or institution to obtain any degree. I further declare that all sources of materials used in this thesis have been properly acknowledged.

Name Awol Mohammed **Signature**_____ **Date** _____

Signature page

This is to certify that the thesis prepared by Awol Mohammed, entitled: "**Groundwater potential study using geophysical methods around Harbu town, South Wollo, Ethiopia**" and submitted in partial fulfillment of the requirements for the degree of Master of science in applied geophysics complies with the regulations of the university and meets the accepted standards for originality and quality.

Approved by examining committee:

Advisor

Dr. Mebatseyon Shawel		
Name	Signature	Date

Co-Advisor

Dr. Behailu Birhanu		
Name	Signature	Date

Internal examiner

Prof. Tigistu Haile		
Name	Signature	Date

External Examiner

Dr. Tilahun Azagegn		
Name	Signature	Date

Chair of School or Graduate Program coordinator

Abstract

This study was conducted in the Harbu area of the Amhara regional state, South Wollo Zone, north central Ethiopia. The present study aims to assess groundwater potential zones and aquifer characterization in the area. Vertical Electrical Sounding (VES) and magnetic methods were employed to achieve this objective. Using a Schlumberger arrangement, thirteen (13) VES points were collected with a PASI resistivity meter. Additionally, 230 magnetic data points were collected using G600 Proton Precession Magnetometer. The magnetic survey was conducted along an east-west orientation with intervals of 100 meters along each traverse. Diurnal and IGRF corrections were applied to isolate the magnetic field arising from subsurface geological units. Subsequently, the upward continuation technique was used to differentiate between shallow and deep-seated geological formations. Various maps were generated using Oasis Montaj software, including a residual anomaly map, a tilt derivative map, and an Euler deconvolution map. A low residual magnetic anomaly was observed toward the southeast and northwest parts of the research area. Euler 3D deconvolution maps indicated variations in the depth of contact within the study area. The 2D magnetic model along the profile revealed variations in sediment thickness. To illustrate vertical and horizontal variations in apparent resistivity across the study area, a sliced stacked map was created. Additionally, geoelectric sections were prepared to provide a quantitative interpretation of apparent resistivity by integrating borehole data and VES curve models. The pseudo-depth sections showed that the central part of the study area corresponds to low apparent resistivity. The geoelectric sections indicated that the central part is characterized by thick alluvial sediment and a deep basement. The relationship between transmissivity (T) and transverse resistance (TR) in the Harbu-Chefa graben was derived as: $T = 0.6239TR - 746.18$. This equation was used to extrapolate transmissivity and hydraulic conductivity of the study area.

Keywords: Aquifer characterization, apparent resistivity, Schlumberger arrangement, Transmissivity.

Acknowledgment

Above all, I extend my deepest gratitude to the Almighty Allah for granting me the strength and guidance to complete this thesis successfully.

Secondly, I am grateful to my advisor, Dr. Mebatseyon Shawel, for his precious guidance and insightful feedback throughout this journey. His comments and suggestions have been instrumental in shaping my understanding and approach to the thesis work. And also I would like to express my sincere gratitude to Dr. Behailu Birhanu for his help full guidance, support, and expertise throughout the preparation of this thesis.

I would like to extend my heartfelt thanks to all my friends and classmates for their encouragement and support, which played a significant role in enabling me to accomplish my tasks.

I am indebted to my family for their unforgettable support, both financially and morally, which has been a constant source of motivation and inspiration.

Lastly, I would like to express my sincere appreciation to the following institutions and organizations: Addis Ababa University, for providing the necessary facilities and resources for the successful completion of my specialization; Dilla University, for granting me the opportunity to take my second degree; the Geological Survey of Ethiopia, for providing invaluable secondary data; and the Amhara National Regional State Water, Irrigation, and Energy Bureau, for supplying essential borehole data.

Table of content

Contents

List of figures

List of tables

List of acronyms

EARS…….. East African Rift System

EFB……. …... Ethiopian Flood Basalt

FB……. ……...Flood Basalt

GPS……. ...… Geographic position System

IGRF……. …..International Geomagnetic Reference Field

MD…… ……...Magnetic declination

MER……. ……Main Ethiopian Rift

MI…… ……..…Magnetic Inclination

NE……..…North East

NNE…….....North North East

NW…… North West

SI …… …….....International System of unit

SSW……South South West

SE……. South West

SW……..South West

VES……Vertical Electrical Sounding

TDR…….Tilt Derivative

CHAPTER I

INTRODUCTION

1.1 Background

Groundwater systems are filled up by precipitation and surface water. On the other hand, groundwater feeds streams, lakes, and oceans. Furthermore, it returns to the atmosphere due to evapotranspiration (Shiklomanov & Rodda, 2003). Groundwater is a vital renewable natural resource that has great significance during climate change (Chatterjee et al., 2010). Aquifers provide drinking water to at least 50% of the world's population and 43% of the water used for irrigation (Diaz & Martinez, 2019). Surface and groundwater resources can be combined to meet specific water needs more efficiently and economically than using them separately. They are important for irrigation, domestic, and industrial purposes. Moreover, groundwater provides additional benefits, such as minimizing drought consequences and reducing vulnerability to contaminants (Sahuquillo, 2009).

The groundwater flow is mostly controlled by different factors, such as geological features like joints and faults, texture of sediment, primary porosity, and topography. The orientations of the geological structures also affect the flow direction (Senthilkumar et al., 2015). Similarly, the fracture density, thickness of the weathered rocks, and thickness of the porous sediments determine how much groundwater is kept in the reservoir or aquifer (Ojoawo & Adagunodo, 2023). Primary porosity, which regulates groundwater flow and storage capacity, is maintained in sedimentary rocks. Alluvial deposits (gravel and sand), sandstone, and limestone are the main aquifers in sedimentary terrain. However, in basements and volcanic terrains, secondary porosities are very important in controlling the hydraulic conductivity and storage capacity of the reservoirs (Tilahun Azagegn et al., 2015; Vsevolozhsky, 2003).

Furthermore, the availability and flow of groundwater are contained in the subsurface geological material. It is necessary to conduct different exploration techniques to identify the groundwater potential zones. Geophysical investigation is one of the techniques to explore groundwater resources by determining anomalies in the physical properties of the earth like density, velocity, conductivity, resistivity, and magnetic susceptibility (Griffiths & King, 2013). According to Chandra et al. (2008), groundwater studies apply geophysical methods, such as vertical electrical

sounding, magnetic, and seismic, to map the depth of firm rocks, determine aquifer geometry, and quantify the thickness of the aquifer.

For the management and sustainability of groundwater resources, understanding of aquifer properties like transmissivity, storability, and hydraulic conductivity are crucial (Soupios et al., 2007). Estimating the aquifer parameters like transmissivity and hydraulic conductivity through pumping tests can be both time consuming and costly. However, geophysical methods offer a faster and more cost-effective alternative for estimating these aquifer parameters. The VES survey is very important for assessing aquifer parameters through numerical modeling (Dor et al., 2011). This study conducted a geophysical-based investigation to assess the groundwater potential zones by knowing the depth of the aquifer, identifying the thickness of alluvial sediment, delineating the geological structure, and estimating the aquifer parameters.

1.2 Previous work

While geophysical-based investigations specifically targeting groundwater potential assessment and aquifer characterization in the research area have not been conducted, several relevant studies have been carried out in other regions. As stated by Esubalew Yehualaw et al. (2023), magnetic and VES methods were utilized to map groundwater potential in the Hosanna area, situated at the western margin of the central main Ethiopian Rift. In another study by (Alzahrani et al. (2022) the electrical resistivity method was employed to detect near-surface groundwater potential zones in Riyadh City, Saudi Arabia. The researchers utilized the VES technique for conducting the electrical resistivity investigation. Additionally, El Makrini et al. (2022) utilized the VES technique to map the potential aquifer of the Guigous Plain, Morocco. Furthermore Akhter & Hasan (2016) employed geophysical methods along with pumping test data to determine aquifer parameters. They conducted 48 geoelectric investigations (VES) using Schlumberger arrangement, with seven soundings at borehole sites. Resistivity data was processed using software packages and transverse unit resistance (R) was calculated. The authors determined the transmissivity value from a pumping test of seven wells, establishing a regression equation to determine the relationship between the values and the transverse unit. Similarly, Onawola et al. (2021) only utilized the geophysical method to determine aquifer parameters. Geophysical data (electrical resistivity) were collected with a Pz-02 resistivity meter, employing the VES method. Thickness and depth were generated for different geoelectric layers using the

IPI2WIN software. The authors calculated the Dar-Zarrouk parameter from geoelectric parameters and established the relationship between transmissivity and transverse resistance.

1.3 Description of the study area

1.3.1 Location and Accessibility

The research area is situated in the Amhara regional state of the south Wollo zone administration about 253 km from Addis Ababa (Fig. 1.1). The area is geographically bounded between 580000–590000 m easting and 1200000–1220000 m northing. The study area covers approximately 32.7 square kilometers. The target area is accessed by the main asphalt road along Addis Ababa to Dessie main road.

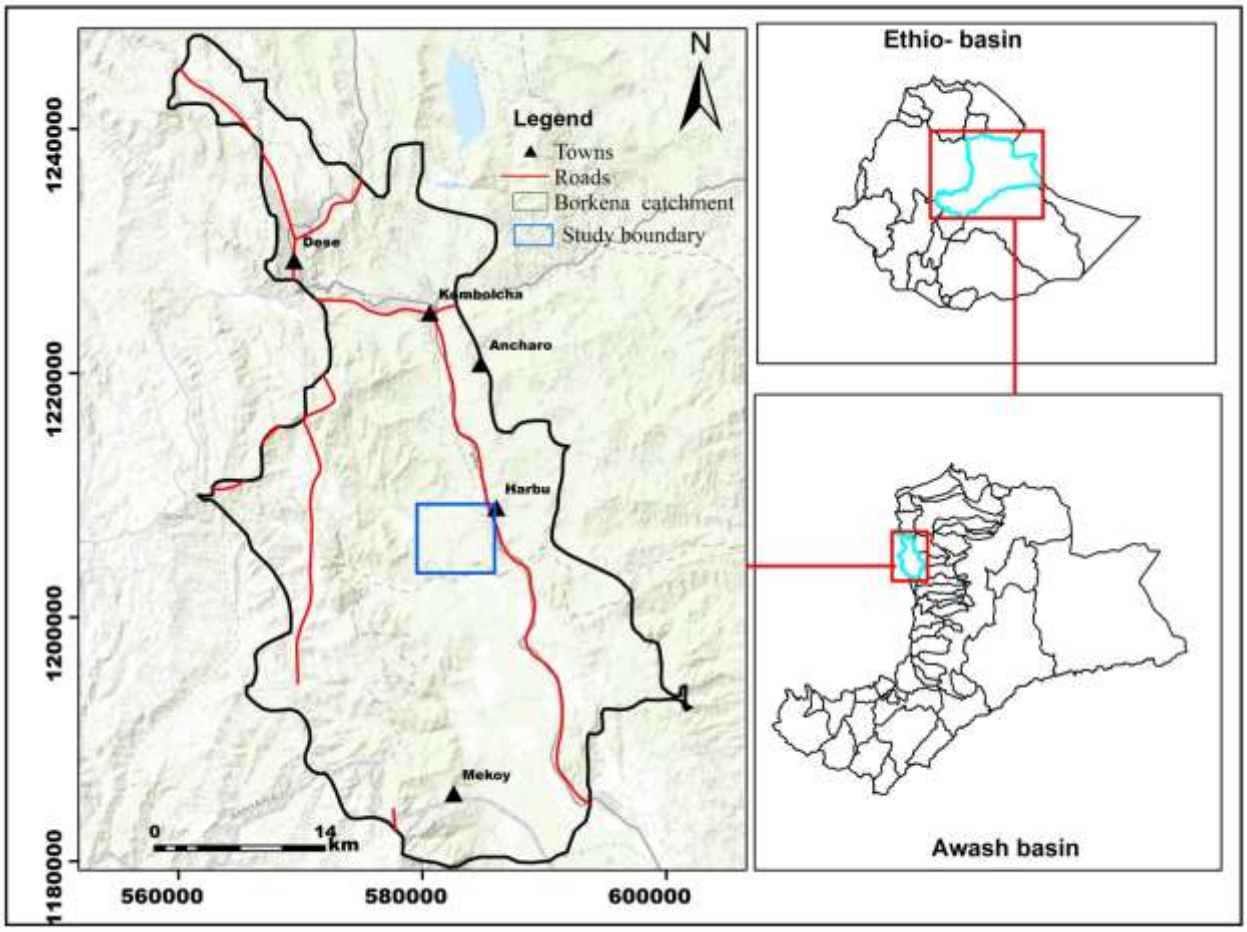

Figure 1.1: Location map of the study area**.**

1.3.2 Physiography

The Borkena catchment is situated near the western Afar margin, a region characterized by extended grabens and escarpments. In the Borkena catchment, the elevation ranges from 1400 m near Kemise in the southeast to 3419 m in the northern and northwestern part of the study area (Fig. 1.2). The study area is situated within the floor of Harbu–Kemise graben, surrounded by mountains to the west and east. The elevation decreases from 2600 m in the western and 2400 in the eastern mountain to 1414m in the graben floor (Fig. 1.2).

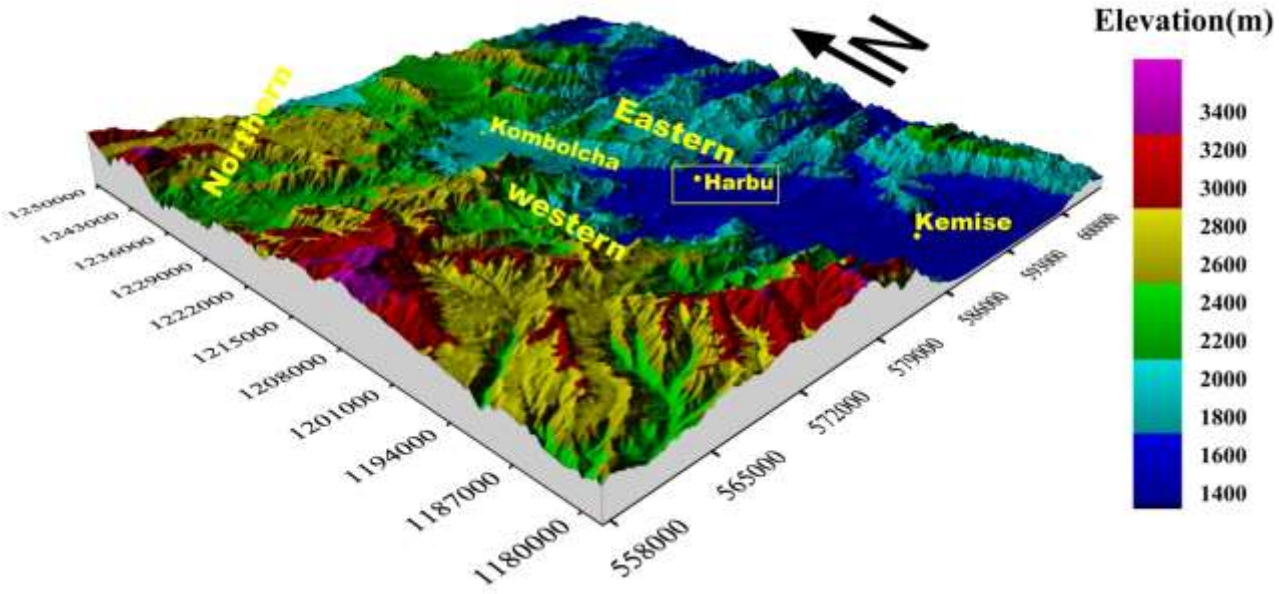

Figure 1.2: Physiography map of the Borkena catchment.

1.3.3 Drainage

The Harbu‑Kemise graben is surrounded by mountains and escarpments. Many tributaries drain from Dessie, Ancharo, and Mekoy areas toward the Borkena River, which dissects Kombolcha town and moves through Harbu and Kemise toward the Awash River. The streams originate from the surrounding mountains, with the majority being perennial while some tributary streams are intermittent. The drainage system in the study area is primarily influenced by the topography of the area, in which all the streams are flowing from high elevated area to lowlands. The drainage arrangement of the area is characterized by a dendritic pattern (Fig. 1.3).

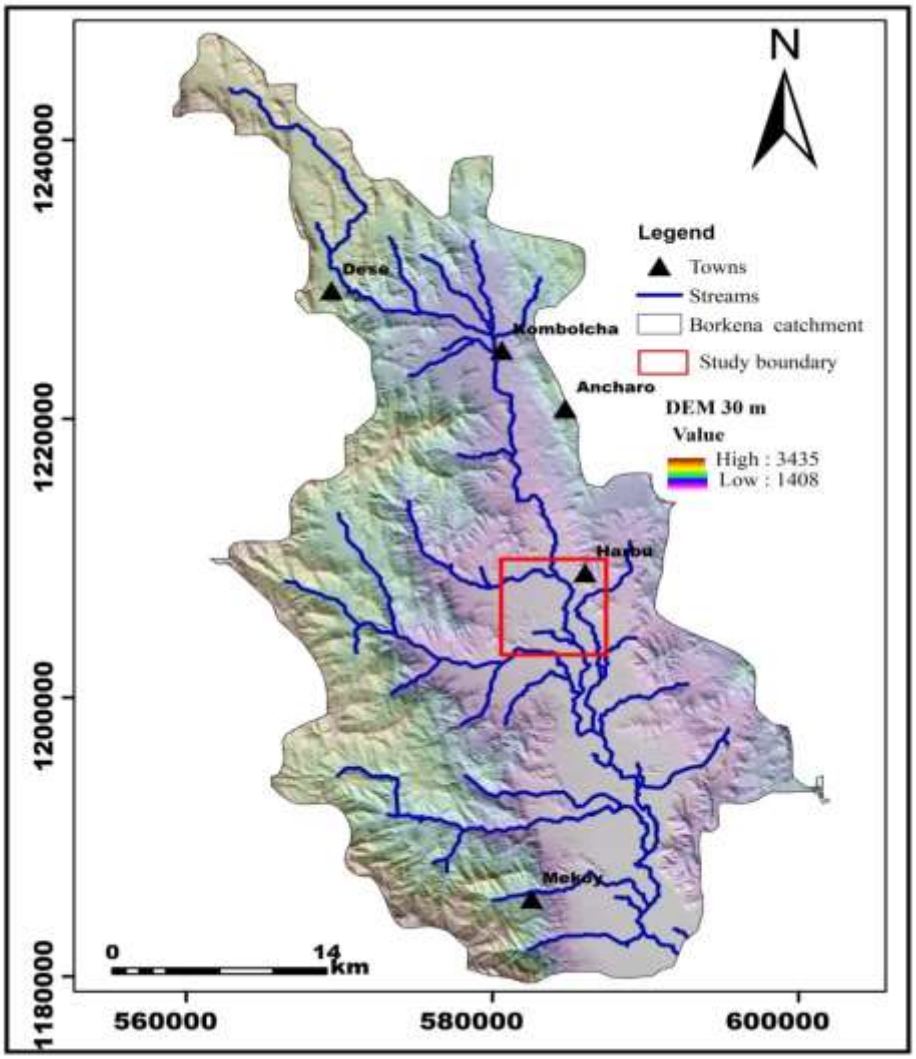

Figure 1.3: Drainage map of the Borkena catchment.

1.3.4 Climate

Precipitation: The precipitation patterns in the research area exhibit significant variation throughout the year, particularly between the summer and dry seasons. As illustrated in Fig.1.4 a, the monthly mean precipitation demonstrates distinct fluctuations across different months.

During the summer months, such as August, the study area experiences higher levels of precipitation. In August, the monthly mean precipitation reaches approximately 252 mm, indicating an increase in rainfall intensity. This high precipitation during the summer season contributes to the replenishment of water resources. Conversely, the dry season, represented by January, is characterized by significantly reduced precipitation levels. In January, the study area records its lowest monthly mean precipitation, with 15.5 mm.

Temperature: The monthly temperature in the study area shows variations from month to month. As shown in Fig. 1.5, different temperature values are observed across different months. During March, April, May, and September, the study area experiences its highest temperatures. These months are characterized by warm weather conditions, with temperatures reaching their peak levels. Conversely, December and October represent the cooler temperatures in the study area, with the lowest recorded temperatures observed during these periods.

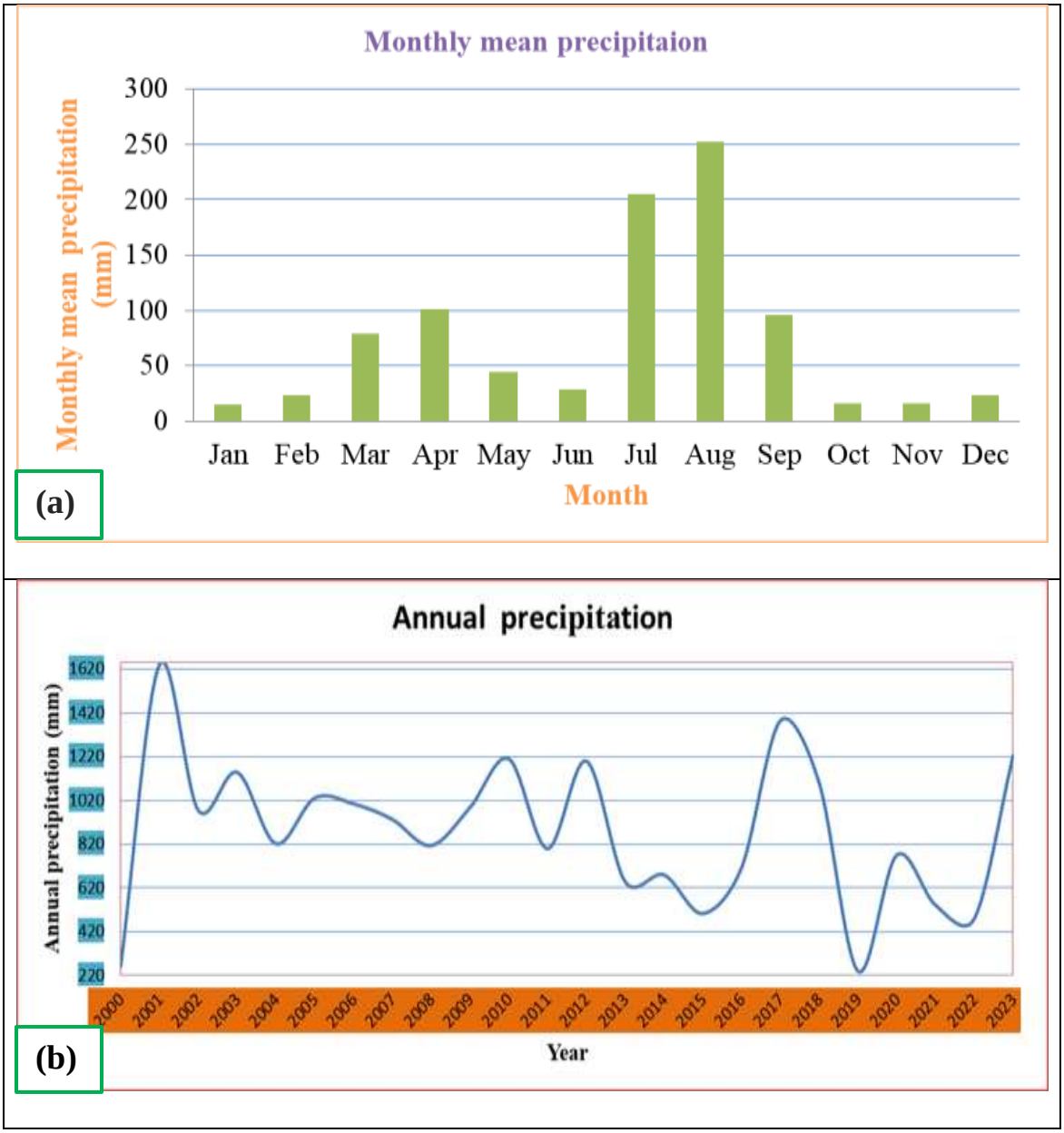

Figure 1.4: Monthly mean and annual precipitation of Harbu station over the years 2000 to 2023.

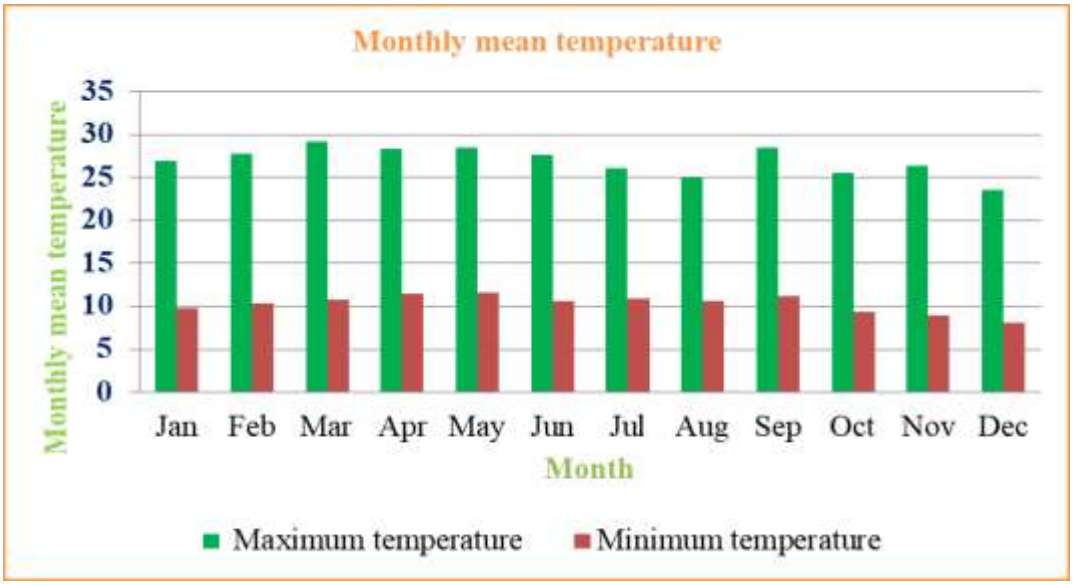

Figure 1.5: Monthly mean temperature of Harbu station over the years 2000 to 2021.

1.4 Statement of the problem

The hydraulic properties, the nature of the geological structure, and the geomorphology of the area control the groundwater flow and occurrence (Melkamu Adimaw et al., 2020). So far, various researchers have conducted hydrogeological-based investigations in the research area, considering surface parameters such as rainfall, slope, recharge, evapotranspiration, fracture density, land use, land cover, surface water (springs and rivers), pumping test data and surface structures (Getachew Tsigie, 2015; Gobezie Wallelegn et al., 2023; Hasen Hussien et al., 2022; Rigbe Tsegaye, 2021). Moreover, previous studies have not studied subsurface geological structures which are critical for groundwater availability and flow, the thickness of alluvial sediment that is important as a reservoir, and the estimation of aquifer parameters using geophysical data. This study aims to address these issues using VES and magnetic methods. The present work includes assessing groundwater potential zones by determining the subsurface geological structures, determining the thickness of sediment, and estimating aquifer parameters.

1.5 Objectives of the study

1.5.1 General objective

The main objective of the study is to examine the groundwater potential zones and aquifer characteristics in the northern part of a marginal graben around Harbu Town, South Wollo Zone.

1.5.2 Specific objectives

The specific objectives of the study are:

- To identify the subsurface lithological units.
- To determine the depth of the potential aquifer.
- To delineate the subsurface structures.
- To estimate the aquifer parameters (hydraulic conductivity and transmissivity) using a dar-zrrouk parameter.

1.6 Materials and methods

1.6.1 Materials

To fulfill the study objectives, various materials were utilized. Geophysical equipment such as the Pasi Resistivity meter and Proton Precession Magnetometer were employed for data collection. Additionally, digital tools including ArcGIS 10.7.1, Oasis Montaj 8.4, Global Mapper, WINRESIST, IPI2win, Microsoft Excel, Google Earth Pro, and Surfer-16 were utilized for data analysis and visualization.

1.6.2 Methods

Several authors including Akhter & Hasan (2016); El Makrini et al. (2022) and Esubalew Yehualaw et al. (2023) were used VES and magnetic geophysical methods to investigate groundwater potential. Similarly, this research applied VES and magnetic geophysical methods to comprehensively determine groundwater potential zones by knowing the depth of the aquifer, identifying the thickness of alluvial sediment, delineating the geological structure, and estimating the aquifer parameters. Each of the methods adopted for the present study is well explained in chapter III. To achieve the objectives of the present study, three different phases of procedures were employed:

A. During the pre-field work

In this phase, existing data from various sources, including hydrogeological and geophysical data, were collected. This encompassed borehole data, previous pumping tests, VES, and magnetic data. Additionally, field designs for data acquisition were prepared, and previous works were reviewed to establish a foundational understanding of the geological and hydrogeological condition of the area.

B. Fieldwork

In the fieldwork phase, comprehensive surface observations were conducted along chosen traverses to identify rock units, geological structures. VES survey was conducted using the pasi resistivity meter along selected profiles, while magnetic field data were collected using G600 proton precession magnetometers along eight profiles. Crucial information such as GPS data for each measurement and field notes were recorded.

C. Post fieldwork

Following the fieldwork phase, post-fieldwork activities were begun. This involved the processing and analysis of the collected geophysical raw data utilizing software tools such as WinResist, IPI2win, Microsoft Excel, Oasis Montaj 8.4, and Surfer-16. The processed and analyzed data were presented in the forms of VES curves, profiles, contour maps, and 2D sections. Following the presentation of results, the discussion, interpretation, and conclusion were carried out.

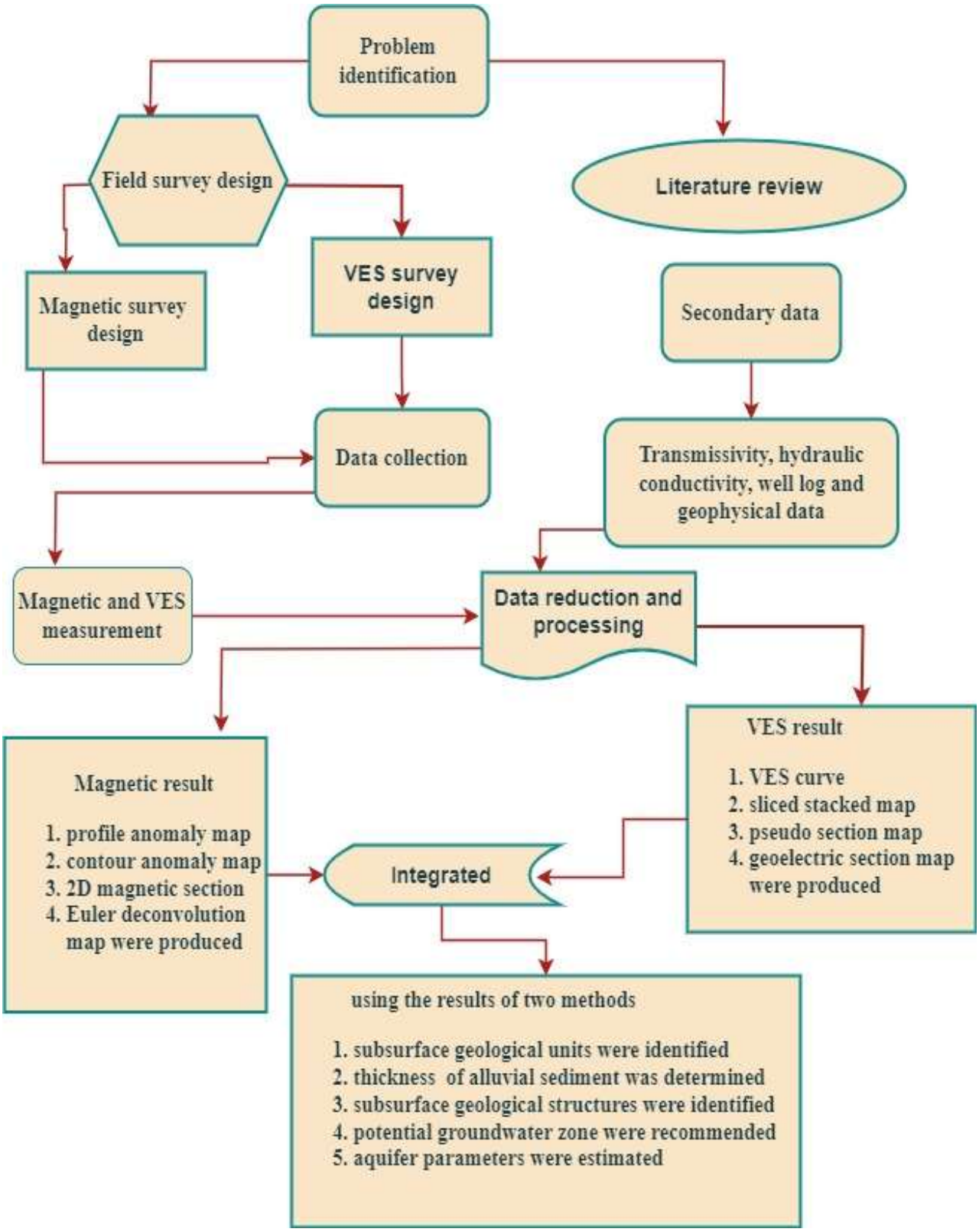

Figure 1.6: Flow chart of the methodological approach.

1.7 Basic research questions

1. How much is the depth of the potential aquifer?
2. What are the subsurface geological units in the study area?
3. What type of geological structures are present in the research area?
5. What is the spatial variability of transmissivity and hydraulic conductivity in the study area?

1.8 Significance of the study

The present study has many applications from a scientific point of view and in solving the problem as justified in the previous. In general, this study will provide vital significance, such as being used as a reference for future investigations and being used as input data for hydrogeology investigations. It will give information about the groundwater potential of the area, and a good insight for adding additional wells to satisfy the needs of society.

1.9 Research outcomes

This study has tried to determine the depth of the potential aquifer, identify the major subsurface geological units in the study area, delineate the geological structure, and estimate the aquifer parameters. After the completion of the work: groundwater potential zones were identified, aquifer parameters were estimated, the depth of aquifers in the area was recognized, and subsurface geological structures were mapped.

1.10 Limitation of the study

The study encounters limitations due to the limited VES data and its depth of investigation constraints on comprehensive aquifer characterization. In addition, the limitation of pumping test data restricts the validation of the formulated model, which integrates VES data with transmissivity value from pumping test data. Moreover, the study's area coverage is also impeding a general understanding of geological structures and aquifer geometry within the harbu–Kemise graben.

1.11 Thesis organization

The organization of the thesis comprises six chapters, each serving a distinct purpose in explaining the research study.

Chapter One: in this chapter, an overview of the research area, previous work, the statement of the problem, the general, specific objectives, and the outcomes of the investigation are included.

Chapter Two: includes both geology and hydrogeology, offering insights into the geological background of the study area. It provides description the regional geological setting and the geology of the study area. It gives the general concept of the hydrogeology of the Borkena catchment

Chapter Three: this chapter intended to establish the theoretical background of the methods employed in the study. Here, the principles and fundamental to the research methodologies are explained, providing a theoretical foundation for subsequent chapters.

Chapter Four: justifies the data acquisition, instrumentation, and processing of VES and magnetic measurement.

Chapter Five: in this chapter, the results of the VES and magnetic data are present in various formats such as profiles, VES curves, contour maps, and 2D sections and discussion is also included in this chapter.

Chapter Six: provides a general conclusion of the study from the results and discussion. Additionally, recommendations from the research findings are provided, offering insights for future research.

CHAPTER II

GEOLOGY AND HYDROGEOLOGY

2.1 Geology

2.1.1 Regional geology

The EARS stretches across Ethiopia, Kenya, and branches into the Tanzanian Craton before concluding in Mozambique. Its northern section, extending into the Afar depression, forms the prominent Rift Valley of Ethiopia (Alebachew Beyene & Abdelsalam, 2005), comprising the primary branches of the EARS are the eastern and western rift systems (Fig. 2.1). The eastern branch originates from the Afar depression in the north and spans roughly 2200 kilometers, traversing the Great Rift Valley of Ethiopia, the Kenyan rifts, and concluding in the North-Tanzanian basins. Conversely, the western branch spans about 2100 kilometers, commencing at Lake Albert in the north and terminating at Lake Malawi in the south. Additionally, a smaller southeast branch lies to the west of the Indian Ocean (Chorowicz, 2005).

The Afar depression serves as the convergence of three significant plate boundaries, where the Red Sea, Gulf of Aden, and EARS intersect (Barberi et al., 1972). Known for its low elevation, some areas within the depression descend below sea level, reaching depths of -176 meters. The underlying geology comprises thin continental and highly dense oceanic lithospheres (Alebachew Beyene & Abdelsalam, 2005).

As Hofmann et al. (1997) documented the EFB, which erupted over 30 million years ago, rapidly formed an extensive volcanic plateau within less than 1 million years. This volcanic activity occurred in conjunction with the Afar mantle plume, as noted by Richards et al. (1989), resulting in the formation of the Ethiopian trap succession near the Afar depression. Kieffer et al. (2004) identified the Simien shield volcano in the northeast of Ethiopia, which overlies a series of FB. These basalts, along with the majority of the shield volcano, exhibit tholeiitic characteristics. Additionally, the Choke and Guguftu shield volcanoes, erupting around 22 million years ago, cover a thinner succession of flood basalt. In the same region, there exists another type of lava that erupted around 30 ma, characterized by high alkalinity and rich in incompatible elements. However, this lava type is restricted to the northeastern part of the country and displays sharp inclines due to deformation. As Hofmann et al. (1997) stated, the late Eocene and Oligocene FB are overlain by Miocene shield volcanoes in the northwestern Ethiopian plateau.

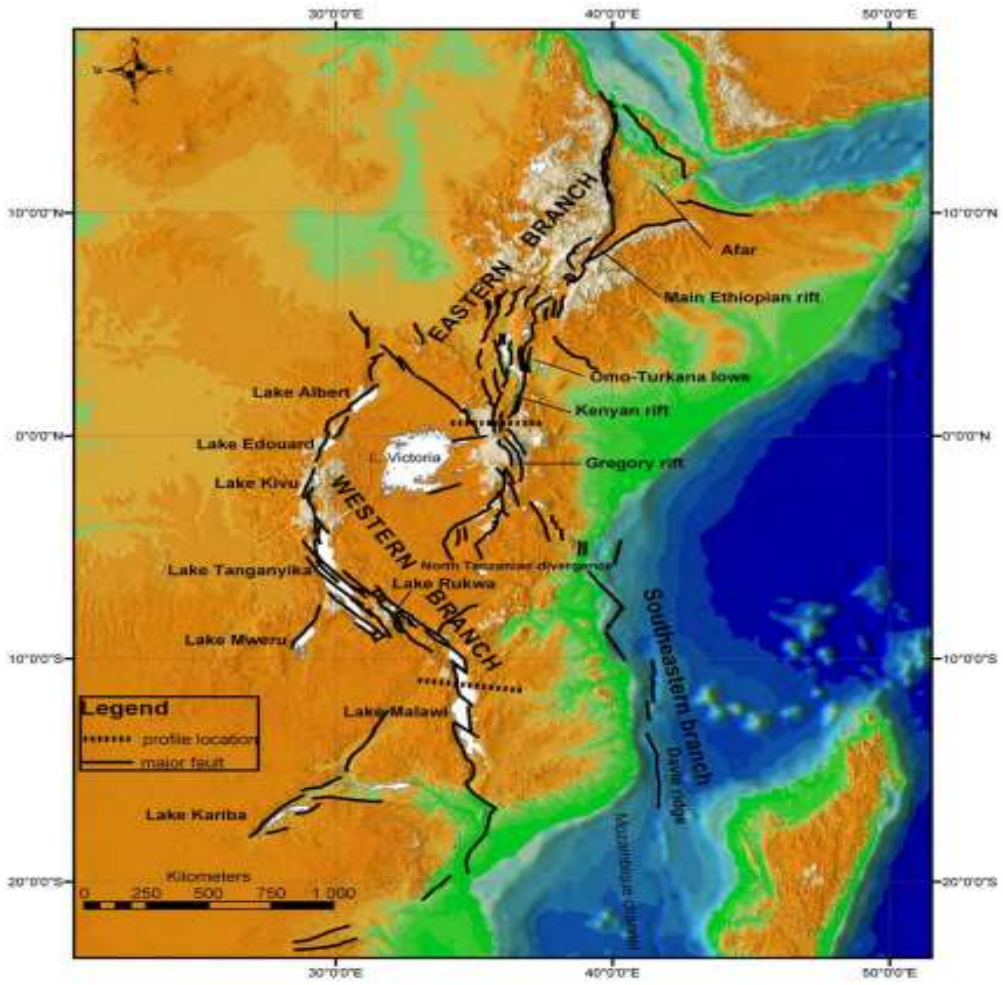

Figure 2.1: East African rift systems (Zwaan et al., 2020).

Western boundaries of afar are extending from Meghezes through Wollo; Tigrai to Eritrea where it joins with the Red Sea Rift (Mohr, 1962). The N-S striking Western Afar margin shows a change in elevation as well as thickness of continental lithosphere, the plateau has heights of up to 4 km, while Afar is located in the north close to or even below sea level (Hammond et al., 2011). Mesozoic sediments overlie the Neoproterozoic rocks in the nearby Afar depression (Abbate et al., 2015; Tadesse Alemu et al., 2018).

The Oligocene-Miocene Trap series mainly covers the Ethiopian plateau and the western Afar margin, while the rift floor and extension graben of the western Afar border are overlaid by Quaternary volcanic and lacustrine sediments, respectively (Barberi & Santacroce, 1980). According to Berhe et al. (1987) the chrono-stratigraphical subdivision of the volcanism in north-western Ethiopia traditionally comprises three formations: the Ashangi formation, the Aiba

basaltic formation, and the overlying ignimbritic Alaji formation. Furthermore, the detailed lithostratigraphy of northwestern plateau volcanic sediments subdivided into Ashangi, Aiba basalts, Alaji Rhyolites, and Termaber Basalts (Zanettin et al., 1974); also according to Dereje Ayalew et al. (2021) the Wegeltena rhyolite formation has introduced the Wegeltena rhyolite formation into this classification scheme.

A) Ashangi Formation

It represents the earliest Tertiary volcanic deposits discovered in northern Ethiopia. Situated above Mesozoic formations within the Mekele basin, this sequence is characterized by the presence of phenocrysts, which crystallized before the magma's ascent to the surface. Notably, the Ashangi formation is distinguished by its highly weathered composition, inclined stratigraphy, variable thickness, enrichment in olivine, and interbedding with pyroclastic volcanic materials. The oldest reliably dated volcanic rocks in the northern Ethiopian highlands have been estimated to be approximately 54 million years old (Kazmin, 1979).

B) Aiba basalt formation

The Aibas basalt formation is characterized by extensive basalt layers alternating with agglomeratic beds, reaching a maximum thickness of approximately 1 kilometer (Abbate et al., 2015). Its composition spans from transitional tholeiitic to alkaline. This formation is distinguished by its aphanitic texture, compacted nature, horizontal bedding, and notable columnar joint structure. The Alaji formation overlays this sequence on the northwestern plateau (Mohr & Zanettin, 1988). The eruption period of these formations occurred between 31 and 29 million years ago (Abbate et al., 2015).

C) Wegel Tena rhyolitic-ignimbrite Formation

According to Dereje Ayalew et al. (2021) in the northwestern Ethiopian plateau, a rhyolitic ignimbrite unit crowns a sequence of flood basalts (FB). This unit is distinguished by its steep slopes and thick outcrops spanning the Wegel Tana, Debre Zebit, and Jita regions. Within the ignimbrite succession, both welded and unwelded layers are prominent.

D) Alaji Formation

This formation comprises aphanitic fine-grained basalt interbedded with rhyolitic ignimbrite units and minor trachyte deposits (Abbate et al., 2015). Eruptions within the formation span from approximately 31 to 13 ma (Zanettin et al., 1978). As Dereje Ayalew (2022) stated, the composition mainly consists of alkaline to peralkaline rhyolite and transitional basalt. The

maximum thickness reaches 500 meters, decreasing to 100 meters towards the western margin of the Afar region.

E) Termaber Formation

The formation consists of zeolitized basalt and scoraceous basalt, with a notable presence of tuff. It is primarily exposed along the escarpments of the northwest Ethiopian plateau and the western edge of Afar, indicating the presence of a shield volcano the age of the Termaber formation spans from 23 to 11ma.

2.1.2 Local geology

Around the research area, there are four distinct geological units: Rhyolite, Basalt, Trachyte, and Alluvial/Colluvial sediments.

1) Rhyolite Unit: This unit dominates the southeastern portion of the Harbu‑Chefa graben, forming a rhyolitic ridge. It is obviously visible along road cuts and is characterized by extensive fracturing.

2) Basalt Unit: Found in the northeastern, northwestern, and northern regions, particularly covering the western and northeastern mountainous areas. This unit exhibits high levels of fracturing.

3) Trachyte Unit: Predominantly located on the floor of the graben, surrounded by alluvial sediments. It covers a small area as compared to other geological units.

4) Alluvial and Colluvial Sediments: These units are primarily situated on the floor of the Harbu‑Kemise graben (Fig. 2.3). They consist of various materials such as black soil, silt, sand, and gravel. Along the Borkena River, sand and gravel deposits are prominent, while black soil and silts cover extensive portions of the investigated area.

2.1.2.1 Geological structures

The Main Ethiopian Rift ranges over 1,000 kilometers in a north-northeast to south-southwest direction, with a width of approximately 80 kilometers at its widest point in the center (Baker et al., 1972); Kazmin & Garland (1973). In the western Afar margin, there exists a fault line striking in the NNE-SSW direction. This fault extends from Debrasina to Karakore, maintaining its NNE-SSW alignment. Beyond Karakore, it diverges northeastward, while a branch turns northward, delineating the eastern boundary of the Borkena Graben. Further north, past Kombolcha, the west-dipping faults continue, forming the lake basins of Ardibo and Haik (Mohr,

1962). The south of Hayk graben also transitions into the Borkena graben (Zwaan et al., 2020). In the research area, the trends of the graben faults are almost northwest to southeast direction (Fig. 2.3).

Figure 2.2: Alluvial deposit along Borkena River (a) fractured rhyolite (b) and intensely weathered basalt (c)

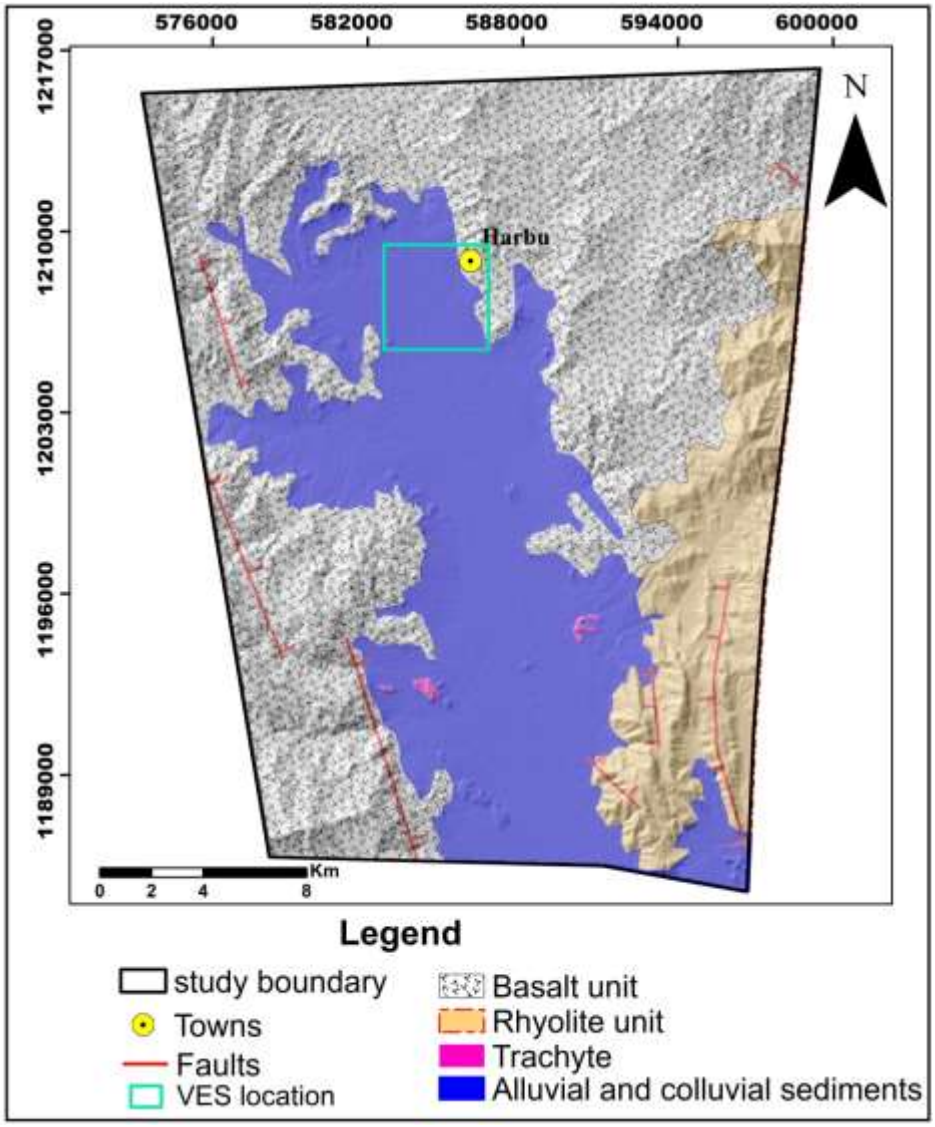

Figure 2.3: Geological map of the Harbu-Kemise graben from the Wereillu map sheet (Geological Survey of Ethiopia).

2.2 Hydrogeology of study area

The Borkena River dissects both the western and eastern escarpments that bound the alluvial sediment. As Gobezie Wallelegn et al. (2023) stated, groundwater flow within the Borkena sub-basin is significantly influenced by hydraulic gradients and elevation. Specifically, the flow direction is observed from the volcanic aquifer located at Kutaber towards the alluvial aquifers at Harbu and Kemisse, traversing through Kombolcha. In the Borkena catchment, the depth of the groundwater is highly variable. It ranges from zero (0) m in the alluvial sediments (in Kombolcha, Harbu and Kemise) to 42.6 m below ground level in the tertiary volcanic aquifers

around the Dessie area. The surface elevations are also highest in the northern part of the catchment, which is approximately 2720 m above sea level. The lowest surface elevation is located around the southern part of the Borkena catchment at 1440 above sea level.

The researchers further clarified the groundwater flow pathway originating from high mountainous areas towards Harbu and Kemisse within the Borkena Catchment due to elevation and nature of structures. In the Borkena catchment, the main recharge areas are the upper, left, and right side of the Borkena River. The lower elevation extending from Kemise to the Kombolcha area receives recharge not only from precipitation but also from groundwater flow originating upstream and from the left and right sides of the catchments, through fractures and faults (Getachew Tsigie, 2015).

Borehole data sourced from the Amhara National Regional State Water, Irrigation, and Energy Bureau reveals the presence of aquifers within the Borkena graben. These aquifers primarily consist of alluvial sediments (comprising sand and gravel), fractured basalt, trachyte, and rhyolite unit. However, the predominant water-bearing formation in the area comprises thick alluvial deposits. In Harbu – Kemise graben, the transmissivity and hydraulic conductivity values of wells in the region exhibit a range of (24.8 -1270) m^2/day and (0.258-13.3) m/day, respectively (Table.5.2). Harbu–Kemise graben is geographically divided into three distinct physiographic regions, delineated by variations in elevation (Fig.1.2).

1) Western and Eastern Mountains: These regions are characterized by high elevation compared to the floor of the Graben.

2) Graben Floor: Occupying the central expanse of the research area, the graben floor experiences by decrease in altitude. Moreover, According to the DEM of the Borkena catchment, the lowest and highest elevations are 1414 and 3419 m respectively (Fig.1.3). In the research area, the elevation ranges between 1445 and 1500 m. This indicates that the study area is a discharge area. Conversely, the northwestern and western parts of the Borkena catchment correspond to high elevation. This suggests that the recharge area is the northwestern and western part of the Borkena catchment. In the Harbu – Kemise graben, a fault line mainly strikes in the NW-SE direction. Moreover, the dipping is towards either SW or NE (Fig. 2.3). Based on surface indications, the research area demonstrates significant potential for groundwater availability.

CHAPTER III

THEORETICAL BACKGROUND OF METHODS

3. 1 Electrical and magnetic methods

3.1.1 Introduction

Applied geophysics can be applicable to investigate a specific area of the upper crust, such as for hydrocarbon exploration, studying shallow subsurface structures, searching for groundwater, minerals, and other economic resources (Parasnise, 2012).

Geophysical methods are broadly classified as either using Earth's natural fields or requiring the injection of artificial fields into the ground. The passive methods utilize the field arising from the earth itself (Kearey et al., 2002). The geophysical survey aims to find underlying geological structures or bodies and determine their dimensions and significant physical properties. Its measurement is conducted along land, sea, and air. The variation of measured electrical resistivity, potential fields, and travel time indicates the heterogeneity of the subsurface earth (Griffiths & King, 2013).

3.1.2 Electrical resistivity method

In the electrical resistivity method, the direct currents are injected into the ground and the potential differences between electrodes are measured at the surface. Variations of measured potential differences indicate the heterogeneity of subsurface earth’s materials, and they provide information on the electrical properties of the subsurface (Kearey et al., 2002; Meindinyo et al., 2017). The resistivity surveying method uses two different kinds of electrodes: current electrodes and potential electrodes. While the two potential electrodes are used to monitor the potential drop, two current electrodes is used to transfer current into the ground (Coker, 2012). The composition of the rock, temperature, porosity, saturation level, salinity of the subsurface water, degree of fracture, and degree of compaction influence the electrical resistivity of soils and rocks (Herman, 2001). A vertical electrical sounding technique is conducted to evaluate the vertical inhomogeneity of the subsurface. During a VES survey, the current electrode separation is progressively expanded around a fixed central point (Pandey, 2015).

3.1.2.1 General principle

The resistivity and conductivity vary inversely. Thus, low resistivity is found on a high-conductivity surface and vice versa. Equation (1) shows the link between resistivity (ρ) and conductivity (σ) (AL-Khafaji, 2014).

$$\rho = \frac{1}{\sigma} \tag{3.1}$$

A material's electrical resistance is typically described in terms of its resistivity. When a conductive object or body with length (L) and cross-sectional area (A) has resistance between its opposite faces of R. The resistivity (ρ) can be calculated using the formula :

$$\rho = \frac{RA}{L} \tag{3.2}$$

The study of subsurface current flow in a homogenous, isotropic earth layer using Ohm's law determines the potential difference across resistance ends, expressed as

$$\Delta V = RI \tag{3.3}$$

$$\Delta V = \frac{\rho L}{A} I \tag{3.4}$$

While J= $\frac{I}{A}$

$$\Delta V = \rho J L \tag{3.5}$$

Divide both sides by L

$$\frac{\Delta V}{L} = \rho J \tag{3.6}$$

$$\text{While, } \frac{\Delta V}{L} = -\nabla V = E \tag{3.7}$$

where I is the current in amperes, R is the resistance in ohms, ΔV is the potential difference in volts, J is current density, L is distance or length in meters, ∇V is a potential gradient in volt/meter, and E is electric filed measured in volt/meter.

Ohms' law establishes a relationship between the current density (J) and the electric field (E) as:

$$J = \sigma E \tag{3.8}$$

Where σ represents the medium's conductivity in Siemens per meter (S/m)

$$E = -\nabla V = \frac{\partial V}{\partial l} = \frac{\partial V}{\partial r} \tag{3.9}$$

This is a potential function. Thus, the equation (9) expand into

$$J = \sigma \nabla V \tag{3.10}$$

Both sides multiplied by ∇ (divergence)

$$\nabla J = \nabla * (\sigma \nabla V) \quad (3.11)$$

But $\nabla J = 0$ from the continuity equation

$$0 = \nabla * (\sigma \nabla V) \quad (3.12)$$

$$\nabla \sigma \nabla V + \nabla^2 V \sigma = 0 \quad (3.13)$$

This is the basic equation of electrical investigation or prospecting in the case of direct current.

When σ remains constant throughout, the first term disappears, resulting in Laplace's equation:

$$\nabla^2 V = 0 \quad (3.14)$$

3.1.2.2 The potential of a single electrode

Consider the current flow around an electrode in (Fig. 3.1), which injects a current I at the surface of a homogeneous half-space. The current originates at the point of contact and spreads outward from there. The equipotential surfaces are hemispherical, and the electric field lines are normal to them and parallel to the current flow (Lowrie, 2007). According to Ohm's law, the electric field E at a distance r is given as:

$$E = \rho \mathrm{J} = \frac{\rho \mathrm{I}}{2\pi r^2} \quad (3.15)$$

where $2\pi r^2$ is an area of the half sphere.

The electric potential V at distance r from the input electrode is obtained by putting this formula into Equation (3.9):

$$\frac{\partial V}{\partial r} = \frac{\rho \mathrm{I}}{2\pi r^2} \quad (3.16)$$

$$V = \frac{\rho \mathrm{I}}{2\pi \mathrm{r}} \quad (3.17)$$

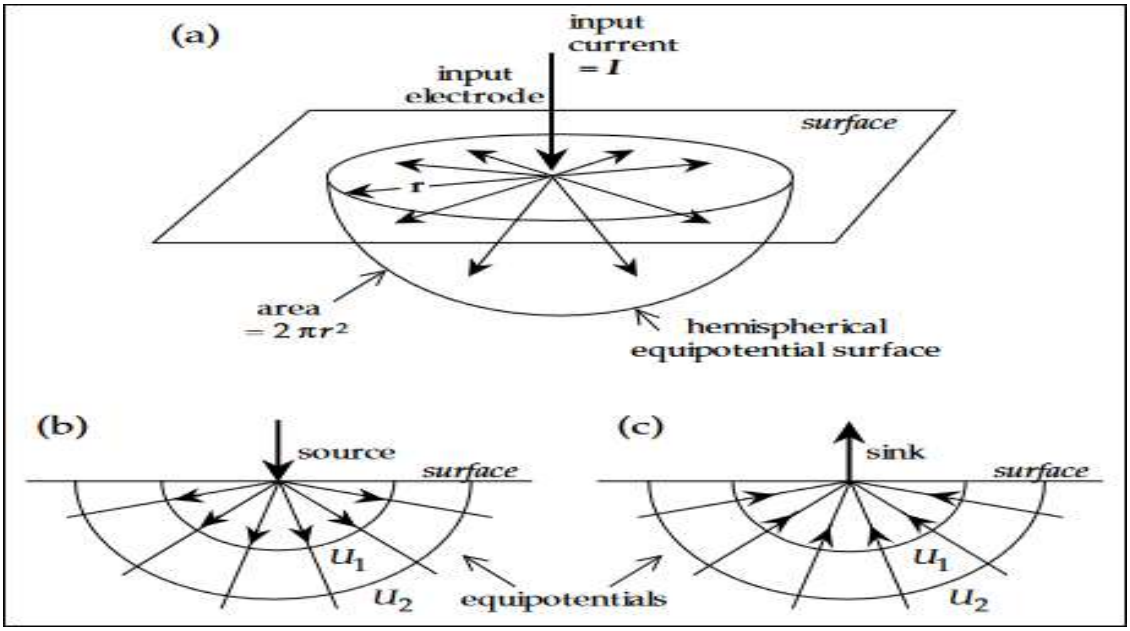

Figure 3.1: The electric field lines around a single electrode at the surface of a homogeneous half-space (Lowrie, 2007).

3.1.2.3 The general four-electrode method

Consider an arrangement with a pair of current electrodes and potential electrodes (Fig 3.2). The potential at the detection electrode C resulting from source A is$\frac{+\rho I}{2\pi r_{AC}}$, whereas the potential at B is$\frac{-\rho I}{2\pi r_{r_{BC}}}$. At C, the total potential is

$$V_C = \frac{\rho I}{2\pi r_{AC}} - \frac{\rho I}{2\pi r_{CB}} \quad (3.18)$$

$$\frac{\rho I}{2\pi}\left(\frac{1}{r_{AC}} - \frac{1}{r_{CB}}\right) = V_C \quad (3.19)$$

Likewise, the potential that results at D is

$$\frac{\rho I}{2\pi}\left(\frac{1}{r_{AD}} - \frac{1}{r_{DB}}\right) = V_D \quad (3.20)$$

The potential difference between C and D is given as :

$$\frac{\rho I}{2\pi}\left(\frac{1}{r_{AC}} - \frac{1}{r_{CB}}\right) - \left(\frac{1}{r_{AD}} - \frac{1}{r_{DB}}\right) \quad (3.21)$$

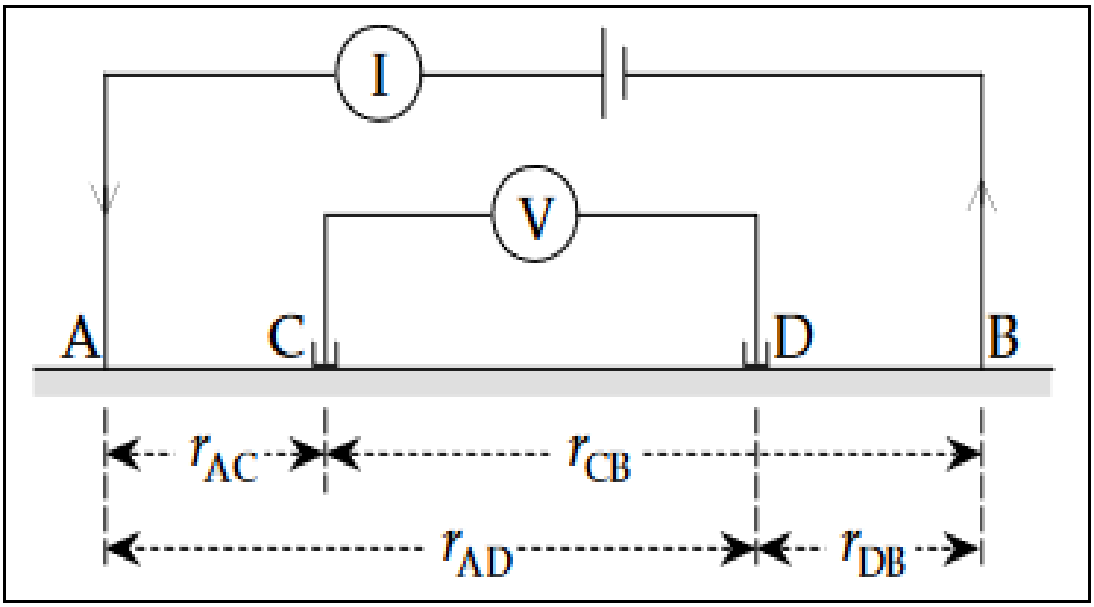

Figure 3.2: The general four electrodes set up for resistivity measurement (Lowrie, 2007).

3.1.2.4 Apparent resistivity

Distributions of subsurface resistivity can be determined by applying the electrical current to the ground and determining the potential differences using potential electrodes. Earth's subsurface is characterized by different geological units and structures. However, this heterogeneity is not considered while measuring electrical resistivity with four electrode methods, which suppose that the ground is homogeneous. The result of this measurement is the apparent resistivity (Lowrie, 2007). To investigate lateral inhomogenity in apparent resistivity that may represent lateral geologic variability, the electrode separation should be the same. To examine variations in resistivity with depth, the electrode separation should be increased progressively (Adli et al., 2010).

3.1.2.5 Schlumberger configuration

The Schlumberger array configuration is applied for VES investigation. Four collinear electrodes, such as potential electrodes and current electrodes make up this configuration. The potential electrodes are positioned between the current electrodes; the potential electrode is moved when the voltage is too low to measure, while the current electrodes' distance from one another is increased to allow current to flow far below the surface of the earth. The central point of the potential electrodes is maintained constant (AL-Khafaji, 2014).

The Schlumberger array has a smaller potential electrode distance (MN) in relation to the current electrode distance (AB), where AB ≥ 5MN (Kunetz, 1966). The apparent resistivity (ρa) given as:

$$\rho_{A=\pi*}\left\{(\frac{AB}{2})^2-(\frac{MN}{2})^2\right\}*\frac{\Delta V}{I} \quad (3.22)$$

Where the potential difference over the applied current is expressed as $\frac{\Delta V}{I}$, the half distance of potential electrodes is expressed as $\frac{MN}{2}$ and the semi distance of current electrodes is expressed as $\frac{AB}{2}$, ρ_A is the apparent resistivity is expressed as ρ_A, and the geometric factor is expressed as $\pi*\left\{(\frac{AB}{2})^2-(\frac{MN}{2})^2\right\}$

3.1.2.6 Electrical resistivity of different rocks and sediments

Except for metallic deposits and clays, as the flowing groundwater, the current flow is contained in pores and fissures, but the rock matrix affects the flow of current through pores media. The resistivity of subsurface earth's material relies on the degree of saturation, fracture density, degree of interconnection of fractures, degree of compaction, degree of weathering, and salinity of groundwater (Griffiths & King, 2013).

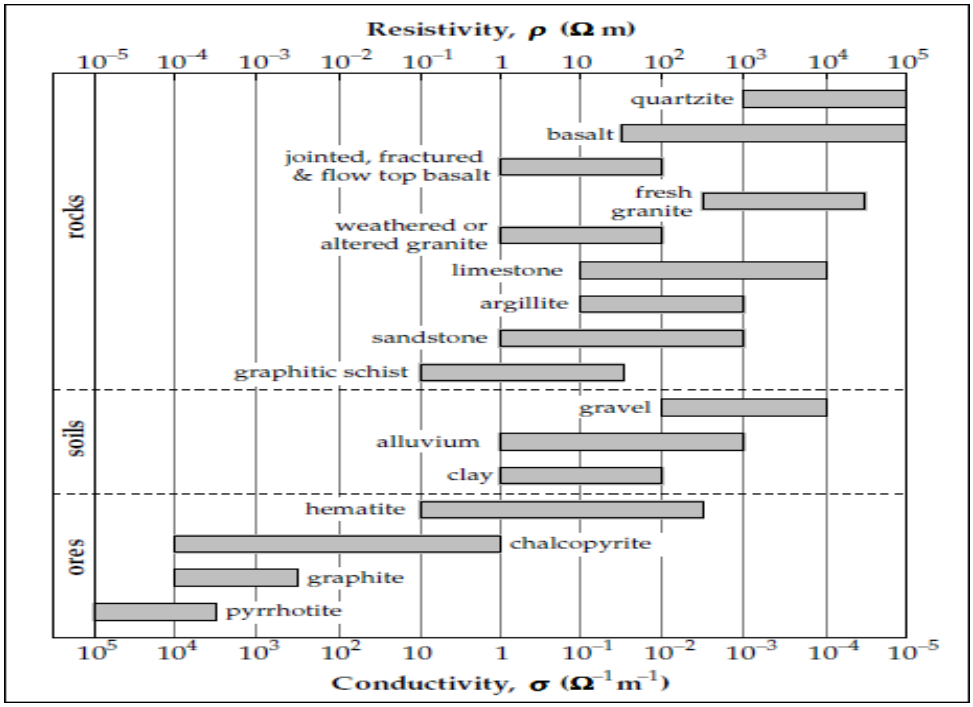

Figure 3.3: Electrical resistivity ranges of common rocks, sediments, and ores (Telford et al., 1990).

3.1.2.7 Vertical electrical sounding curves

While the current flow reaches the boundary between two different layers, the current lines change their direction depending on the nature of the geological unit (Lowrie & Fichtner, 2020). The resistivity contrast between the two layers also determines the form of the apparent resistivity versus electrode spacing curve. The apparent resistivity curve for two layers, depending on the value of ρ_1 and ρ_1, has two shapes ascending and descending. The three-layer sounding curve, depending on the value of ρ_1, ρ_2, and ρ_3, has four shapes such as minimum type or H type ($\rho_1 > \rho_2 < \rho_3$), double descending or A type ($\rho_1 > \rho_2 > \rho_3$), maximum type or K type ($\rho_1 < \rho_2 > \rho_3$), and double ascending or Q type ($\rho_1 < \rho_2 < \rho_3$).

3.1.2.8 Dar-Zrrouk parameters

Dar-Zarrouk parameters are quantified as follows:

$$L_C = \sum_1^N \frac{h}{\rho} \quad (3.23$$

$$T_R = \sum_1^N h\rho \quad (3.24)$$

where h is the thickness of the aquifer, ρ is the resistivity of the aquifer, N is the number of layers, L_C is longitudinal conductance (Ohm^{-1}), and TR is transverse resistance ($Ohm\text{-}m^2$).

The groundwater flow through an aquifer is governed by the transmissivity T, which can be given as follows:

$$T = Kh \quad (3.25)$$

Where K is the hydraulic conductivity (m/s) and T is the transmissivity (m^2/s)

As stated (Singh, 2005) the current density (J) and the Electric field (E) are related through Ohms' law and groundwater movement governed by Darcy's law.

$$J = -\sigma \frac{\partial V}{\partial r} \quad (3.26)$$

$$q = -K \frac{\partial h}{\partial r} \quad (3.27)$$

Where J is current density (ampere/area), σ is electrical conductivity (Siemens/m), V is electric potential (Volts), r is the distance (m), K is hydraulic conductivity (m/s), h is hydraulic head and q is specific discharge (m/s). in addition, the groundwater movement and electric current flow through a connected porous medium may have some similarities, so for the groundwater study, the electrical technique is powerful (Singh, 2005). The analytical connection between

transmissivity, longitudinal conductance, and transverse resistance was established by (Niwas & Singhal, 1981). The Dar-Zarrouk and aquifer parameters related as follows:

Divide equation 3.24 by equation 3.25

$$\frac{T}{T_R} = \frac{Kh}{\rho h} = \frac{k}{\rho} \quad (3.28)$$

$$T = \frac{KT_R}{\rho} = K\sigma T_R \quad (3.29)$$

where σ is the electrical conductivity of the aquifer

$$\text{If } \frac{K}{\rho} = \alpha \quad (3.30)$$

$$T = \alpha T_R \quad (3.31)$$

This is the relationship between transmissivity and transverse resistance of the aquifer. Then to determine the relationship between longitudinal conductance and transmissivity:

Divide equation 3.25 by equation 3.23

$$\frac{T}{L_C} = \frac{Kh}{\frac{h}{\rho}} = \frac{kh\rho}{h} = k\rho \quad (3.32)$$

$$T = K\rho L_C \quad (3.33)$$

$$\text{If } \; k\,\rho = \beta \quad (3.34)$$

$$T = \beta L_C \quad (3.35)$$

3.1.3 Magnetic method

The magnetic method uses a magnetometer to measure the magnetic field of Earth on the surface of the Earth. Unlike the gravity field, which has a vertical direction and temporal invariance gravity field, the magnetic field varies in time, is dipolar, and is variable in direction (Valenta & 2015). The goal of the magnetic method approach is to investigate magnetized rocks and hidden metallic deposits (Hansen et al., 2005). Furthermore, Investigation using the magnetic method approach is important to determine the depth of basement rock which is overlain by sediments, the depth of unconsolidated sediments, and subsurface geological structures like fault and shear zones (Mark, 2013).

3.1.3.1 Fundamental concepts of magnetic field

Coulomb's law determines the magnetic force F_m acting between a big magnet's two poles, which are separated by a finite distance r and have pole strengths of –p and +p (Lowrie & Fichtner, 2020).

$$F_m = -\frac{\mu_0 1 P_1 P_2}{4\pi\mu_r r^2} \quad (3.34)$$

Where p1 &p2 are pole strength in ampere meters, r is the distance between two poles in meters, μ_0 and μ_r are the Magnetic permeability in the vacuum and relative permeability in the medium respectively, and F_m is the magnetic force between the poles. The total magnetic field of the magnet at the location of the positive test pole is the sum of B_n and B_p given by:

$$B_T = -\frac{\mu_0 1p1}{4\pi\mu_r\, rn^2} + \frac{\mu_0 1p2}{4\pi\mu_r\, {r_p}^2} \quad (3.35)$$

Where rn and r_p are the distance between negative pole strength and positive pole strength respectively, B_T is the total magnetic field in gamma or Nano tesla, and μ_0 and μ_r are the Magnetic permeability of the vacuum and relative permeability of the medium respectively. The earth's magnetic field B varies with location, just as the gravity field g. As a result, the magnetic potential gradient used to calculate the B-field at any position p (r, θ, ∅) as follows:

$$B = -\nabla W \quad (3.36)$$

Where W is magnetic potential, ∅ is longitude, θ is colatitude and measured from north to the equator, r is the radius, and B is the magnetic field.

3.1.3.2 Geomagnetic field

The fluid motion, which is composed of molten iron and nickel, in the outer core produced the electric current. While the dynamic fluid moves across the field lines, the induced magnetic field is created (Lindsay, 1940; Mark, 2013). However, the magnetic field of Earth is not only a result of a dipole field but also an external field and the local anomaly or rock magnetism is a component of Earth's magnetic field. As Valenta (2015) stated, the Earth' magnetic field can be divided into three components such as the main field originating within the Earth's interior and changing relatively slowly, the external field which comes from outside the Earth and varies quite quickly. This represents one percent of the Earth's field, Local anomalies caused by spatial inhomogenity of rock magnetism in the crust.

The magnetic field of earth is a vector quantity that changes in magnitude and direction over the surface of the spherical earth. Therefore, the Cartesian component is used to describe the magnetic field elements (Fig. 3.4). The direction of a magnetic field is described by two angles: declination, the angle between the magnetic meridian and the geographic meridian, and inclination, the angle at which the magnetic vector dips below the horizontal. The Earth's magnetic field is described by north, east, and vertical components, declination angles, inclination angles, and total field intensity, with Cartesian (X Y Z) and spherical polar (F I D) (Lowrie & Fichtner, 2020). Using the trigonometric relation the geomagnetic elements are related to each other as:

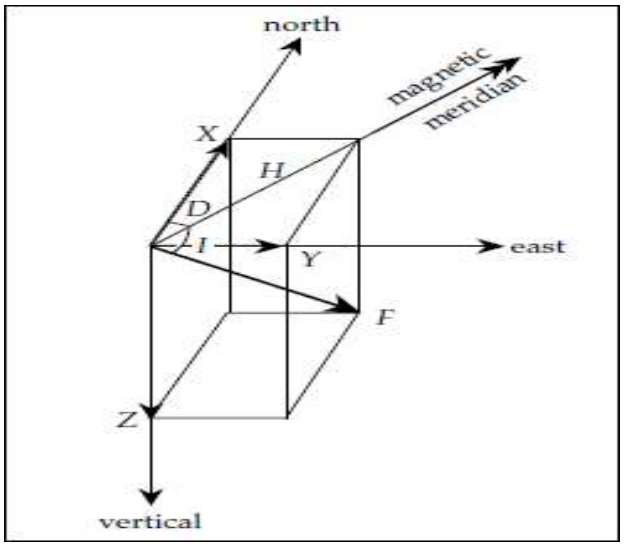

$$X = H\cos D$$

$$Y = H \sin D$$

$$Z = F \sin D$$

$$H = \sqrt{X^2 + Y^2}$$

$$F = \sqrt{X^2 + Y^2 + Z^2}$$

$$D = arc\tan\left(\frac{Y}{X}\right)$$

$$I = arc\tan(Z/\sqrt{X^2 + Y^2})$$

Figure 3.4: Geomagnetic elements from (Lowrie & Fichtner, 2020).

3.1.3.3 Magnetic field variations

The magnetic field of earth is not always constant at any given location. However, their variations are different due to variation time. The secular variation of the earth's magnetic field of earth well-known by slow changes occurred over centuries. The variation is related to the change in the direction of fluid flow in the outer core. The diurnal variation, a time-dependent change in geomagnetic field intensity, occurs as the Earth rotates beneath the ionosphere, with an amplitude of 10-30nT and a day. Magnetic storms, characterized by sudden increases in ionosphere magnetic activity, often coincide with increased sunspot activity, causing irregular and unpredictable magnetic observations; making exploration magnetic surveys unsuitable (Lowrie & Fichtner, 2020).

3.1.3.4 Permanent and induced magnetization

As Mark (2013) stated, magnetic method is sensitive to differentiate the spatial variations of rocks and soils in magnetization. Induced magnetization (MI) occurs when the magnetic material is exposed to the external field. The magnetization decays while the external field is removed. Assume that a weak magnetic field (H), like the geomagnetic field B, is applied to a magnetic substance. As a result, MI = χH. Where χ is the magnetic susceptibility of the material. The induced magnetization is proportional to the applied magnetic field. In the magnetic investigation in the continental crus the remnant magnetization is negligible.

3.1.3.5 Reduction of magnetic field measurements

Magnetic data reduction removes magnetic variation from observations, excluding subsurface magnetic effects. It avoids noises and delineates subsurface anomalies (Kearey et al., 2002). Because the Earth rotates beneath various regions of the ionosphere throughout the day, the external field changes at every location on the surface, making diurnal correction is crucial. By putting in a continuously measurement at a fixed base in the survey region, the variation can be avoided (Lowrie & Fichtner, 2020). The magnetic field variations with altitude and latitude are controlled by vertical and horizontal dipole field variations. The total intensity is calculated using the radial (Br) and tangential (B_Θ), components.

$$B_T = \sqrt{B\Theta^2 + Br^2} = \frac{\mu_0 M}{4\pi}\frac{\sqrt{1+3cos^2\theta}}{r^3} \quad (3.37)$$

The latitude adjustment is produced by differentiating the total magnetic field intensity with respect to θ,

$$\frac{\partial B_T}{\partial r} = \frac{-3\mu_o M}{4\pi}\frac{\sqrt{1+3cos^2\theta}}{r^4} = \frac{-3B_T}{r} \quad (3.38)$$

Where r is earth's radius, M is the magnetic moment of the earth, B_T is the total magnetic intensity field, θ is the colatitude measure from the poles to the equator, and μ_o is the magnetic permeability.

The altitude correction near the pole and equator is about 0.030 and 0.015 nTm^2 respectively. The total magnetic field intensity at the pole and equator is 60000 and 30000 nT respectively. While the total magnetic field intensity is differentiated with respect to θ to obtain the latitude correction, this gives

$$\frac{1}{r}\frac{-B_T}{\partial r} = \frac{\mu_0 M}{4\pi}\frac{1}{r^4}\frac{\partial}{\partial\theta}\sqrt{1+3cos^2\theta} = \frac{3B_T sin\theta cos\theta}{r(1+cos^2\theta} \quad (3.39)$$

At the magnetic equator and pole, the latitude correction is zero. At intermediate latitudes, it reaches a maximum value of 0.005 nT m^{-1}. However, in small area surveys the altitude and latitude correction is ignored. Therefore, the survey data can be corrected at any point by subtracting the diurnal correction (B_D) and the theoretical field value (B_T), which can be found from the IGRF from the measured value (B_{ob}) (Lowrie & Fichtner, 2020).

$$\Delta B = B_O - B_{T-B_D} \quad (3.40)$$

where ΔB is the magnetic anomaly of the earth.

3.1.3.6 The magnetic susceptibility of rocks and sediments

According to Parasnis (2012), the presence of magnetic minerals determines the susceptibility of rocks and sediments. Mafic and ultramafic igneous rocks have higher magnetic susceptibility when compared to acidic igneous rocks as well as sedimentary rocks. The porosity like faults and joints, intergranular, intragranular void, magmatic intrusion, weathering, and hydrothermal alteration also affect the magnetic susceptibility of rocks and sediments and lead to the low magnetic anomaly (Kearey et al., 2002). According to Layade et al. (2023), the magnetic survey is important to determine the depth of alluvial sediment, the depth of firm rock, the shear zone, and geological features like faults, joints, and contact between two layers.

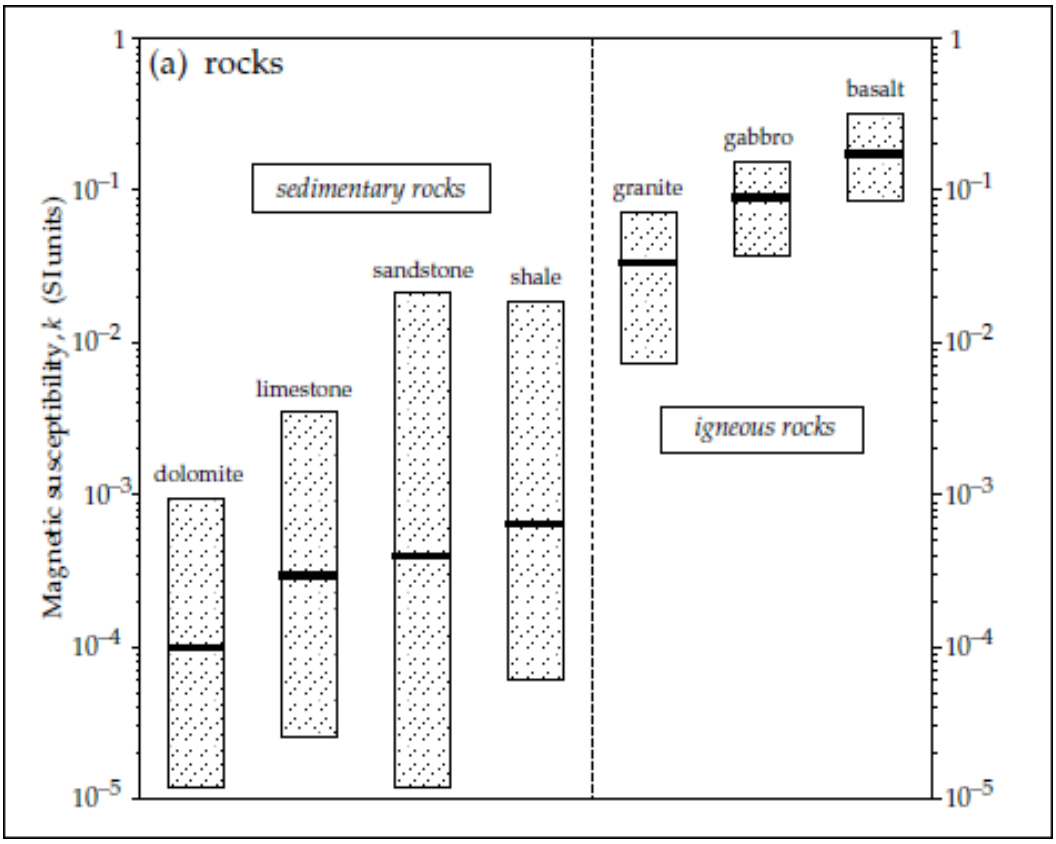

Figure 3.5: The magnetic susceptibility of some common rock types (Lowrie, 2007).

CHAPTER IV

DATA ACQUISITION AND PROCESSING

4.1. Survey traverse selection

The study area is situated within a marginal graben that is bounded by escarpments that extend from south to north and are characterized by quaternary sediments. Both the escarpment and sediment trend in a northeast to southwest direction. The primary aims of this investigation are to delineate the subsurface geological structure and determine the thickness of alluvial sediment in the graben to examine the groundwater potential of the region. Therefore, the traverse for this study has been chosen along an east-west orientation.

4.2. Data acquisition and instrumentation

4.2.1. Vertical electrical sounding

The traverse line was set up in an east-west direction (Fig. 4.1). The Schlumberger arrangement, with the maximum electrode separation (AB/2) set to 500 m, was applied. Along the traverse line, 13 VES points were selected. These points are spaced at intervals of 690 m on average along four profiles. The VES surveys utilized a PASI resistivity meter, powered by a 12V DC external battery. And observation stations were located using GPS. The process of utilizing the PASI resistivity meter to assess inhomogenity in the electrical resistivity of subsurface earth materials involved several sequential steps:

Site Selection: Initially, the most suitable location along a chosen traverse was selected, optimizing the VES site placement.

Electrode Placement: In the second step, electrode placement was undertaken. Two electrodes serve the purpose of injecting current into the ground (current electrode), while the other electrode was employed for measuring potential differences.

Current Injection into the Ground: Subsequently, current injection into the ground was conducted by connecting the current electrode to a power source.

Measurement of Potential Difference: Lastly, the potential difference was measured at the midpoint between the electrodes.

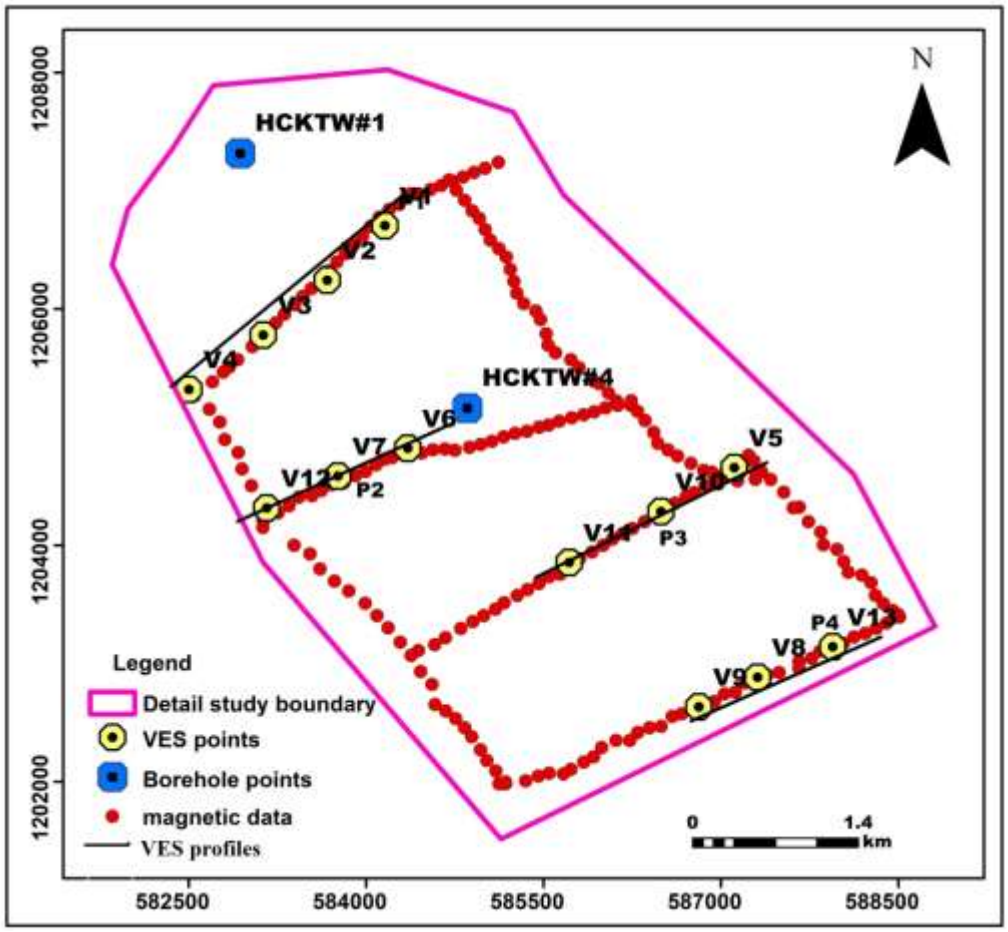

Figure 4.1: Data distribution in study area.

4.2.2 Magnetic survey

As stated by Esubalew Yehualaw et al. (2023), a magnetic survey was conducted to delineate faults that governed the availability and flow of groundwater.

In this study, a magnetic survey was conducted along an east-west orientation at regular intervals of 100 meters along each traverse to locate the possible structures and the variation in sediment thickness within the Harbu-Kemise graben. A total of 230 measurements were collected across six (6) profiles, ensuring comprehensive coverage of the area under study.

To carry out the survey, G 600 Proton Precession magnetometer was employed. This instrument provided the total magnetic field at each point along the traverse. Simultaneously, additional data such as time and GPS locations were also recorded.

4.3 Data reduction and Processing

4.3.1 VES data processing

During field measurements, the initial curve (apparent resistivity versus AB/2 distance) was produced to assure the accuracy and reliability of the data. The measured apparent electrical resistivity was processed using Win Resist software. The existing borehole was used as a constraint. The software has provided crucial information, including the thickness and resistivity of each layer, with an acceptable RMS error range of 2.5 to 4.8. This stage provided a strong foundation for further analysis and interpretation. The thickness and resistivity of each layer generated from Win Resist software were used to construct the geoelectric section (Fig.5.6 &5.8). To determine the horizontal variation of the apparent resistivity within the subsurface earth's material the pseudo depth section was constructed (Fig. 5.5), while to observe the horizontal and vertical variation of apparent resistivity at a certain depth over a plane surface sliced stacked map were prepared (Fig.5.3). The VES curve provides information on the number of subsurface layers, their resistivity values, thickness, and depth from the surface (Fig.5.1&5.2). Using this VES curve information the Dar Zarrouk parameter was calculated. Furthermore, the relationship between transmissivity and transverse unit resistance derived from the resistivity and thickness of each layer is established using a regression technique. By utilizing this regression equation, the transmissivity and hydraulic conductivity of the study area were estimated.

4.3.2. Magnetic data reduction and processing

4.3.2.1. Magnetic data reduction

One effective approach involved measuring the total magnetic field at a designated base station situated within the survey region. This served to calculate the diurnal variation. Moreover, to reduce the influence of vertical and horizontal dipole field variations, the IGRF was subtracted from the total magnetic field readings. During the magnetic data reduction process, particular attention was paid to smoothing out noisy data inherent in the total magnetic field measurements. This smoothing operation enhances the clarity and reliability of the magnetic anomaly signatures, facilitating more accurate interpretations of subsurface geological structures. By employing these techniques, the magnetic anomalies that arise from subsurface geological features are extracted.

4.3.2.2. Magnetic data processing

After magnetic data reduction, the total magnetic field that only comes from subsurface geological units remains. However, it's crucial to separate the magnetic signals originating from shallow features and those from deeper-seated geological formations. To isolate the magnetic field that comes from shallow features, an upward continuation technique was employed. Subsequently, to avoid the dipole nature inherent in the magnetic field of Earth, the residual anomaly is subjected to reduce to magnetic equator filtering. For the interpretation of shallow features, various maps were generated utilizing Oasis Montaj software. These included total magnetic anomaly map, residual anomaly map, analytic signal map, and tilt derivative map. These outputs facilitate a broad understanding of the magnetic signatures associated with shallow geological structures, helping in geological interpretation efforts. Moreover, the 2D section and Euler deconvolution map for quantitative interpretation and profile anomaly map for qualitative interpretation were prepared.

CHAPTER V

RESULTS AND DISCUSSION

5.1 General

In this chapter, survey results for the study area are presented and discussed qualitatively and quantitatively. The VES data analyses are presented as sliced stacked maps, pseudo-section maps, one dimensional inverse models and geoelectric sections. The magnetic survey analyses are presented as profile and gridded maps. In addition, a two- dimensional magnetic susceptibility inverse model is used to show variations in magnetic properties along selected profile lines. These sections were modeled to show subsurface geology and structures with implications for groundwater potential of the study area. In addition to the VES data, the Euler deconvolution has been used to constrain the 2D modeling results.

5.2 Results and discussions of vertical electrical sounding

5.2.1 Vertical electrical sounding curves

The VES curves are constructed using Win Resist software with log-log plot of apparent resistivity as the vertical axis and AB/2, representing half current electrode separation, as the horizontal axis (Fig.5.1 and 5.2). The shape of VES curves is determined by the number of resistivity layers found in the shallow subsurface and the sequence of the resistivity layers. For the study area, the shapes of the apparent resistivity versus electrode spacing curve all exhibit four-layer curves as shown in (Table 5.1), with the majority HK type.

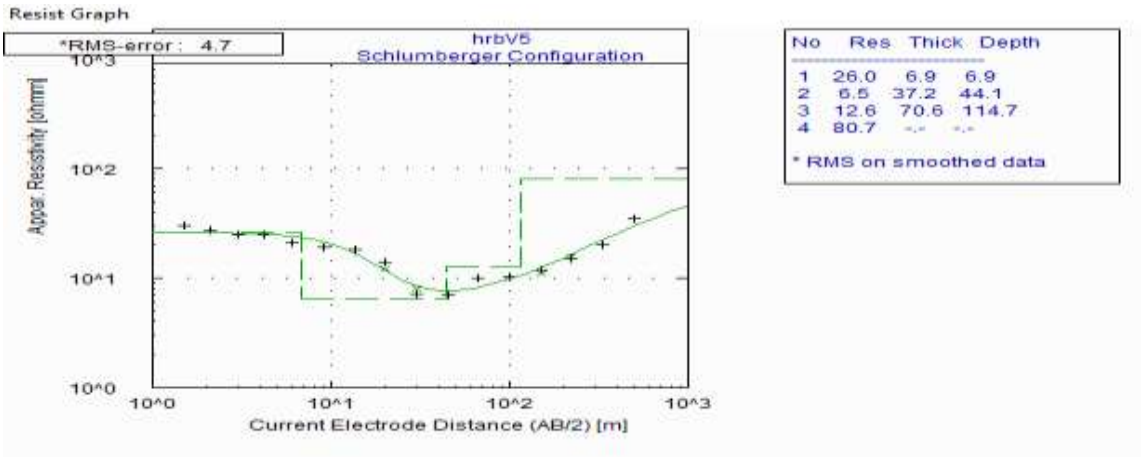

Figure 5.1: The interpreted curve model of VES 5.

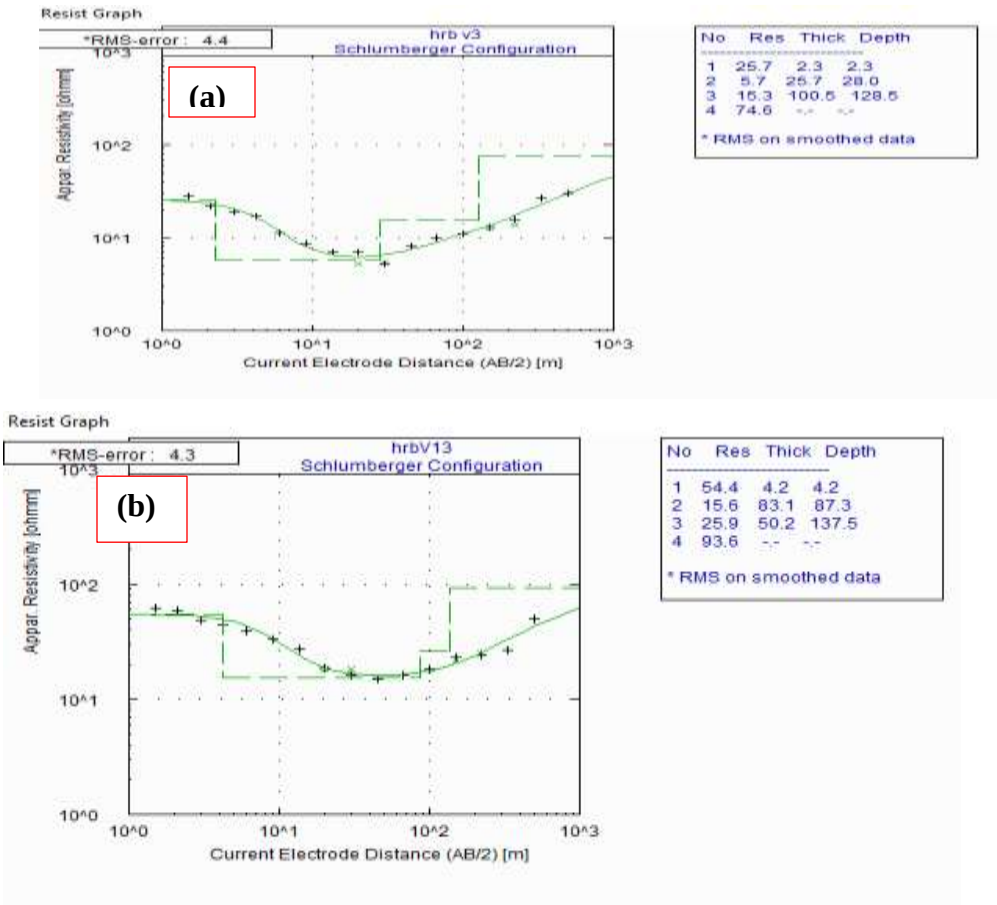

Figure 5.2: Curve model of VES 3 (a) and VES 13 (b).

Table 5.1: VES Curve type based on the resistivity value of each layer in the study area.

	Resistivity for each layer					
VES ID	ρ1	ρ2	ρ3	ρ4	Comparison	Curve type
1	7.9	24.4	9.4	6.2	ρ1< ρ2 > ρ3 > ρ4	KQ
2	20.9	7.8	15.4	3.9	ρ1 > ρ2 < ρ3 > ρ4	HK
3	25.6	5.7	15.3	74.6	ρ1> ρ2 < ρ3 < ρ4	HA
4	20.7	9	19.7	137.4	ρ1> ρ2 < ρ3 < ρ4	HA
5	26	6.5	12.6	80.7	ρ1 > ρ2 < ρ3 < ρ4	HQ
6	21	6.8	16.7	4.1	ρ1 > ρ2 < ρ3 > ρ4	HK
7	18.5	7.6	20.3	4.3	ρ1 > ρ2 <ρ3 > ρ4	HK
8	24	5.8	19	3.9	ρ1 >ρ2 < ρ3 > ρ4	HK
9	38	8.6	24.8	5.9	ρ1> ρ2 < ρ3 > ρ4	HK
10	41.3	16.4	11.5	6	ρ1 > ρ2 > ρ3 > ρ4	QQ
11	8.4	16.6	20.8	5.7	ρ1 < ρ2 < ρ3 > ρ4	KK
12	51.1	15.5	6.2	162.7	ρ1 > ρ2 > ρ3 < ρ4	HH
13	54.4	15.6	25.9	93.6	ρ1 > ρ2 < ρ3 < ρ4	HQ

5.2.2. Sliced–stacked section

As stated by (Esubalew Yehualaw et al. (2023), the stacked map constructed using the apparent resistivity values of the area. it is important to show the apparent resistivity variation in the depth as well as in the xy plane.

In this study, to illustrate the vertical and horizontal variations in apparent resistivity across the study area, a sliced stacked map was created. This map was generated by gridding selective apparent resistivity values based on AB/2 distance and GPS coordinates. The apparent resistivity values are stacked over one another according to sequential AB/2 distances (Fig.5.3). This visualization provides valuable insights into the subsurface resistivity distribution across different depths and lateral extents within the study area.

As shown in the figure below, specific AB/2 distances of 1.5, 45, 100, and 500 meters were chosen to represent apparent resistivity variations at the surface, middle, and base of the investigation. Notably, AB/2 distances of 1.5 and 500 meters are crucial for delineating the study area into eastern, western, and central zones. At an AB/2 distance of 45 meters, the apparent resistivity demonstrates a consistent trend across most sections, with VES 11 and 10 exhibiting relatively high resistivity values that may correspond to coarse grain alluvial sediments. Conversely, at the depth of 500 m the apparent resistivity value becomes very low value at VES 10 and 11, this may correspond with high clay content. At the top part of the section, the apparent resistivity varies from the central to eastern and western parts of the research area. This suggests that the variation in moisture and the availability of surface water.

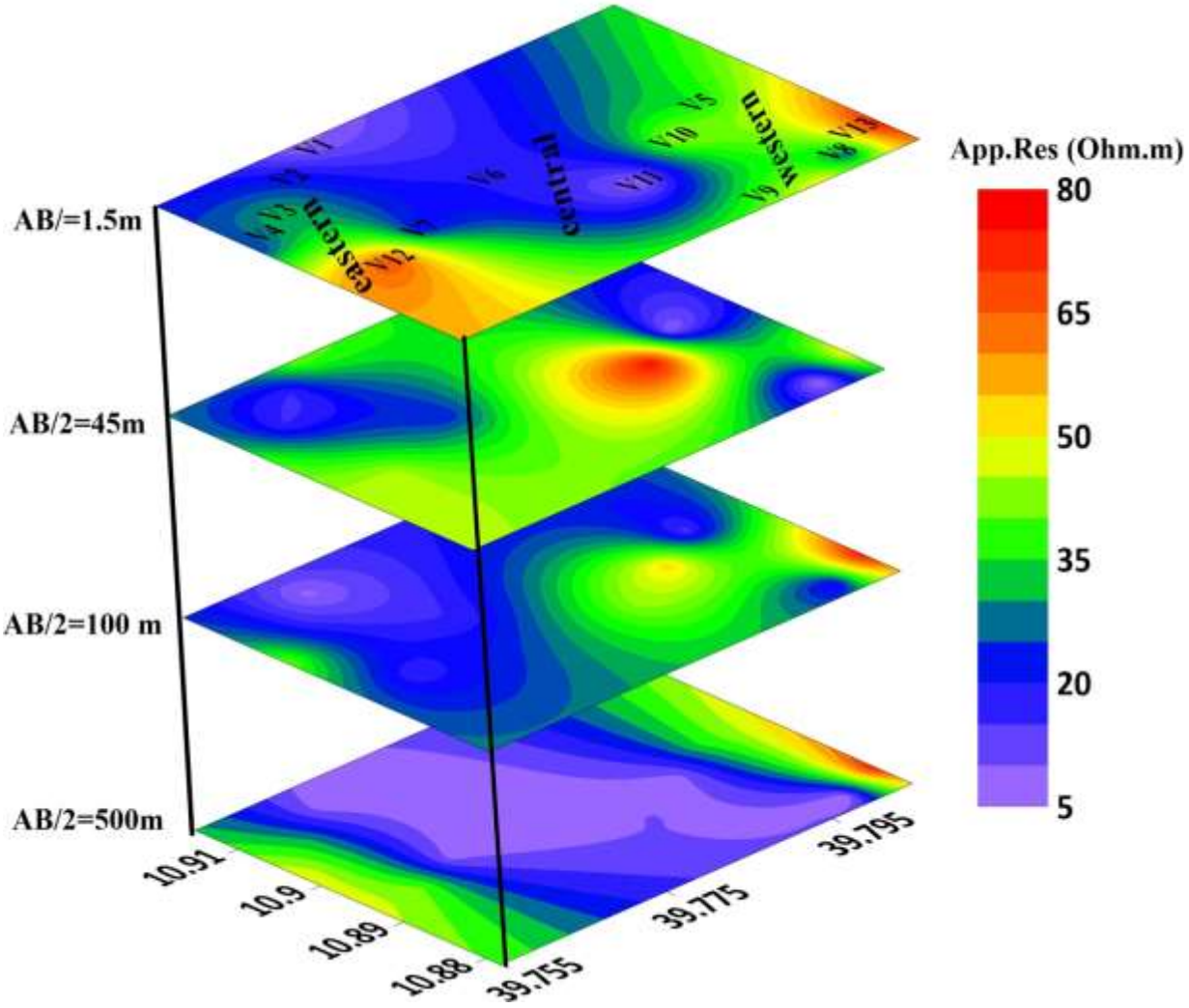

Figure 5.3: Sliced stacked map with selective AB/2 distance.

5.2.3 1D Inverse model and correlation with lithology

The 1D inverse model is constructed by an inversion process where a misfit between field curves and model curves is iteratively minimized to obtain a representative resistivity versus depth model. An initial model is specified based on the number of curvatures representing number of layers and resistivity values estimated for each layer using IPWIN software. The final model is inverted using WinResist. And the misfit measured using RMS error is between 2.5 to 4.8.

The results of the VES 1D inverse modeling were correlated with VES points where nearby boreholes were available. The maximum depth of the VES6 1D inversion is 120 m, while the total depth of the borehole (HCKTW#4) is about 324 meters. The correlation between the

borehole (HCKTW#4) and VES6 is between the surface and a depth of 120 m (Fig. 5.4). The topsoil (21) Ohm.m, gravel with clay and sand (6.8) Ohm.m, and coarse gravel (16.7) Ohm.m are well correlated between VES6 and the borehole (HCKTW#4).

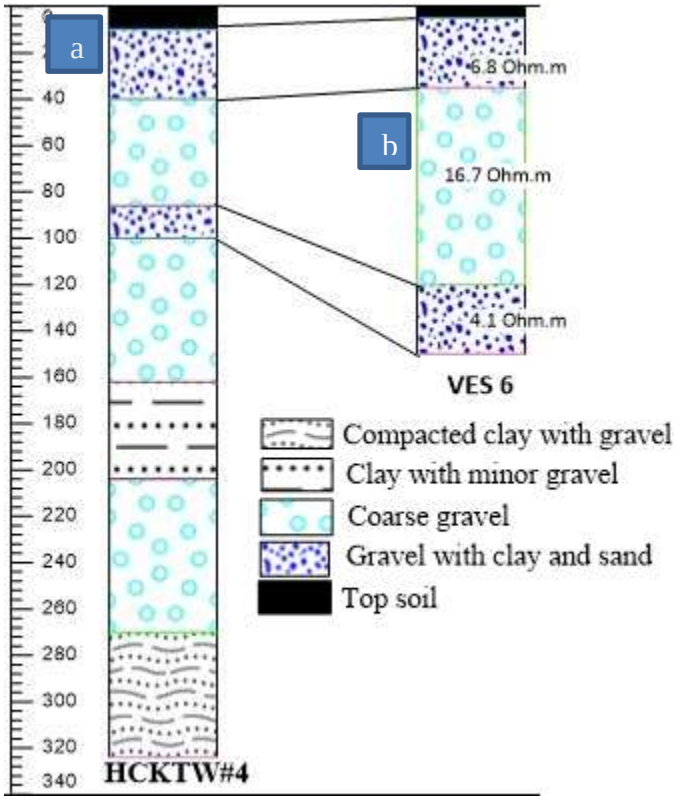

Figure 5.4: Stratigraphic log of HCKTW#4 (Amhara Water, Irrigation, and Energy Bureau) (a) and VES 6 measurement in this study (b).

5.2.4 Pseudo depth section and geoelectric section of the profiles

The pseudo-depth sections were created to illustrate the apparent resistivity variations in the 2 dimension direction. To provide a quantitative interpretation of the apparent resistivity, geoelectric sections were prepared. These sections were constructed by integrating borehole data and VES curve models.

5.2.4.1 Profile one

A) Pseudo depth section

The section of profile one was constructed using VES 1, 2, 3, and 4, providing a comprehensive understanding of the subsurface apparent resistivity variation. As shown in Fig. 5.5, the eastern

segment of the profile is notably distinguished by its lower resistivity values, suggesting potential geological variance in that region. The bottom part of VES 4 is characterized by a high apparent resistivity value. At a depth of 1.5 AB/2, VES 4 displays an intermediate apparent resistivity value compared to the others. This value could be due to the presence of dry soil at its top layer.

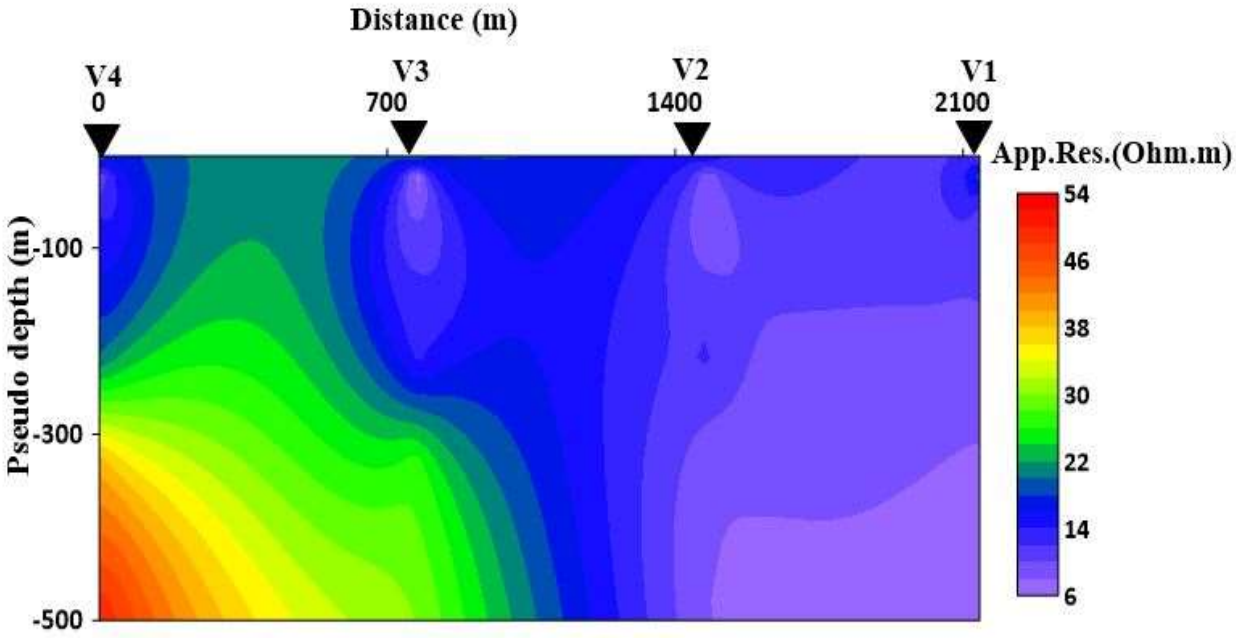

Figure 5.5: Pseudo-depth section of profile one.

B) Geoelectric section along profile one

The geoelectric section of profile one is derived from interpreted (VES) curve parameters of VES 1, VES 2, VES 3, and VES 4 (Fig. 5.6). The vertical axis of the section represents elevation from the surface to the final depth, while the horizontal axis indicates the offset. The geoelectric section delineates four (4) distinct lithological units. The uppermost layer corresponds to the topsoil. Along the western margin, particularly associated with VES3 and VES4, the apparent resistivity values are high. Conversely, the central portion of the profile exhibits lower resistivity values. The top soil exhibits a resistivity range of (7 – 20) Ohm.m. The gravel with clay and sand has the resistivity values ranging from (5.7 – 9) and (4 – 9) Ohm.m. The coarse gravel has a resistivity range of (15.4 – 24) Ohm.m. In contrast, fractured basalt shows a higher resistivity, ranging from 74 to 134 Ohm.m. The average thickness of the topsoil layer is approximately 2.1 m. The gravel with clay and sand, which is covered by topsoil, has a thickness of approximately

33 m. below this; there is coarse gravel, with an average thickness of 92.3 m. The potential aquifer in this section is coarse gravel and fractured basalt. The average depth of coarse gravel from surface is about 36 m. However, along theVES1, the depth is near surface. The depth of fractured aquifer from surface is about 128.3m.

The lower section of the eastern part of the profile is distinguished by notably low resistivity. This could be due to the presence of clay and saline groundwater.

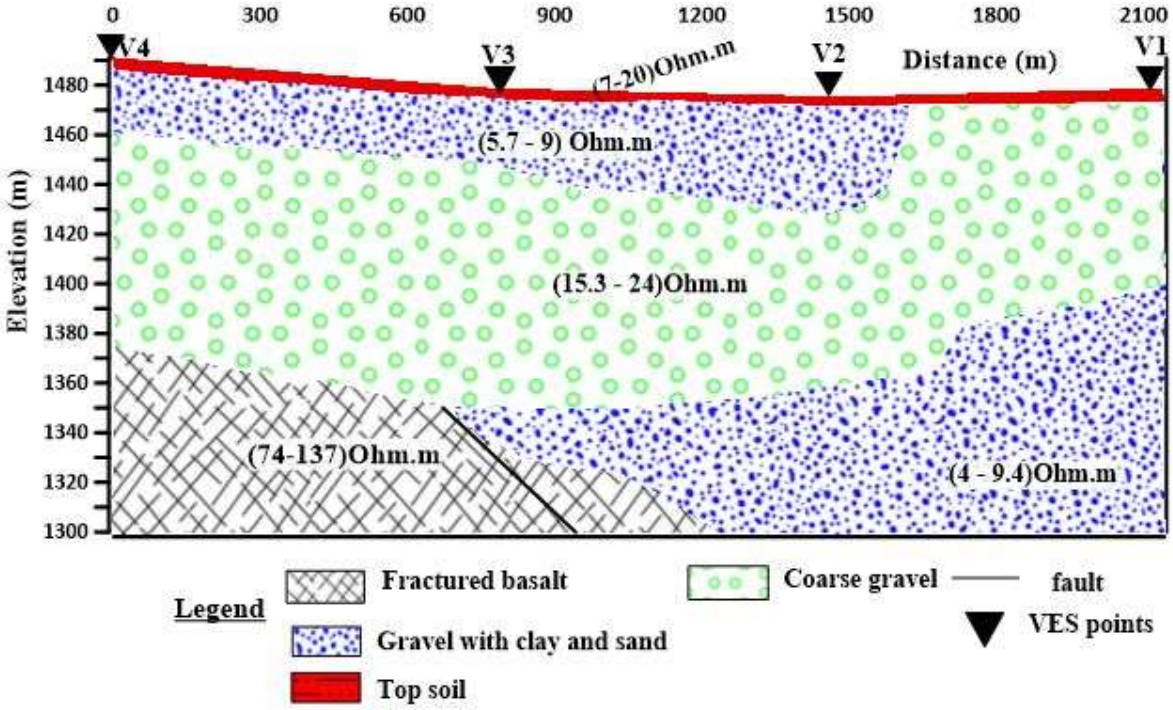

Figure 5.6: Geoelectric section of profile one

5.2.4.2 Profile two

A) Pseudo depth section

The section of Profile two was prepared using VES data from stations 12, 7, and 6 (Fig 5.7). As shown in the figure, the eastern section corresponds to low apparent resistivity as compared to the western part of the section. At 1.5 m AB/2 distance, VES 12 exhibits an intermediate apparent resistivity value compared to the adjacent stations. The lower section of the western part of the profile corresponds to high resistivity. This could be due to the presence of fractured to slightly fractured basalt.

B) Geoelectric section

The geoelectric section of profile two was generated using interpreted VES curve parameters obtained from VES12, 7, and 6 (Fig.5.8). While preparing this geoelectric section, the HCKTW#4 was used as constraint. The geoelectric section reveals approximately four (4) distinct lithological units. The uppermost layer corresponds to the topsoil, while the lower part of VES12 indicates slightly fractured basalt. In contrast, the other VES points terminate in alluvial sediments gravel with sand and clay. The top soil shows a resistivity range of (18 – 51) Ohm.m. The gravel with clay and sand has the resistivity values ranging from (6.8 – 7.6) and (4.1 – 6.2) Ohm.m. The coarse gravel has a resistivity range of (15– 20.3) Ohm.m. In contrast, slightly fractured basalt shows a higher resistivity about 162 Ohm.m. The average thicknesses of the topsoil and gravel with clay sand are approximately 4 and 29.8 m, respectively. The average thickness of coarse gravel measures about 101 m. Additionally, there is a layer of thick gravel with clay and sand, measuring about 70 m, located between slightly fractured basalt and the coarse gravel. The potential aquifer in this section is coarse gravel. Its average depth from surface is about 33.6 m. However, along the VES12, the depth is near surface.

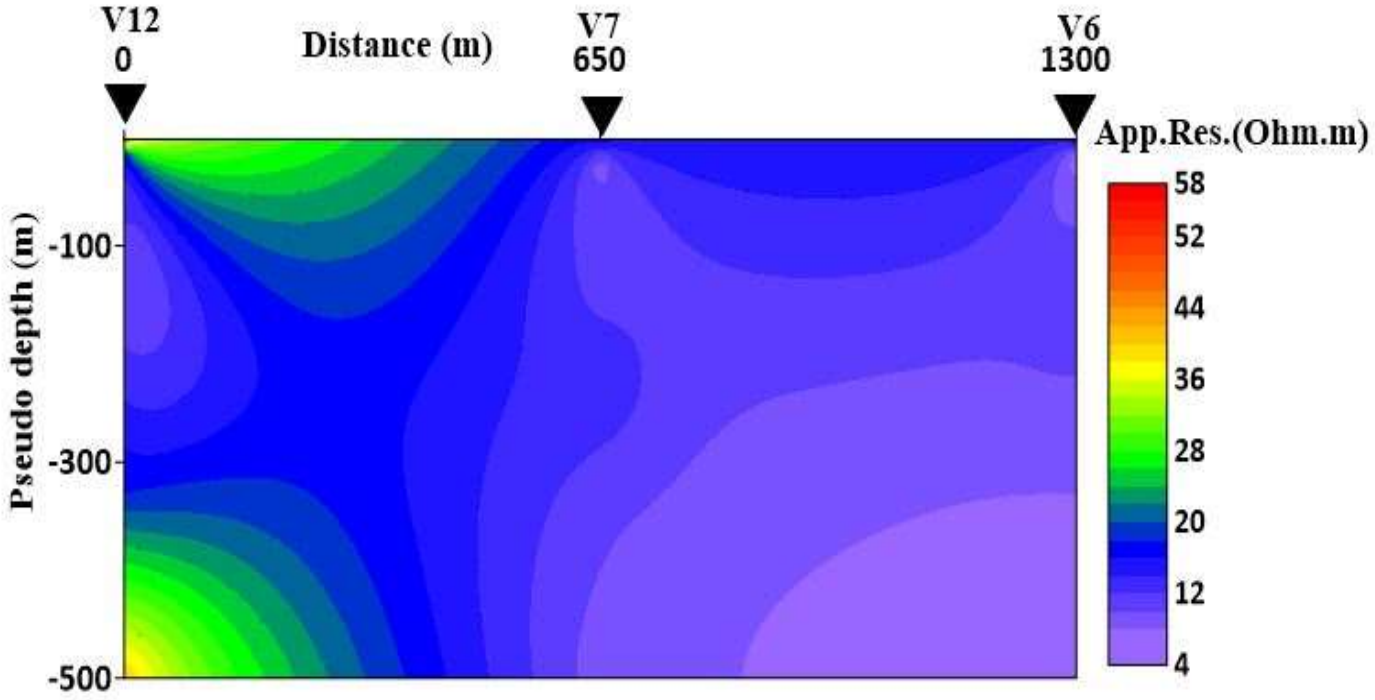

Figure 5.7: Pseudo-depth section of profile two.

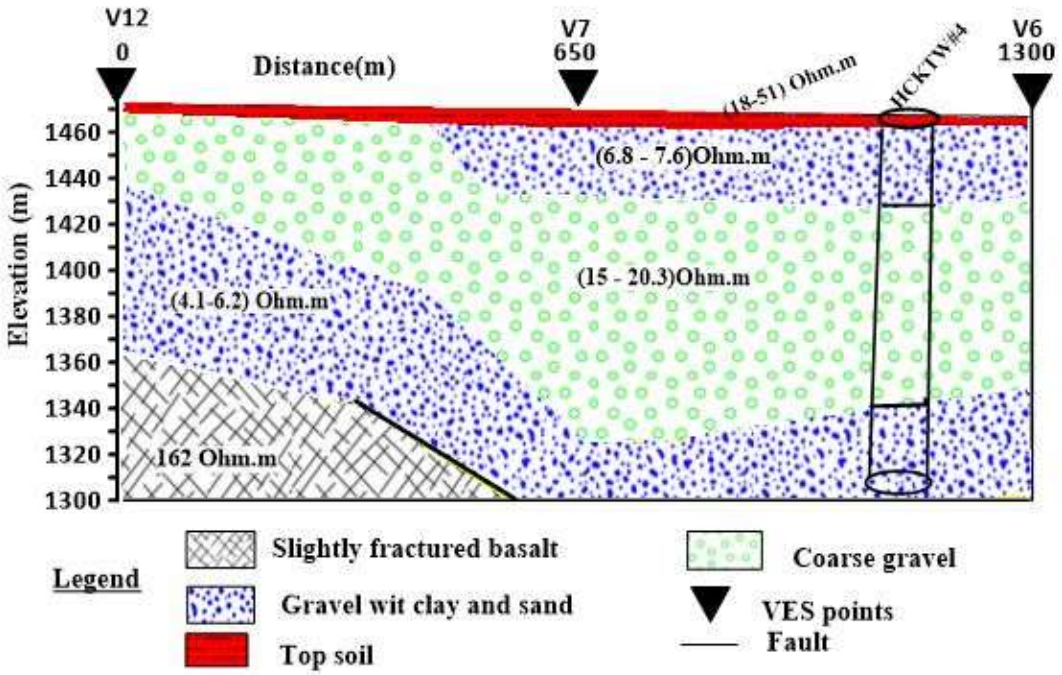

Figure 5.8: Geoelectric section of profile two

5.2.4.3. Profile three

A) Pseudo depth section

The section of Profile 3 was created using VES data from stations 5, 10, and 11. As shown in Fig. 5.9, VES 5 and 10 exhibit intermediate resistivity values in their upper portions. However, at the lower segment of VES 12, a high apparent resistivity value is observed. Conversely, in VES 11, both the upper and lower segments are characterized by low apparent resistivity values.

B) Geoelectric section

The geoelectric section was prepared based on interpreted parameters extracted from VES curves, specifically from VES 5, 10, and 11 (Fig.5.10). As presented in the figure, the geoelectric section delineates approximately four (4) distinct lithological units. The uppermost layer corresponds to the topsoil. Beneath VES 5 lies fractured basalt, while the other VES is bottomed by alluvial sediments. The top soil shows a resistivity range of (8 – 41) Ohm.m. The gravel with clay and sand has the resistivity value ranging from (4.1 – 6.5) Ohm.m. The coarse gravel has a resistivity range of (11.5– 18) Ohm.m. On the other hand, fractured basalt shows a higher resistivity about 79 Ohm.m. The average thicknesses of the topsoil and gravel with clay sand are approximately 5.2 and 37 m, respectively. The average thickness of coarse gravel is about 143 m. However, the thickness of the coarse gravel decreases significantly towards VES 5. The

potential aquifer in this section is coarse gravel and fractured basalt. The average depth of coarse gravel from surface along VES5 is about 43 m. However, along the VES11 and 10, the depth is near surface. The depth of fractured basalt is about113.6 m.

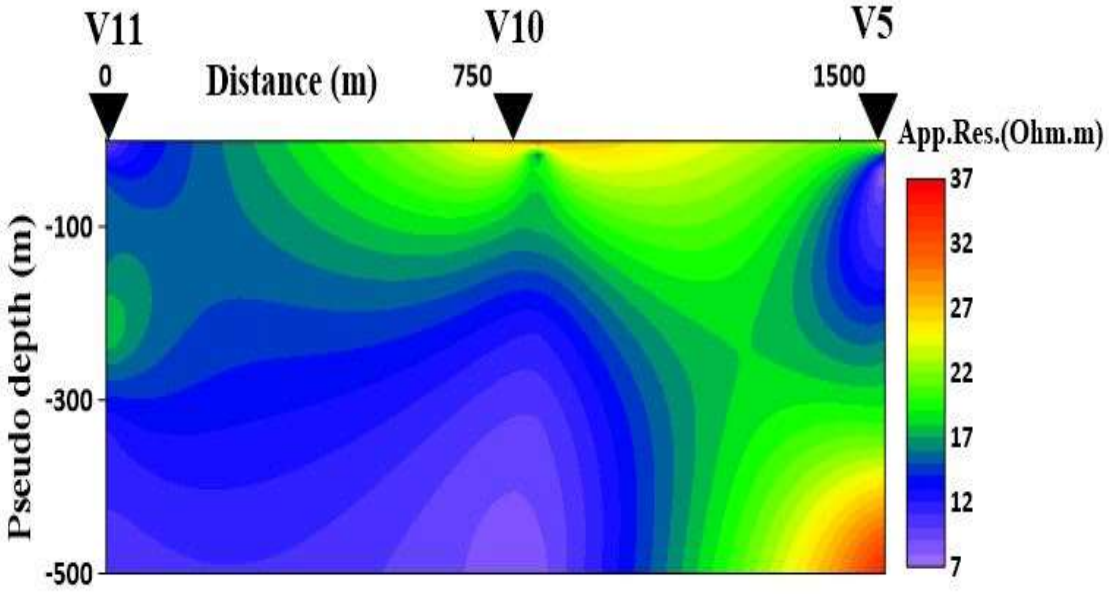

Figure 5.9: Pseudo-depth section of profile three.

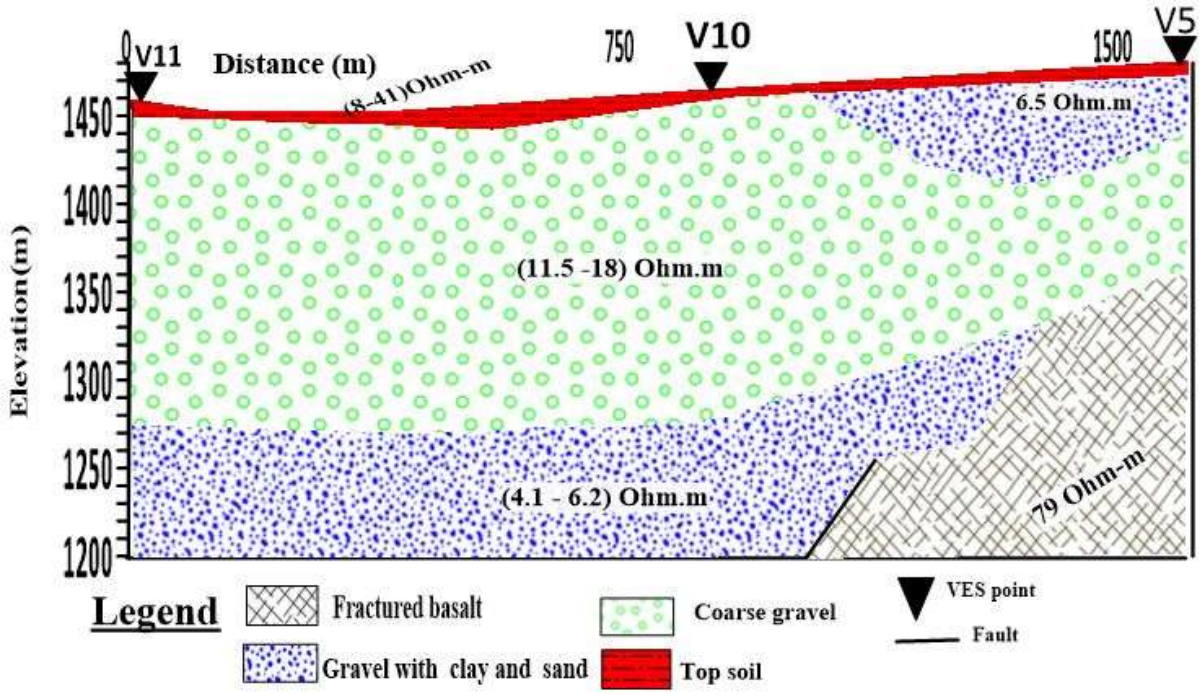

Figure 5.10: geoelectric section of profile three.

5.2.4.4. Profile four

A) Pseudo depth section

The section of profile 4 was produced using VES data from points 13, 8, and 9 (Fig. 5.11). As shown in the figure, section VES13 exhibits intermediate resistivity values at its upper portion, while the lower part shows high apparent resistivity values. However, VES points 8 and 9 demonstrate consistently low apparent resistivity values throughout both the upper and lower sections.

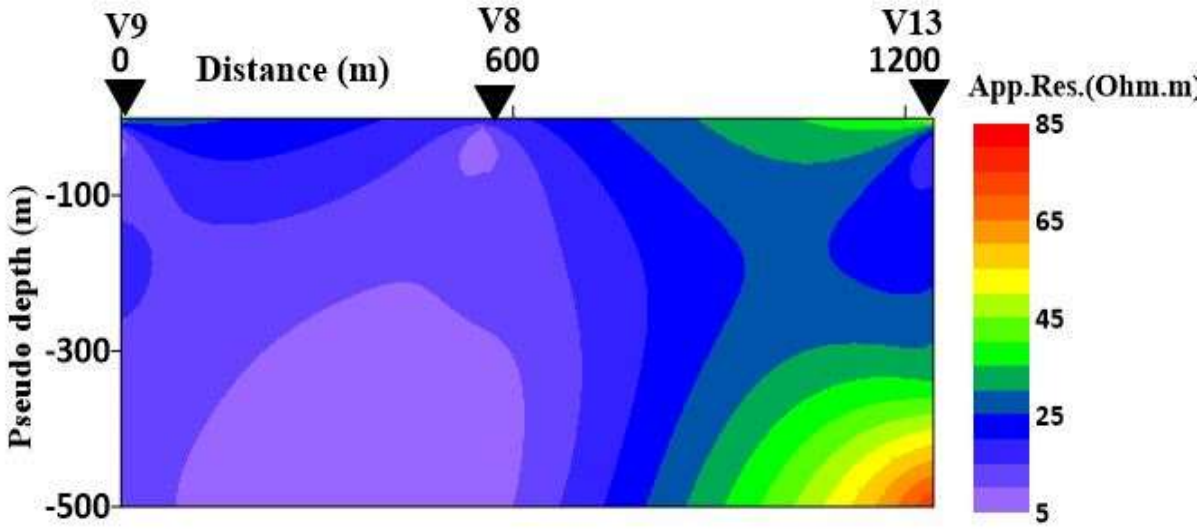

Figure 5.11: Pseudo-depth section of profile four.

B) Geoelectric section

The geoelectric section was generated using VES curve parameters, particularly from VES 13, 8, and 9 (Fig.5.12). The section shows four (4) distinct lithological units. At the topmost layer lies the topsoil, while the lower portion of VES 13 indicates fractured basalt. Conversely, the other VES sites terminate in alluvial sediments, primarily gravel with clay and sand. The top soil shows a resistivity range of (24 – 54) Ohm.m. The gravel with clay and sand has the resistivity values ranging from (5.8 – 8.6) and (4 – 6) Ohm.m. The coarse gravel has a resistivity range of (15.6 – 25) Ohm.m. On the other hand, fractured basalt shows a higher resistivity about 93 Ohm.m. The average thicknesses of the topsoil and gravel with clay and sand are approximately 3.6 meters and 31 m, respectively. Additionally, coarse gravel has an average thickness of about 108 m. The potential aquifer in this section is coarse gravel and fractured basalt. The average

depth of coarse gravel from surface is about 34 m. However, along the VES13, the depth is near surface. The average depth of fractured basalt is about 113m.

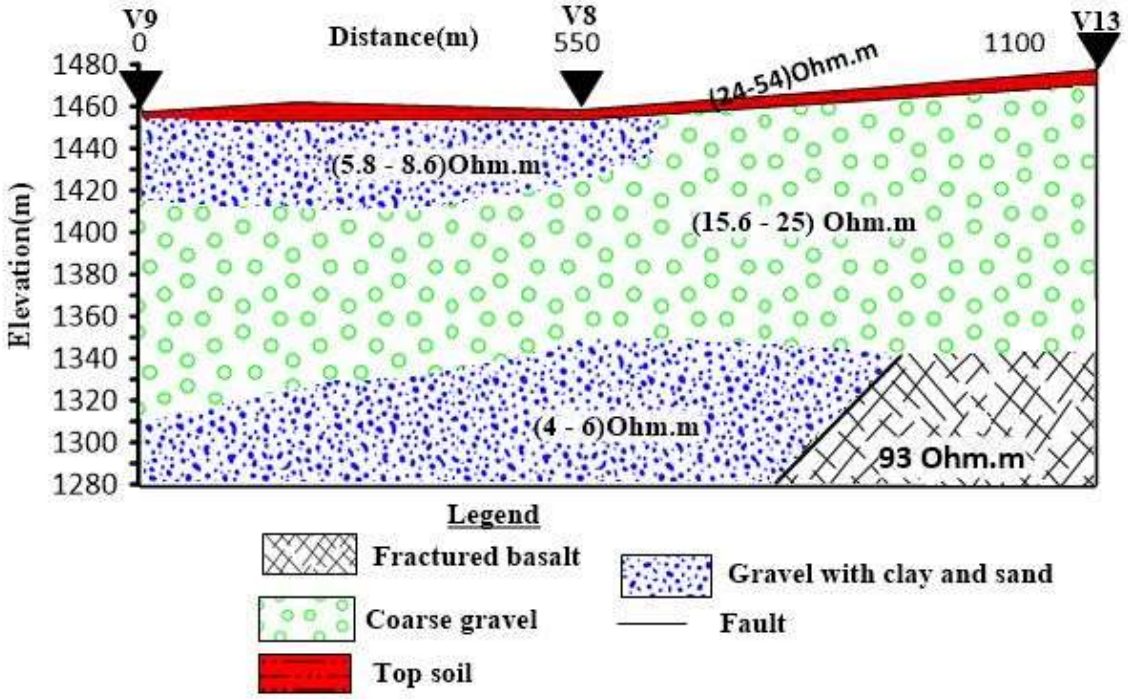

Figure 5.12: Geoelectric section of profile four.

5.3 Results and discussions of aquifer parameters

As discussed in the literature, the relationship between Dar-Zarrouk and aquifer parameter that resulted from combining the hydraulic and geoelectric parameters (equation 3.29) is important to estimate the transmissivity and hydraulic conductivity from transfer resistance. When the Kσ remain constant, the transmissivity could be estimated directly from transverse unit resistance. In the case of alluvial sediments, such as gravel, coarse sand, and sand with clay, the hydraulic conductivity of these aquifer materials decreases, and their electrical conductivity increases (Niwas & Singhal, 1981). Conversely, in the case of the fractured aquifer, the hydraulic conductivity and the electrical conductivity have a direct relationship.

According to (Okiongbo & Oborie, 2015), their study aimed to explore the connections between hydraulic and geoelectric parameters within an alluvial aquifer. They concluded that the empirical relationships between hydraulic and geoelectric parameters could effectively predict hydraulic parameters.

In this study, to derive the regression equation in the entire Harbu-Kemise graben, six (6) secondary VES data, and six (6) pumping test data, sourced from the Amhara National Regional State Water, Irrigation, and Energy Bureau, were used (Table 5.2). The relationship between transmissivity (T) and transverse resistance (TR) in Harbu – Kemise graben was derived as: $T=0.6239TR-746.18$ (Fig.5.13). The research area being a part of Harbu – Kemise graben, the equation provided was utilized to extrapolate the transmissivity and hydraulic conductivity in the study area (Table 5.3).

Table 5.2: Transmissivity, hydraulic conductivity and VES points in the Harbu-Kemise Graben from (Amhara Water, Irrigation, and Energy Bureau).

Pumping test data							VES meaurments close to the wells				
No	well name	GPS location			Trasmissivity	Haydraulic conductivity	VES ID	GPS location			Transverse resistance
		long	Lat	Elevation (m)				long	Lat	Elevation(m)	
1	HCKTW#1	39.7589	10.921	1497	24.8	0.258	VES 27	39.758053	10.9201	1449	1458
2	HCKTW#3	39.8462	10.724	1464	316	4.07	VES 19	39.841947	10.7251	1431	1950
3	HCKPW#14	39.8205	10.731	1429	355	3.08	VES 33	39.816293	10.7369	1430	1294
4	HCKPw#7	39.8279	10.726	1426	731	7.62	VES34	39.830427	10.7278	1423	2503
5	HCKTW#2	39.8014	10.695	1444	1270	13	VES 18	39.798288	10.6985	1456	2749
6	HCKPW#15	39.8316	10.719	1424	453	4.4	VES20	39.833522	10.7207	1425	2270

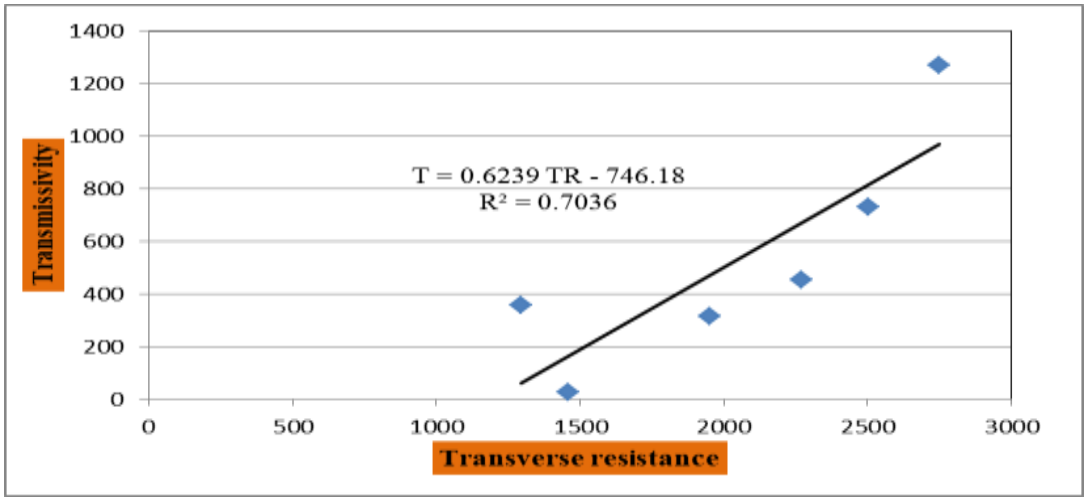

Figure 5.13: The linear relationship between transmissivity and transverse unit resistance in Harbu-Kemise graben.

Table 5.3: Estimated transmissivity and hydraulic conductivity in the study area

GPS point			VES ID	Thickness (m)	Transverse resistance	Transmissivity from pumping test	Hydraulic conductivity from pumping tes	Estimated transmissivity	Estimated hydrauic conductivity
Long	Lat								
39.7701	10.915	1478	V1	144.6	1536.4	–	–	212.4	1.5
39.7657	10.911	1476	V2	160	2110	–	–	570.2	3.6
39.7607	10.907	1478	V3	128.5	1743.2	–	–	341.4	2.7
39.755	10.903	1491	V4	115.2	1973	–	–	484.8	4.2
39.7971	10.897	1470	V5	114.7	1310	–	–	71.1	0.6
39.7719	10.898	1466	V6	120	1727	215	2.11	331.3	2.8
39.7665	10.896	1469	V7	146	2572	–	–	858.5	5.9
39.7989	10.881	1460	V8	112	1814	–	–	385.6	3.4
39.7943	10.878	1458	V9	149.9	3166.5	–	–	1229.4	8.2
39.7914	10.893	1466	V10	188.6	2582	–	–	864.7	4.6
39.7843	10.889	1461	V11	181	3484	–	–	1427.5	7.9
39.7609	10.894	1473	V12	110.6	1250	–	–	33.7	0.3
39.8047	10.883	1480	V13	137.5	2825	–	–	1016.3	7.4

In a study conducted by Soupios et al. (2007), the estimation of aquifer hydraulic parameters from surficial geophysical methods in the Keritis Basin was undertaken. The geology of the area primarily comprises Quaternary deposits. Through the correlation established between geophysical parameters derived from surface electrical measurements and aquifer parameters extracted from pumping tests, the researchers established the relationship between transmissivity and transverse resistance, which is expressed as: $T = \left(\frac{TR}{0.19}\right)^{\frac{1}{1.28}}$. Similarly, in another investigation by (Okiongbo & Oborie, 2015), the relationships between geoelectric and hydraulic parameters in a Quaternary alluvial aquifer in Yenagoa, Southern Nigeria were explored. This research aimed to understand the groundwater system in the region. The researchers noted a direct correlation between transmissivity and transverse resistance, emphasizing the interconnected nature of hydraulic and geoelectric parameters within the aquifer. This relationship was mathematically expressed as: $T = 0.18TR + 301.8$.

In this study, it was observed that there exists a direct relationship between transmissivity and transverse resistance, as illustrated in Fig.5.13. This finding suggests that higher transverse resistance values correspond to higher transmissivity within alluvial sediment. The estimated transmissivity and hydraulic conductivity values are consistent with the pumping test data within the Harbu–Kemise graben. According to the pumping test data, the transmissivity and hydraulic

conductivity values of wells in the Harbu- Kemise graben exhibit a range of (24.8-1270) m²/day and (0.258-13.3) m/day, respectively. Although model validation was not conducted, the results align with findings from other studies. Additionally, one pumping test data was utilized to assess the model's performance, as shown in Table 5.3.

To visually represent the variation of transmissivity and hydraulic conductivity across the area, grid maps were generated (Fig. 5.14 and 5.15). These figures illustrate that both estimated hydraulic conductivity and transmissivity values are notably high in the southern region of the research area. Conversely, the northeastern and southwestern sections exhibit lower values. This suggests that the southern part of the research area holds promising potential for supplying a significant amount of groundwater to wells.

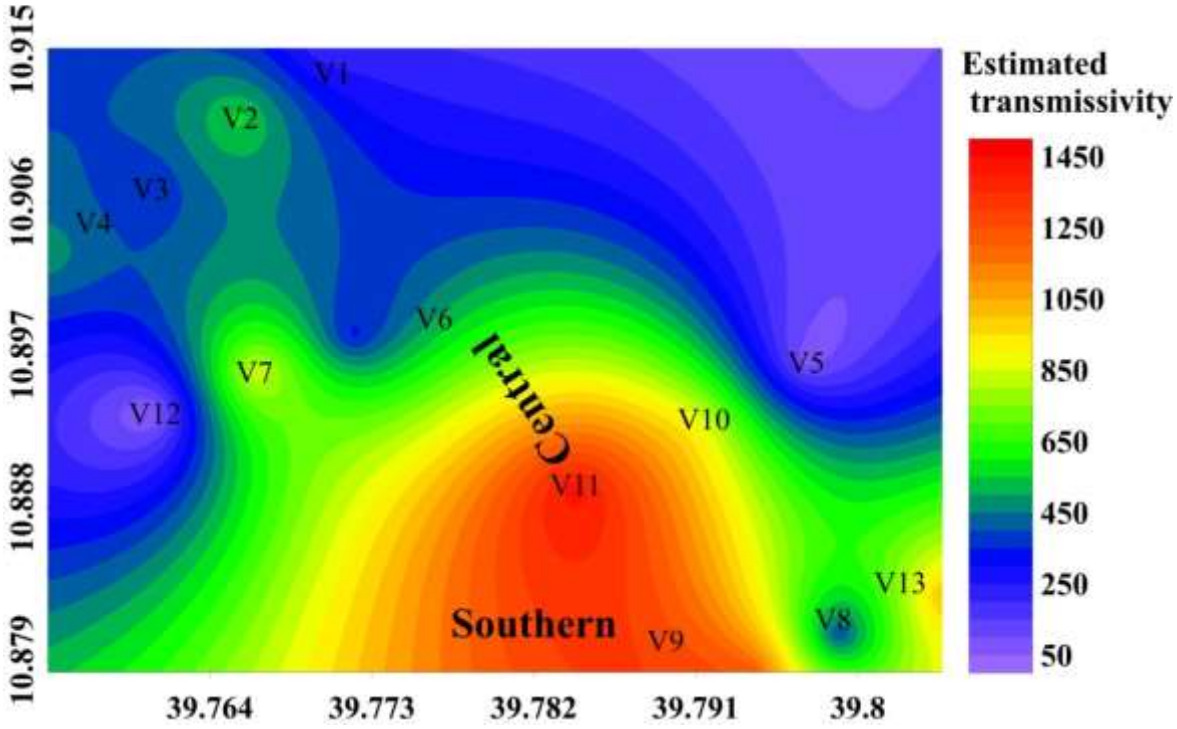

Figure 5.14: Estimated transmissivity.

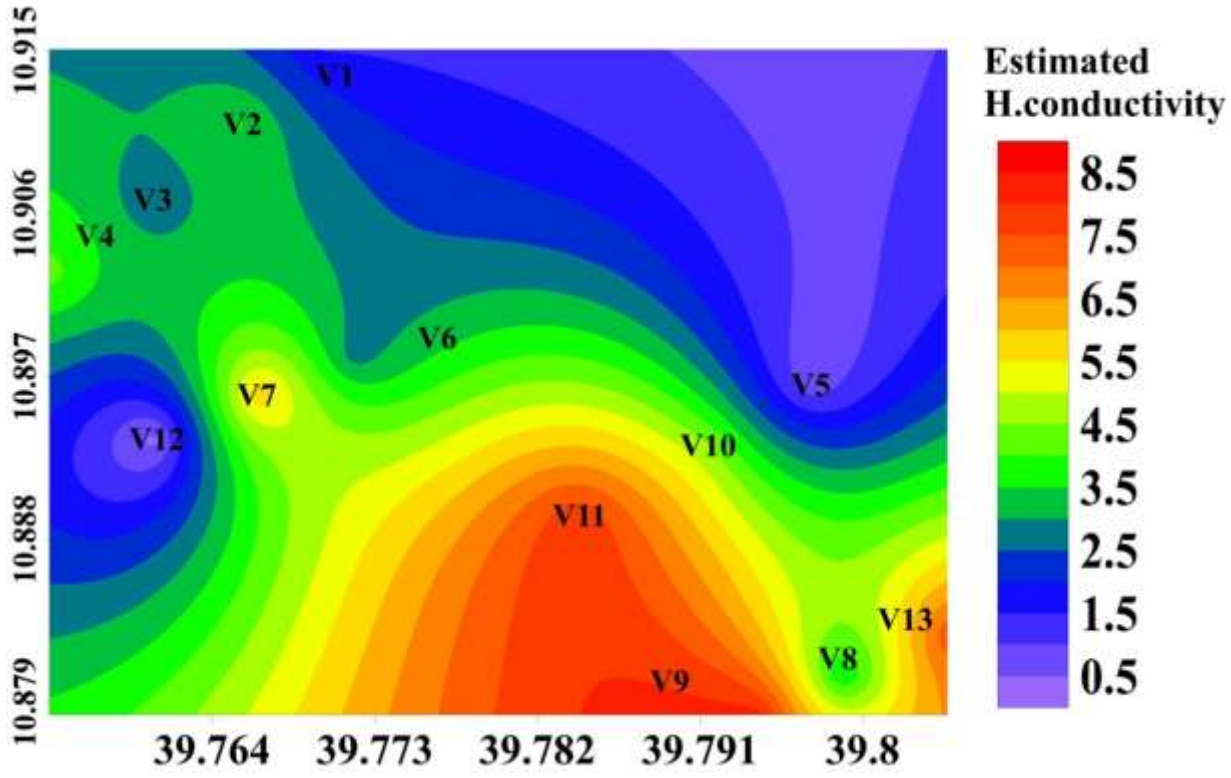

Figure 5.15: Estimated hydraulic conductivity.

5.4 Results and discussions of magnetic

5.4.1. Interpretation of total magnetic anomaly along profile (E- E')

The profile map was created after removing for the effects of the IGRF and diurnal variation. It shows a one-dimensional variation of the total magnetic field anomaly along a selected profile. In this preparation, the vertical axis represents the total magnetic anomaly, while the horizontal axis represents distances (Fig. 5.16). The eastern region of the research area exhibits a low total magnetic anomaly, as shown in Fig 5.17. Conversely, the central part of the research area displays a high magnetic anomaly value. This indicates that there is a highly magnetized body in the eastern part of the investigation area as compared to the central part.

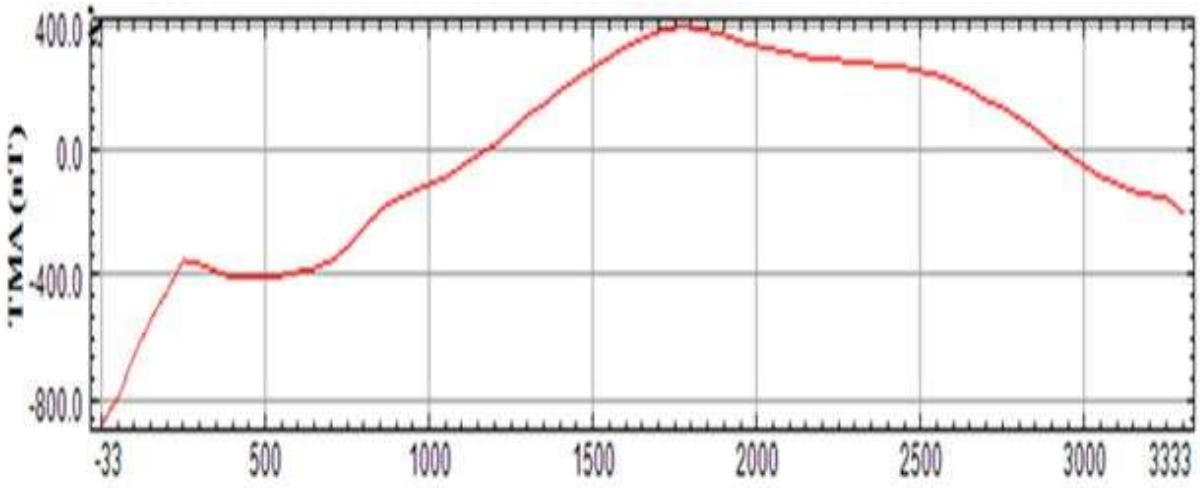

Figure 5.16: Total magnetic anomaly along profile (E−E').

5.4.2. Results of different anomaly maps

5.4.2.1 The total magnetic field anomaly map

The total magnetic anomaly of the region has been calculated by subtracting IGRF from the total magnetic intensity. The IGRF value for the area was obtained from the IGRF model (13th generation).

In this study, the Total Magnetic Anomaly map was generated following the exclusion of diurnal variation and IGRF or main field influences from field-collected data. As illustrated in Fig.5.17, the map displays low anomalies in the eastern and western sections of the research area. In regions closer to the equator or at low latitudes, highly magnetized bodies yield negative responses. Due to this reason, the eastern and western sections of the study area exhibit highly magnetized bodies. Conversely, the central part of the research area is characterized by low-magnetized bodies.

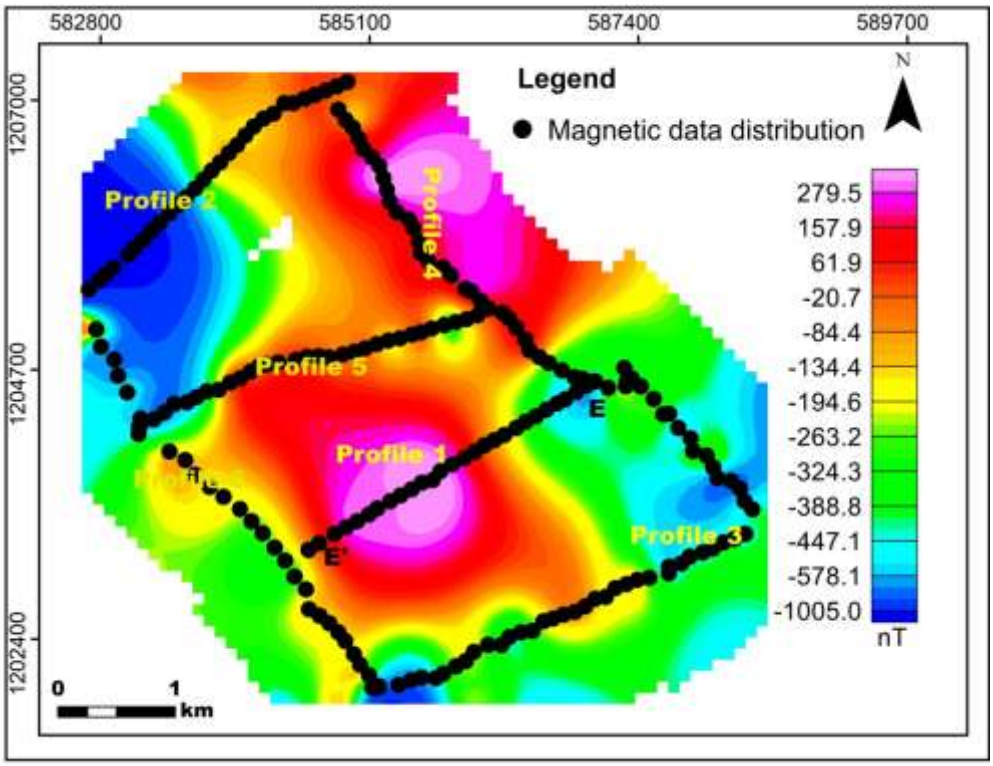

Figure 5.17: Equator reduced total magnetic field anomaly map.

5.4.2.2 Residual anomaly map

The magnetic field value measured in the field comprises two overlapping components: regional and residual anomalies. The low-frequency anomalies offer insights into the sources is at a significant depths, while the residual anomaly component shows the shallow depth (Satiawan, 2009). As stated by Rusman et al. (2023), interpreting geomagnetic anomaly data poses challenges due to the effect of the dipole magnetic field of Earth. To address this issue, the researcher employed the Reduced Equator (RTE) method to obtain the monopoles.

In this study, to isolate the magnetic field originating from shallow features the upward continuation with (800) m was employed. Following the removal of magnetic signals from deep-seated features, further analysis was conducted to reduce anomalies near the equator. Fig 5.18 illustrates a higher anomaly signature corresponding to the central part of the study area. This may be due to the presence of a weak zone or alluvial sediment. Additionally, the anomaly trend in a northeast-southwest direction is high. This may be due to the presence of an elongated, low magnetized body in the central part of the research area.

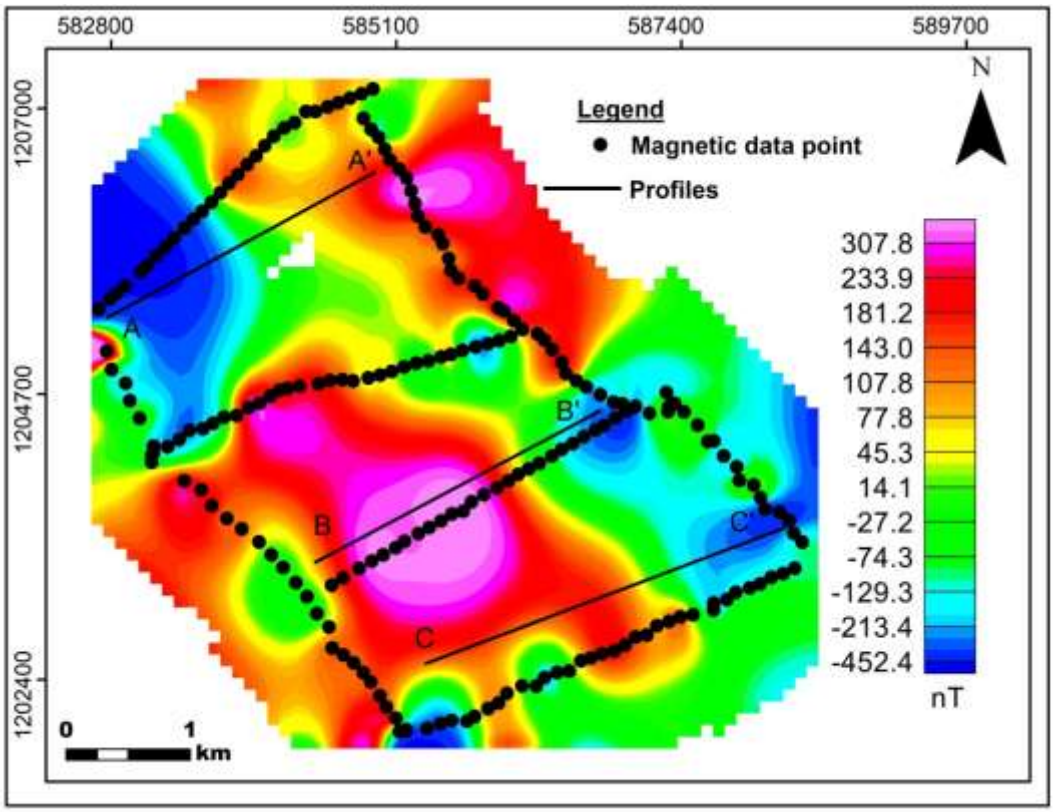

Figure 5.18: Equator-reduced residual anomaly map.

5.4.2.3 Tilt angle derivative map

The TDR technique is applied in mineral exploration to map shallow geological structures, as it is good at identifying the boundaries of magnetic source bodies (Salawu et al., 2019). The method was first outlined by (Miller & Singh, 1994) and presented as:

$$\theta = TDR = tan^{-1}\frac{\frac{\partial T}{\partial z}}{\sqrt{\left(\frac{\partial T}{\partial X}\right)^2 + \left(\frac{\partial T}{\partial y}\right)^2}}$$

Where T is residual magnetic field anomaly and TDR is tilt derivative.

In the transformation to reduced-to-equator coordinates, the TDR's amplitudes are negative over magnetic source bodies and positive outside of them (Verduzco et al., 2004).

The TDR method aids in identifying the horizontal positioning of magnetic source body edges within the study region. Zero contours on the TDR map mark locations where sharp transitions occur in magnetic susceptibilities between negative and positive magnetic source bodies. As a

result, these zero contours on the TDR map serve as indicators of faults or contact boundaries (Salawu et al., 2019).

In this study, to determine the magnetic signature arising from linear geological features such as faults and weak zones, the tilt derivative technique was employed. As shown in Fig 5.19, it delineates variation along the boundary separating the central, eastern, and western regions of the study area. The zero contours indicate either the contact between the basement (igneous rock) and alluvial sediment or the presence of a weak zone (fault).

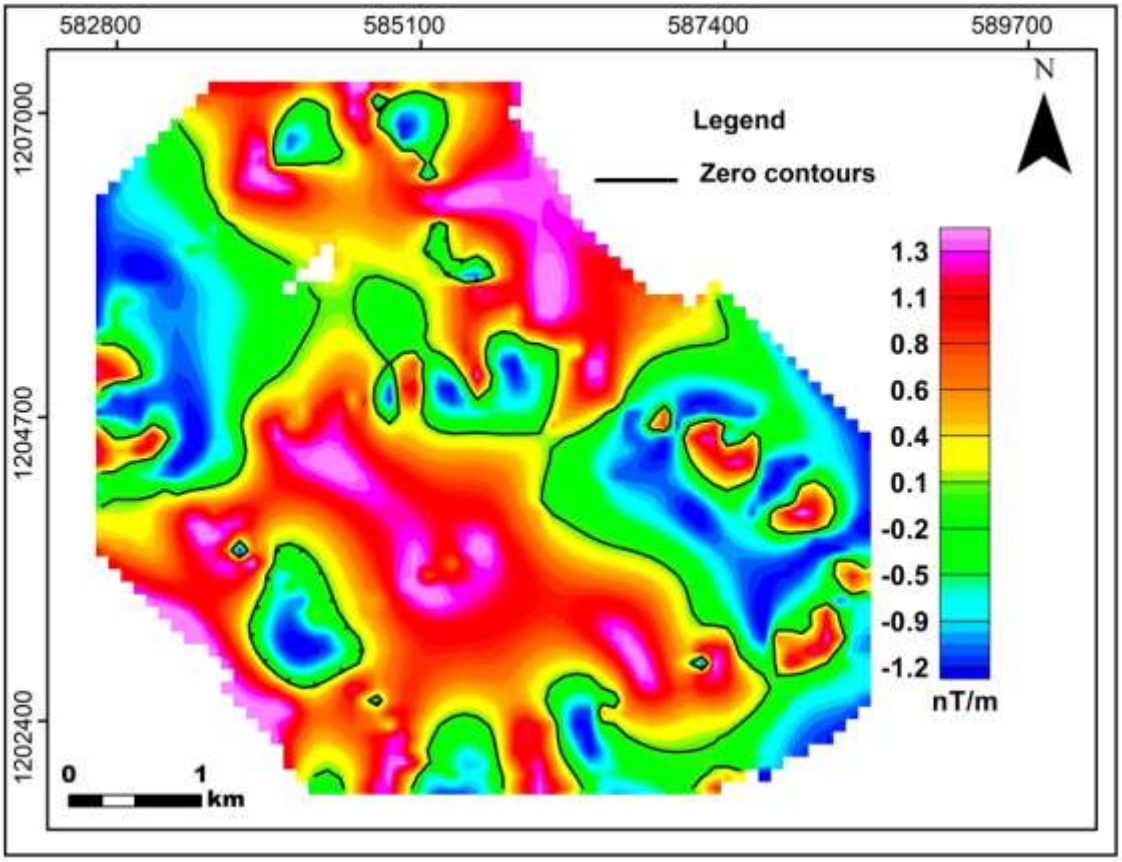

Figure 5.19: Tilt derivative map.

5.4.2.4 Analytic Signal Map

According to Roest et al. (1992) the amplitude expression for the analytical signal (AS) of 3D structures, is expressed as bellows.

$$AS = \sqrt{\left(\frac{\partial T}{\partial X}\right)^2 + \left(\frac{\partial T}{\partial Y}\right)^2 + \left(\frac{\partial T}{\partial Z}\right)^2}$$

Analytic signal filter is not depending on the inducing magnetic field direction so that the anomalies peak is distributed immediately above the source body (Lingerew Nebere, 2017). In order to map or detect the edge of the magnetic sources and for identifying geological boundaries due to their sensitivity to anomalous source boundaries, analytic signal filter is important tool (Muzaffer & Dikmen, 2013).

In this study the analytic signal filter is employed, to delineate the edges of geological features and identify geological contacts in three directions. As showed in the Fig 5.20, it effectively shows the variation between the central, eastern, and western sections of the research area. Particularly important is the distinct delineation of alluvial sediment in the central region, clearly visible on the map. In analytic map, the high magnetic anomaly indicates near source. Conversely, the low magnetic anomaly indicates far from source. Due to this reason the low magnetic anomaly in central part of study area insight that the depth of alluvial sediment is high as compared to north western and southeastern part of the research area.

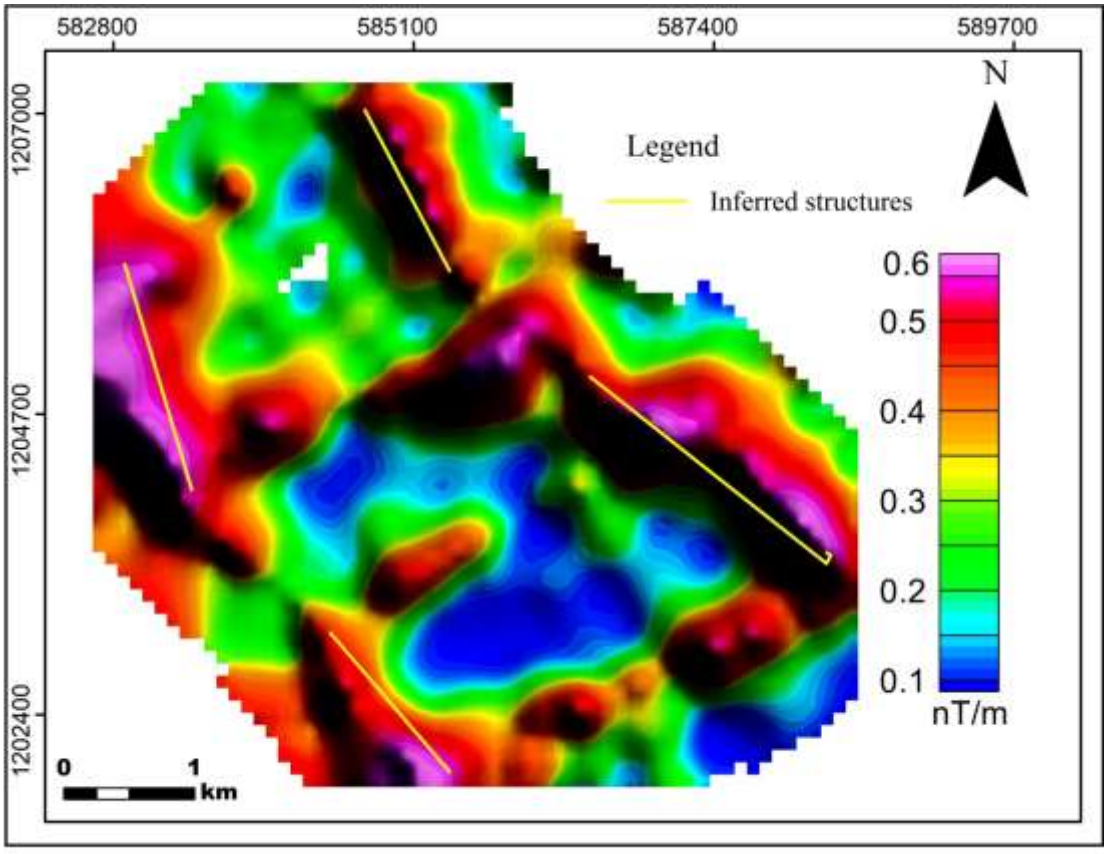

Figure 5.20: Analytic signal map.

5.4.3 Euler deconvolution and 2D magnetic model

5.4.3.1 Euler deconvolution map

This technique used to enhance data for estimating the location and depth of magnetic anomaly sources. It connects magnetic field and gradient components to locate anomaly sources, utilizing a structural index to measure their homogeneity. This technique is effective for identifying anomalies from both isolated and multiple sources (Eldawi et al., 2004). This method is practiced at delineating the depth of geological contacts and dykes. Typically, the structural index (N) remains constant, enabling the determination of the locations and depths ($x_\circ$,$y_\circ$, $z_\circ$) of causative geologic sources (Naheem et al., 2019). Mathematically expressed as follows:

$$(X - x_\circ)\frac{\partial T}{\partial X} + (Y - y_\circ)\frac{\partial T}{\partial Y} + (Z - z_\circ)\frac{\partial T}{\partial Z} = N(B - T)$$

Where ($x_\circ$,$y_\circ$, $z_\circ$) denotes the location of a source where the total field T is detected at coordinates (X, Y, Z). Here, B represents the regional value of the field, and N stands for the structural index (SI). As Hilemichaeil Samson et al. (2024) stated, the depth of the source of magnetic and gravitational anomalies is crucial in geophysical interpretation of subsurface structures. To understand the subsurface structure of the area, they employed 3D Euler deconvolution and radially averaged power spectrum analysis.

Table 5.4: Structural indices for magnetic methods (Naheem et al., 2019).

S/N	Source type (model)	SI
1	Contact of considerable depth extent	0
2	Thin sheet edge (sill, dyke, etc.)	1
3	Line source (pipeline, narrow kimberlite pipe, etc.)	2
4	Sphere or compact body at a distance	3

This study involves the preparation of Euler 3D deconvolution maps derived from the residual magnetic grid. These maps provide insights into the location, characteristics, and depth of causative bodies. Following visual inspection and clustering of depth solutions, SI values of 0, indicating magnetic contact, were selected.

As shown in Fig. 5.21, the depth of contact in the eastern and western parts of the research area is characterized by lower depths compared to the central region. This may due to variation of sediment thickness in the research area. The results of the 3D Euler deconvolution align well with the 2D section (Fig. 5.24).

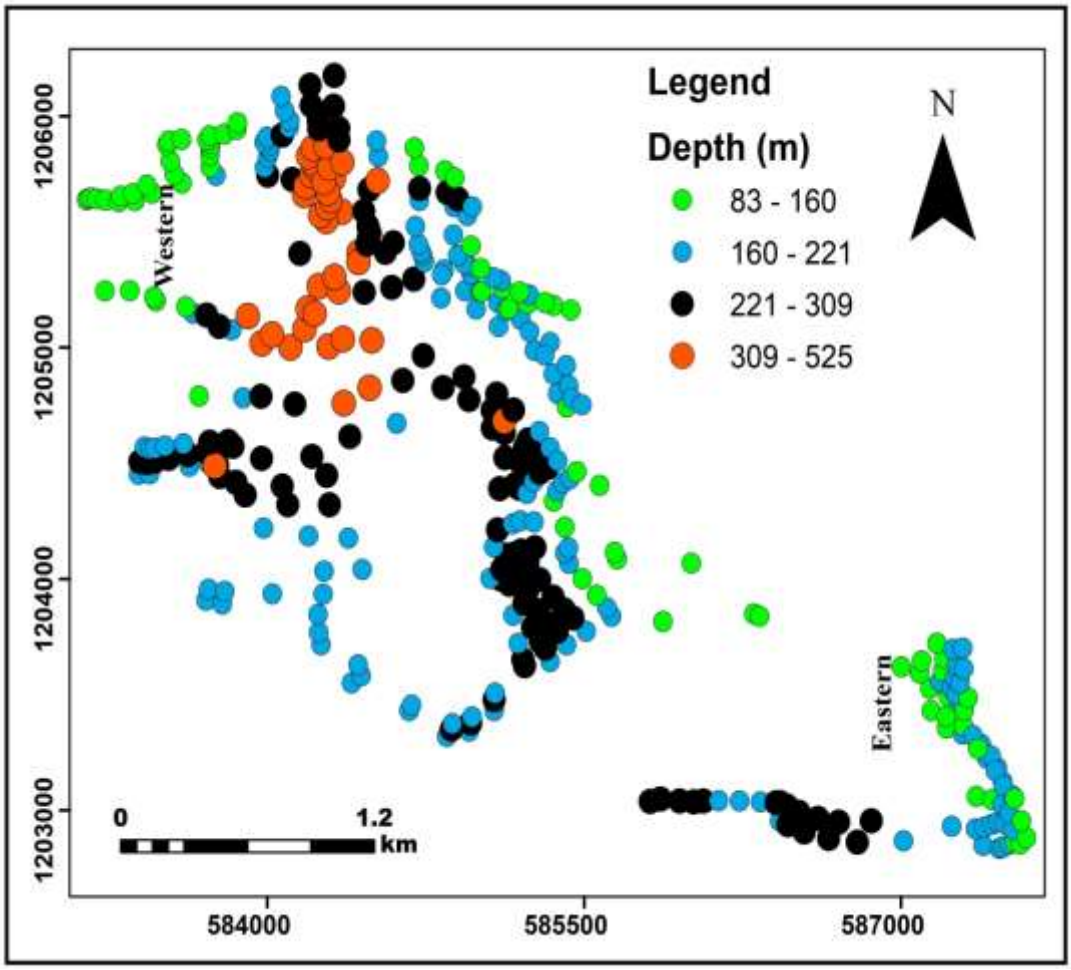

Figure 5.21: Euler deconvolution map.

5.4.3.2 2D magnetic model

A 2D model constrained by geophysical and borehole data was constructed utilizing a residual magnetic anomaly map. The residual anomaly values were extracted along three profiles running across the study area (Fig.5.18). These 2D magnetic models aimed to delineate sediment thickness variations and identify structures within the area. To mitigate the non-uniqueness of geophysical modeling, incorporating prior information such as geological and geophysical data is vital. In the process of 2D magnetic modeling, the result of borehole data (Table 5.5), VES

curves (Table 5.7), and depth estimations obtained from Euler deconvolution (Table 5.6) were integrated to effectively constrain the magnetic data.

Table 5.5: Geological unit depth from borehole data (Amhara Water, Irrigation, and Energy Bureau).

no	Long	Lat	ID	Depth	Geological unit
1	39.78664	10.88724	HCKTW#*1*	0-210	Alluvial sediment
				>260	Basalt
2	39.776476	10.901187	HCKTW#4	0-320	Alluvial sediment

Table 5.6: The depth of geological contact from Euler deconvolution.

no	Location in the study area	Depth
1	Eastern and western	83-221
2	central part	309-500

Table 5.7: Depth of geological unit from VES curve model.

no	Location		VES name	depth	geological unit
	Long	Lat			
1	39.75495	10.902663	V4	0-120	Alluvial
				> 120	Basalt
2	39.79713	10.896566	V5	0-116	Alluvial
				>116	Basalt
3	39.76094	10.893562	V12	0-110	Alluvial
				>110	Basalt
4	39.80471	10.882842	V13	0-137	alluvial
				>137	basalt

In this study, GM-SYS, a 2D modeling software was employed to calculate magnetic responses derived from a user-defined geological mode (Table 5.6).

Table 5.8: The prior information to develop the forward model.

no	geological unit	susceptibility in SI unit	magnet inclination	magnetic declination	IGRF	Depth(m)
1	alluvial sediment	0.0001	8	2.5	36537	0-300
2	Basement (basalt unit)	0.5	8	2.5	36537	300-600

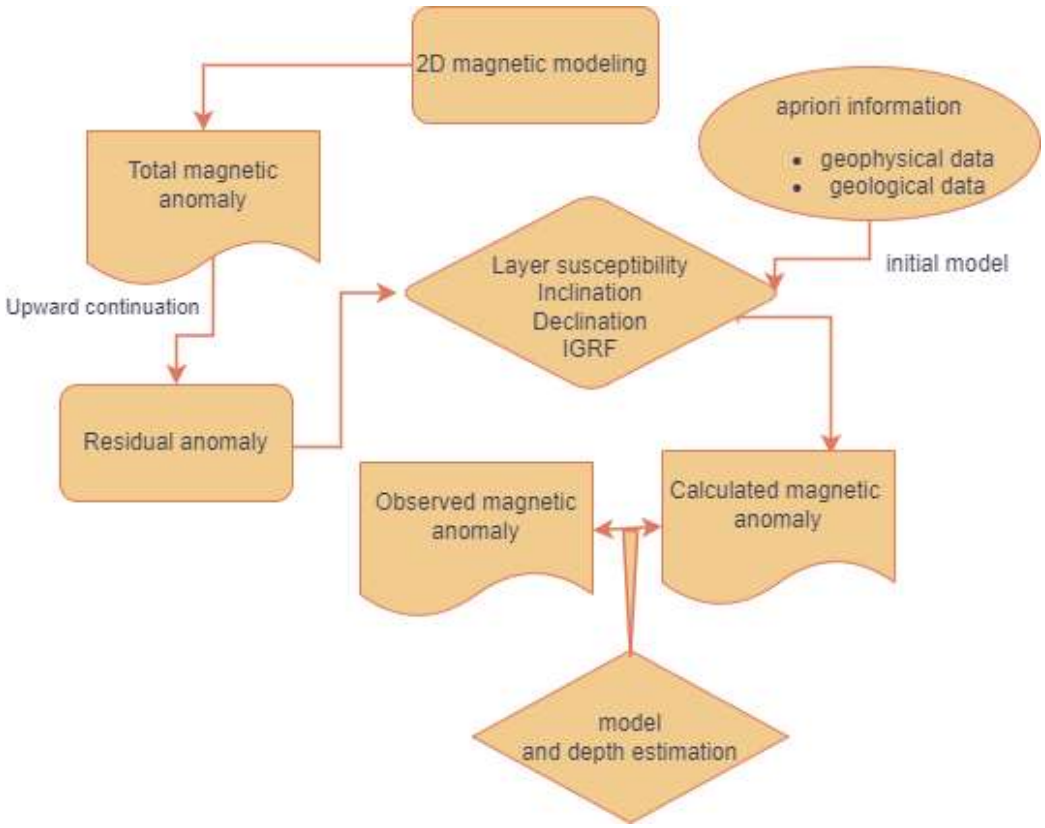

Figure 5.22: The general steps to prepare a 2D magnetic model.

A) 2D magnetic section along profile (A-A')

The purpose of choosing profile sections from the residual anomaly (Fig. 5.18) is to illustrate the distribution of sediment over the basement unit. In the developed 2D model (Fig.5.23), two susceptibility layers were taken into account. As shown in Figure, the sediment thickness is high in the central portion of the research area compared to the western section. Moreover, the model

effectively shows the variations in sediment distribution across the entire study area. The maximum and minimum thickness of the sediment is approximately 400 m and 150 m respectively. There is also an inferred fault that dips towards the east.

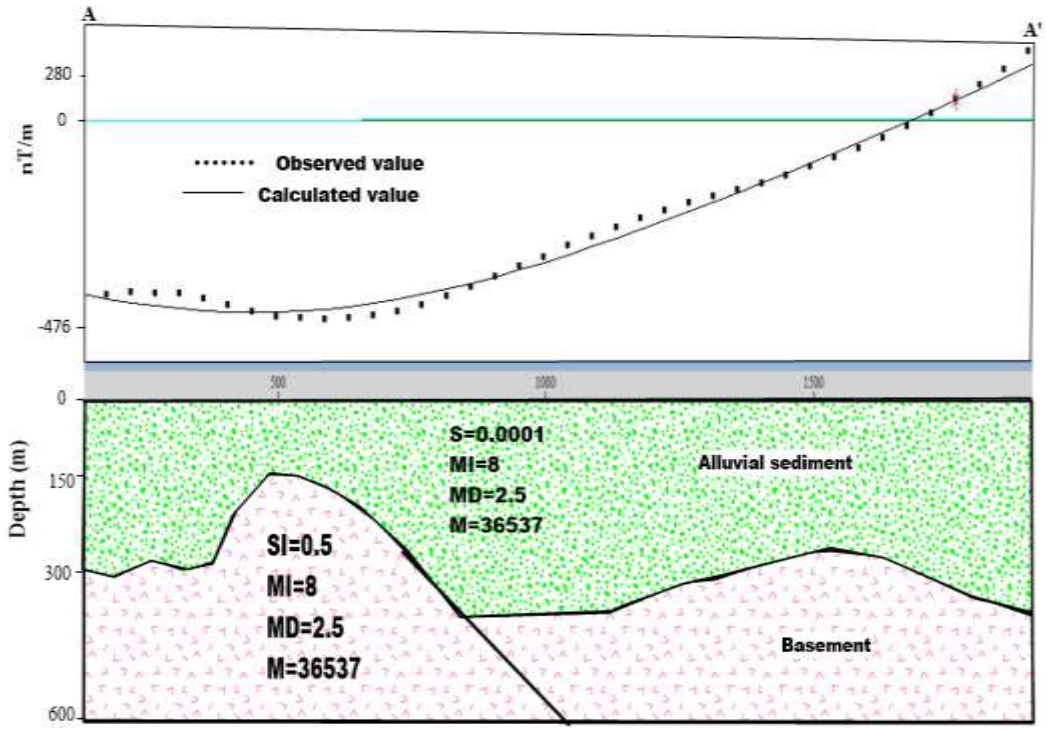

Figure 5.23: 2D magnetic section along profile (A-A').

B) 2D magnetic model along profile (B - B')

While preparing the 2D model (Fig.5.24), two susceptibility layers were taken into account. As shown in the figure, the sediment thickness is significantly lower in the eastern portion of the research area compared to the central section. In addition, the model effectively shows the variations in the sediment thickness across the entire research area. The model shows the existence of faults those dipping towards to central part. The maximum and minimum thickness of the sediment is approximately 380 m and 130 m respectively. There is also an inferred fault that dips towards the center.

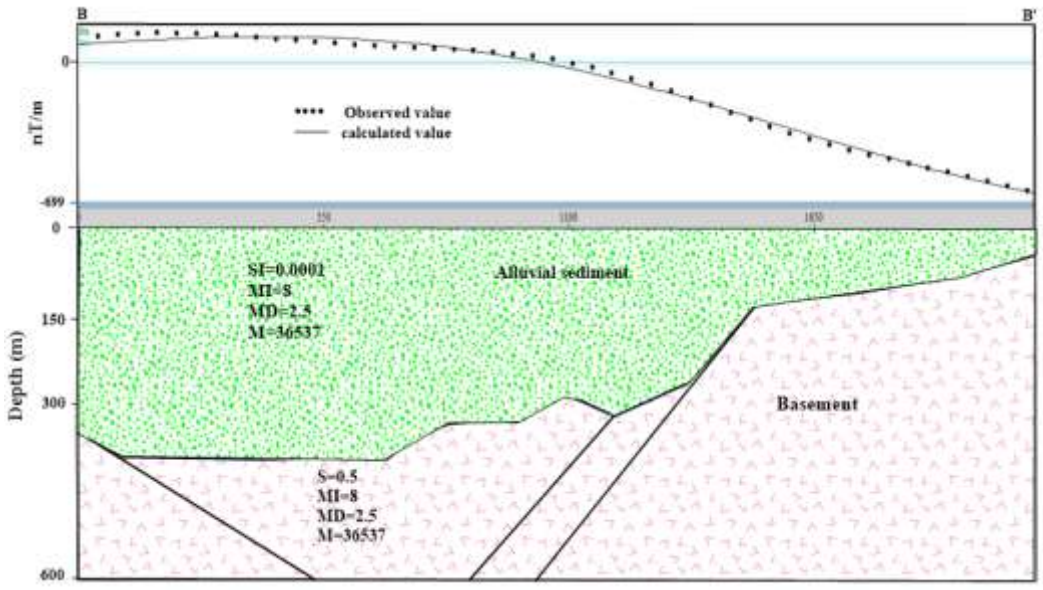

Figure 5.24: 2D magnetic section along profile (B - B').

C) 2D magnetic model along profile (C - C')

The 2D model (Fig.5.25) illustrates the undulation of sediment and the depth variation of the basement from the surface. In this developed 2D model, two susceptibility layers were considered. As shown in the figure, the depth of the basalt unit significantly varies with depth to the surface, particularly in the central section compared to the eastern section. The maximum and minimum thickness of the sediment is approximately 310 m and 140 m respectively. There is also an inferred fault that dips towards the east and west.

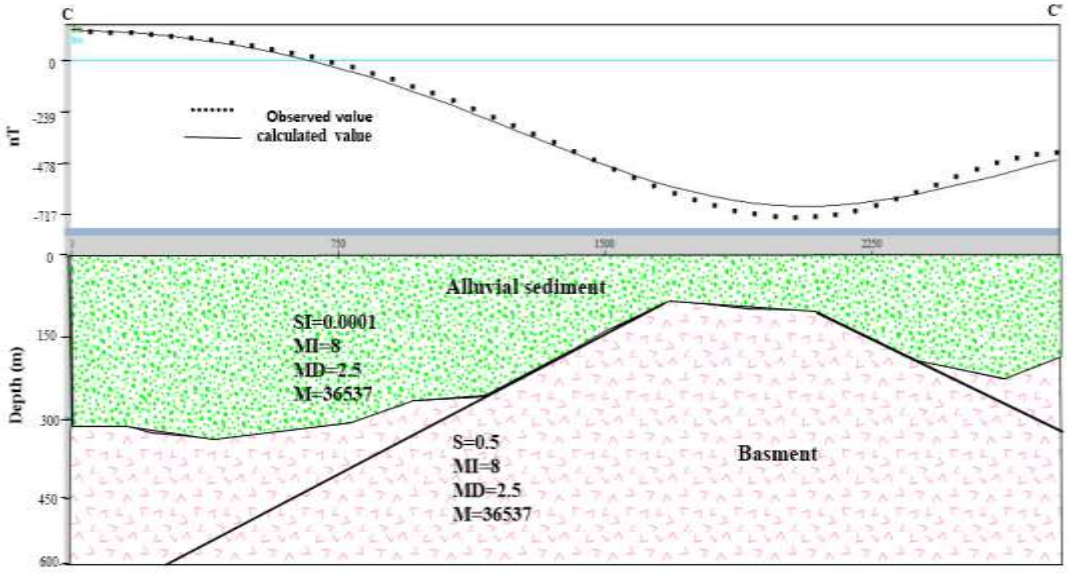

Figure 5.25: 2D magnetic section along profile (C - C').

CHAPTER VI

CONCLUSION AND RECOMMENDATION

6.1 Conclusion

In the present study, the two geophysical surveys, namely VES, and magnetic surveys, are utilized to find out the depth and thickness of water-bearing horizons. This study proves that the surface geoelectrical method, specifically the VES technique, is a useful, cost-effective, and efficient tool for estimating aquifer hydraulic properties such as transmissivity and hydraulic conductivity.

The low residual magnetic anomaly observed in the eastern and northwestern parts of the area suggests that the basement rock is shallower in these regions compared to the central part. This interpretation is supported by the tilt map which identifies a NE-SW trending fault or boundary between the basement rock and the overlying sediment. The results from the magnetic 2D sections and geoelectric sections indicate that the sediment thickness is greatest in the central part of the study area. According to the 2D magnetic section results, the average sediment thickness in the central section is approximately 363 meters. In contrast, the sediment thickness in the eastern sections is about 135 meters. The four pseudo-depth sections also show that the central part of the investigation area corresponds with low apparent resistivity. Especially, at a depth of AB/2 500 m the eastern and western part of the research area is characterized by high apparent resistivity.

The geoelectric sections reveal the variations in the depth of potential aquifers in the research area. In VES 1, 12, 13, 11, and 10, the depth of the potential aquifer is approximately less than ten (10) m. However, in VES 9, 2, and 5, the depth of the potential aquifer is between 40 and 50 meters. In VES 1, 4, 3, 6, 8, and 7, the depth of the potential aquifer ranges between 28.3 and 36.1 m. These results emphasize the significant variability in the depth of potential aquifers across the study area. Subsequently, using the results of the two geophysical surveys, the eastern and western part of the study area is delineated as a good groundwater potential zone compared to the central parts of the study area.

6.2 Recommendation

Based on the findings of this study, the following recommendations are suggested

1) The results of this study reveal the presence of a fractured basalt in the eastern and western parts of the study area. Therefore, it is recommended that future boreholes be drilled in these surrounding areas to achieve better groundwater yield.

2) In the central part of the study area, a significant low resistivity was observed at approximately 130 meters depth. It is recommended to conduct further investigations to assess groundwater salinity in this region.

3) To enhance the precision of aquifer parameter estimation through the integration of geophysical methods with pumping test data, increasing the number of VES data points is recommended.

4) To comprehensively understand the nature of the structures governing groundwater movement across the entire Borkena catchment and its interactions with neighboring hydrological systems, conducting an integrated geophysical investigation of the full Borkena catchment is recommended.

REFERENCE

Abbate E., Bruni, P., & Sagri, M. (Eds.). (2015). Geology of Ethiopia: a review and geomorphological perspectives, 33- 64.

Adli, Z. H., Musa, M. H., & Arifin, M. K. (2010). Electrical resistivity of subsurface: Field and laboratory assessment. International Journal of Geological and Environmental Engineering, 4(9), 422-425.

Akhter, G., & Hasan, M. (2016). Determination of aquifer parameters using geoelectrical sounding and pumping test data in Khanewal District, Pakistan. Open Geosciences, 8(1),631-638.

AL-Khafaji, W. M. S. (2014). Lecture note of electrical geophysical methods, 1- 66.

Alebachew Beyene, &, Abdelsalam, M.G. (2005). Tectonics of the Afar Depression: A review and synthesis. Journal of African Earth Sciences, 41(1-2), 41-59.

Alzahrani, H., Abdelrahman, K., & Hazaea, S. (2022). Use of geoelectrical resistivity method for detecting near-surface groundwater potential zones at Riyadh city, Saudi Arabia. Journal of King Saud University - Science, 34(7), 1- 7.

Baker, B. H., Mohr, P. A., & Williams, L. A. J. (1972). Geology of the eastern rift system of Africa (Vol. 136). Geological Society of America.

Barberi, F., & Santacroce, R. (1980). The Afar Stratoid Series and the magmatic evolution of East African rift system. Bull. Soc. Geol. Fr, 22, 891-899.

Barberi, F., Tazieff, H., & Varet, J. (1972). Volcanism in the Afar depression: its tectonic and magmatic significance. Tectonophysics, 15(1-2), 19-29.

Berhe, S. M., Desta, B., Nicoletti, M., & Teferra, M. (1987). Geology, geochronology and geodynamic implications of the Cenozoic magmatic province in W and SE Ethiopia. Journal of the Geological Society, 144(2), 213-226.

Chandra, S., Ahmed, S., Ram, A., & Dewandel, B. (2008). Estimation of hard rock aquifers hydraulic conductivity from geoelectrical measurements: A theoretical development with field application. Journal of Hydrology, 357(3-4), 218-227.

Chatterjee, R., Tarafder, G., & Paul, S. (2010). Groundwater quality assessment of Dhanbad district, Jharkhand, India. Bulletin of Engineering geology and the Environment, 69, 137-141.

Chorowicz, J. (2005). The East African rift system. Journal of African Earth Sciences, 43(1-3), 379-410. https://doi.org/10.1016/j.jafrearsci.2005.07.019

Coker, J. O. (2012). Vertical electrical sounding (VES) methods to delineate potential groundwater aquifers in Akobo area, Ibadan, South-western, Nigeria. Journal of Geology and Mining Research, 4(2), 35-42.

Dereje Ayalew. (2022). The relations between felsic and mafic volcanic rocks in continental flood basalts of Ethiopia: implication for the thermal weakening of the crust. Geological Society, London, Special Publications, 357(1), 253-264. https://doi.org/10.1144/sp357.13

Dereje Ayalew, Worash Getaneh, raphael, P., Balemwal Atnafu, Addise Zemelak, & Endayne Belay. (2021). Stratigraphic framework of the northeastern part of the Ethiopian flood basalt province. Bulletin of Volcanology, 83, 1-13. https://doi.org/10.1007/s00445-021-01482-z

Diaz, A., & Martinez, S. (2019). Advances in groundwater potential mapping. Hydrogeology Journal, 27(7), 2307-2324. https://doi.org/10.1007/s10040-019-02001-3

Dor, N., Syafalni, S., Abustan, I., Rahman, M. T. A., Nazri, M. A. A., Mostafa, R., & Mejus, L. (2011). Verification of surface-groundwater connectivity in an irrigation canal using geophysical, water balance and stable isotope approaches. Water resources management, 25, 2837-2853.

El Makrini, S., Boualoul, M., Mamouch, Y., & El Makrini, H. (2022). Vertical Electrical Sounding Technique to Map Potential Aquifers of the Guigou Plain (Middle Atlas, Morocco). Applied Sciences, 12(24), 2- 16. https://doi.org/10.3390/app122412829

Eldawi, M., Tianyou, L., Hui, S., & Dapeng, L. (2004). Depth estimation of 2-D magnetic anomalous sources by using Euler deconvolution method. American Journal of Applied Sciences, 1(3), 209-214.

Esubalew Yehualaw, Tigistu Haile, & Wubamlak Nigusse. (2023). Groundwater Potential Mapping Using Geophysical Techniques: a Case Study in Hosanna Area, Western Margin of The Central Main Ethiopian Rift, Ethiopia. Journal of Economic Research & Reviews, 3(3), 192-195. https://doi.org/10.33140/jerr.03.03.05

Getachew Tsigie. (2015). Evaluation of Groundwater Resource Potential in Borkena River Catchment, Awash Basin Getachew Tsigie, (2015). Evaluation of Groundwater Resource

Potential in Borkena River Catchment, Awash Basin Department of Water Resource and Irrigation Engineering, Institute of Technology, Arba Minch University.

Gobezie Wallelegn, Teferi Ermias, Dile Yihun, Bayabil Haimanote, Ayele Gebiaw & Ebrahim Girma. (2023). Modeling Surface Water–Groundwater Interactions: Evidence from Borkena Catchment, Awash River Basin, Ethiopia. Hydrology, 10(2), 2- 8.

Griffiths, D. H., & King, R. F. (2013). Applied geophysics for geologists and engineers: the elements of geophysical prospecting. Elsevier, 1- 222.

Hammond, J. O. S., Kendall, J. M., Stuart, G. W., Keir, D., Ebinger, C., Ayele, A., & Belachew, M. (2011). The nature of the crust beneath the Afar triple junction: Evidence from receiver functions. Geochemistry, Geophysics, Geosystems, 12(12), 1- 22.

Hansen, R., Racic, L., & Grauch, V. (2005). Magnetic methods in near-surface geophysics. In Near-surface geophysics. Society of Exploration Geophysicists, 151-176).

Hasen Hussien, Zerihun Asmelash, Andualem Shigute & Abreham Bekele. (2022). Assessment of surface water resources Based on Different growth scenarios, for borkena river sub-basin, awash river basin, ethiopia. Jordan Journal of Earth and Environmental Sciences, 13 (3), 199-214, 199-214.

Herman, R. (2001). An introduction to electrical resistivity in geophysics. American Journal of Physics, 69(9), 943-952.

Hilemichaeil Samson, Tigistu Haile, & Gezahegn Yirgu. (2024). Integrated geophysical methods to constrain subsurface structure of Tulu Moye-Bora-Bericha axial volcanic complex, Main Ethiopia Rift: implications for geothermal resources. *Elsevier Ltd*, *10*(7), 1- 20.

Hofmann, C., Courtillot, V., Feraud, G., Rochette, P., Gezahegn Yirgu., Ketefo, E., & Pik, R. (1997). Timing of the Ethiopian flood basalt event and implications for plume birth and global change. . Nature, 389(6653), 838-841.

Kazmin, V. (1979). Stratigraphy and correlation of Cenozoic volcanic rocks in Ethiopia. Reports of Ethiopian Institute of Geological Survey, 106, 1-26.

Kazmin, V., & Garland, C. (1973). Evidence of Precambrian block-faulting in the western margin of the Afar depression, Ethiopia. Geological Magazine, 110(1), 55-57.

Kearey, P., Brooks, M., & Hill, I. (2002). An introduction to geophysical exploration.John Wiley & Sons, 1- 262.

Kieffer, B., Arndt, N., Lapierre, H., Bastien, F., Bosch, D., Pecher, A., Gezahegn, Y., Dereje, A., Weis, D., Jerram, D. A., Keller, F., & Meugniot, C. (2004). Flood and Shield Basalts from Ethiopia: Magmas from the African Superswell. Journal of Petrology, 45(4), 793-834.

Kunetz, G. (1966). Principles of direct current-Resistivity prospecting.

Layade, G., Oluyinka, Edunjobi, H. O., Ajayi, K. D., & Anifowoshe, M. M. (2023). Qualitative, Lineation and Depth Evaluation of Potential Field Signatures in the Abeokuta Region, Southwestern Nigeria, 1- 38.

Lindsay, R. B. (1940). William gilbert and magnetism in 1600. American Journal of Physics, 8(5), 271-282.

Lingerew Nebere. (2017). Reduction to the Pole and analytic signal interpretation techniques of magnetic data in equatorial erea, Ethiopia. International Journal of Scientific Engineering and Research, 5(7), 466- 468.

Lowrie, W. (2007). fundamentals of geophysics Cambridge University Press, 1- 381.

Lowrie, W., & Fichtner, A. (2020). Fundamentals of geophysics. Cambridge university press, 1-393.

Mark, E. (2013). Near-surface applied geophysics. Cambridge University Press. Cambridge University Press, Cambridge,1- 403.

Meindinyo, R., Utuedeye, O., & Adedokun, I. (2017). Vertical electrical sounding (Ves) for the determination of under ground resistivity in part of Nigeria Wilberforce Island, Amassoma, Bayelsa State. IOSR Journal of Research & Method in Education, 7(2), 53-61.

Melkamu Adimaw, Murugesan Bagyaraj, Tewabe Melkamu and Yohannes Gashu. (2020). Aquifer characterization and groundwater flow dynamics in the upper left bank of Jemma River catchment, Blue Nile Basin, Ethiopia. Arabian Journal of Geosciences, 13(13),1-11.

Miller, H. G., & Singh, V. (1994). Potential field tilt a new concept for location of potential field sources. Journal of applied Geophysics, 32(2-3), 213-217.

Mohr, P. (1962). The Ethiopian Rift system. U.S Geological Survey Washington, 33-62.

Mohr, P., & Zanettin, B. (1988). The Ethiopian flood basalt province. Continental flood basalts, 63-110.

Muzaffer, Ö., & Dikmen, Ü. (2013). Edge Detection of Magnetic Sources Using Enhanced Total Horizontal Derivative of the Tilt Angle. Yerbilimleri 34(1), 73-82.

Naheem, S., Saminu, O., Muyiwa, M., & Yusuf., T. (2019). Geophysical inversion of geologic structures of Oyo Metropolis, Southwestern Nigeria from airborne magnetic data. Geomechanics and Geophysics for Geo-Energy and Geo-Resources, 5(2), 143-157.

Niwas, S., & Singhal, D. (1981). Estimation of aquifer transmissivity from Dar-Zarrouk parameters in porous media. Journal of Hydrology, 50, 393-399.

Ojoawo, A. I., & Adagunodo, T. A. (2023). Groundwater occurrence and flow in varying geological formations. In IOP Conference Series: Earth and Environmental Science,1-10.

Okiongbo, K., & Oborie, E. (2015). Investigation of relationships between geoelectric and hydraulic parameters in a quaternary alluvial aquifer in Yenagoa, Southern Nigeria. Ife Journal of Science, 17(1), 163-172.

Onawola, B., Olatunji, S., Ologe, O., & Jimoh, R. (2021). Determination of aquifer parameters from resistivity data: A case of University of Ilorin Campus. Tanzania Journal of Science,, 47, 91-103.

Pandey, L. M. (2015). Electrical resistivity of sandy soil with water, leachates and seawater,1-92.

Parasnis, D. S. (2012). Principles of applied geophysics Springer Science & Business Media, 1-402.

Richards, M. A., Duncan, R. A., & Courtillot, V. E. (1989). Flood basalts and hot-spot tracks: plume heads and tails. Science, 246(4926), 103-107.

Rigbe Tsegaye. (2021). Hydrogeology and Major Ion Hydro-Geo-Chemistry of Borkena River Catchment, Awash Basin, Ethiopia Addis Ababa University.

Roest, W. R., Verhoef, J., & Pilkington, M. (1992). Magnetic interpretation using the 3-D analytic signal. Geophysics, 57(1), 116-125.

Rusman, M. N., Alawiyah, S., & Gunawan, I. (2023). Study on the Significance of Reduction to the Equator (RTE), Reduction to the Pole (RTP), and Pseudogravity in Magnetic Data Interpretation. Jurnal Penelitian Pendidikan IPA, 9(8), 6197-6205.

Sahuquillo, A. (2009). Conjunctive use of surface water and groundwater In Encyclopedia of Life Support Systems (EOLSS), Developed under the Auspices of UNESCO, 3, 1- 6.

Salawu, N. B., Olatunji, S., Adebiyi, L. S., Olasunkanmi, N. K., & Dada, S. S. (2019). Edge detection and magnetic basement depth of Danko area, northwestern Nigeria, from low-latitude aeromagnetic anomaly data. SN Applied Sciences, 1, 1- 9.

Satiawan, S. (2009). Aplikasi Kontinuasi Ke Atas dan Filter Panjang Gelombang untuk Pemisahan Anomali Regional-Residual Pada Data Geomagnetik. Tugas Akhir.

Senthilkumar, M., Arumugam, R., Gnanasundar, D., C Thambi, D. S., & Kumar, E. S. (2015). Effects of geological structures on groundwater flow and quality in hardrock regions of northern Tirunelveli district, southern India Journal of Earth System Science, 124(2), 405-418.

Shiklomanov, I. A., & Rodda, J. C. (2003). World water resources at the beginning of the twenty-first century. Cambridge University Press.

Singh, K. P. (2005). Nonlinear estimation of aquifer parameters from surficial resistivity measurements. 917-938. Hydrology and Earth System Sciences Discussions 2(3), 917-938.

Soupios, P. M., Kouli, M., Vallianatos, F., Vafidis, A., & Stavroulakis, G. (2007). Estimation of aquifer hydraulic parameters from surficial geophysical methods: A case study of Keritis Basin in Chania (Crete–Greece). Journal of Hydrology, 338(1-2), 122-131.

Tadesse Alemu, Abdelsalam, M., Enkurie Dawit, Balemwal Atnafu & Mickus, K. L. (2018). The Paleozoic – Mesozoic Mekele Sedimentary Basin in Ethiopia. Journal of African Earth Sciences, 143, 40-58.

Telford, W. M., Geldart, L. P., & Sheriff, R. E. (1990). Applied geophysics. Cambridge university press.

Tilahun Azagegn, Asfawossen Asrat, Tenalem Ayenew & Seifu Kebede. (2015). Litho-structural control on interbasin groundwater transfer in central Ethiopia. Journal of African Earth Sciences, 101, 383-395.

Valenta, J. (2015). Introduction to geophysics–lecture notes. Czech Republic Development Cooperation,1- 62.

Verduzco, B., Fairhead, J. D., Green, C. M., & MacKenzie, C. (2004). New insights into magnetic derivatives for structural mapping. The leading edge, 23(2), 116-119.

Vsevolozhsky, V. (2003). Groundwater in sedimentary, metamorphic and volcanic rocks. Hydrological cycle, 4, 118-127.

Zanettin, B., Gregnanin, A., Justin Visentin, E., Morbidelli, M., & Piccirillo, E. (1974). Geological and petrological researches on the volcanics of central Ethiopia. N Jb Geol Palaont Mh H, 9, 567-574.

Zanettin, B., Justin-Visentin, E., & Piccirillo, E. (1978). Volcanic succession, tectonics and magmatology in central Ethiopia. Soc. cooper. tipogr.

Zwaan, F., Corti, G., Sani, F., Keir, D., Muluneh, A. A., Illsley-Kemp, F., & Papini, M. (2020). Structural Analysis of the Western Afar Margin, East Africa: Evidence for Multiphas Rotational Rifting. Tectonics, 39(7), 1- 25.

ANNEXES

Monthly precipitation data from the National Meteorological Agency for the Harbu station.

Year	Jan	Feb	Mar	Apr	May	Jun	Jul	Aug	Sep	Oct	Nov	Dec	sum
2000	0	0	0	0	0	0	0	0	174	0	25	62.7	261.7
2001	0	36.2	299.8	34.8	59.2	28	610.6	445.4	91.6	14.8	0	20	1640.4
2002	137.1	13.4	124.4	114.2	2	2.1	0	331.4	144.4	11	0	95.4	975.4
2003	18.6	21.3	95.6	209.3	0	31.3	184	357.3	163	0	3.2	65.6	1149.2
2004	12.1	8.6	58.6	138.7	16.2	31.5	202.4	209.9	77.8	29.5	33.7	3.5	822.5
2005	18.5	18.9	95.4	87.5	104.6	9.7	352.3	249.5	44.3	26	24.6	0	1031.3
2006	9.9	10	118.7	82.7	30.1	40	287.4	297.8	99.3	21.8	7.3	0	1005
2007	21.9	45.9	83.9	70.3	10.8	18.7	364	174.9	96.6	41.9	5.1	0	934
2008	24.4	0	0	60.6	56.1	32.2	247.7	146.5	111.1	67.5	68.4	0	814.5
2009	20.2	4.9	10.5	7.2	0		286.5	228.2	59.1	64.4	14.8	292	987.8
2010	0.6	62.6	104.2	137	95.2	4.2	219.5	490.6	33.2	0	63.6	0	1210.7
2011	0	0	67.5	68.8	106.8	37.1	159.3	213.6	86	0	61.3	0	800.4
2012	0	0	145.8	154.9	74.6	55.5	418.1	300.7	50.4	0	0	0	1200
2013	0	0	176.9	65.8	29.5	0	246		130.4	0	0	0	648.6
2014	0	0	78	51.8	34.9	0	158.1	199.5	157.8	0	0	0	680.1
2015	0	0	34.8	0	44.1	0	0	365.6	58.4	0	0	0	502.9
2016	4.2	13	33.5	133.2	10.2	123.2		324.1	42.4	0	28.8	0	712.6
2017	0	57	0	186.7	45	0	332.7	445.5	286.2	19	0	13	1385.1
2018	6	112	52	131.9	17	139	283	223.4	46	52	38	0	1100.3
2019	0	71	24	0	0	0	0	0	145	0	0	0	240
2020	5	14	70	76	58	6	207	258	76	0	0	0	770
2021	88.3	0	0	452.9	0	0	0	0	0	0	0	0	541.2
2022	0	0	0	0	0	0	0	347.5	73.8	51.4	8	0	480.7
2023	6.3	75.6	217.7	171.2	261.3	92.6	149.7	189.3	62.8	0	0	0	1226.5
Average	15.54583	23.51667	78.80417	101.4792	43.98333	28.3087	204.7087	252.1174	96.23333	16.6375	15.90833	23.00833	

Monthly maximum temperature data from the National Meteorological Agency for the Harbu station.

Year	Jan	Feb	Mar	Apr	May	Jun	Jul	Aug	Sep	Oct	Nov	Dec
2000	0	0	0	0	0	0	0	0	30	0	28	28.3
2001	26.2	29.3	28.8	31.8	33.6	33.3	29.9	27.7	28.8	28.6	25.6	26.9
2002	26.2	28.8	29	31.4	33.3	34.2	0	30.8	29.7	30.4	30	27.6
2003	26.8	30.5	30.4	31	33.7	34.8	31.9	29.5	30.1	29.8	29.6	28.3
2004	30.4	29.6	31	31.1	35.5	35.5	33.2	31.3	30.7	30.1	30.1	29.3
2005	29.6	30.8	31.4	31	31	33.7	31.9	31.3	31	30.7	30.9	29.7
2006	31.3	31.2	31.2	30.5	33.5	35.3	31.9	29.6	29.9	30	29.5	0
2007	27.8	30.5	32.7	32.6	35.1	35.7	31.5	30.9	30.8	30.1	29.3	29.1
2008	29.9	29.9	33	32.8	34	35.4	32.3	31	31.3	31.5	29.3	29.2
2009	28.8	30.6	32.1	33.5	34.7	0	32.4	32.4	32	30.2	29.4	30.8
2010	31.4	30.7	31.8	32.8	32.9	33.8	33.7	32.1	29.4	30.7	30.9	30.5
2011	30.8	31	32	33.8	33.1	33.9	34	31.9	31.3	30.3	30	30.1
2012	30.7	31.1	31.7	30.8	33.2	34.1	31.6	31.1	31.4	30.7	31.3	31.6
2013	31.3	31.9	33.9	32.3	36.3	36.2	34	0	31.7	31.8	31.2	30.9
2014	30.8	31	33.1	33.1	33.1	33.7	34.4	34	33.7	31.5	30.9	30.7
2015	31.8	32.4	33.9	34.6	35.1	36.4	36.3	35	32.6	32.2	33.2	32.6
2016	32.2	32.5	32.9	32.1	32.1	32.1	32.5	33.7	33.9	34.5	33.6	32.1
2017	28.7	28.8	32.1	32.5	33.1	34.5	33.3	29.9	26.4	24.4	23.7	22.9
2018	22.9	24	27	25	24.6	26.3	24.8	23.1	23.6	20.5	20.6	18.1
2019	20.2	21.5	22.7	0	0	0	0	0	24.5	0	0	0
2020	21	21.2	24.2	25.4	28.4	28.2	23.4	24.1	23.9	22.7	23.7	0
2021	25.1	25.1	26	25.2	0	0	0	0	0	0	0	0
average	26.99545	27.83636	29.13182	28.33182	28.46818	27.59545	26.04545	24.97273	28.48636	25.48636	26.4	23.57727

VES curves

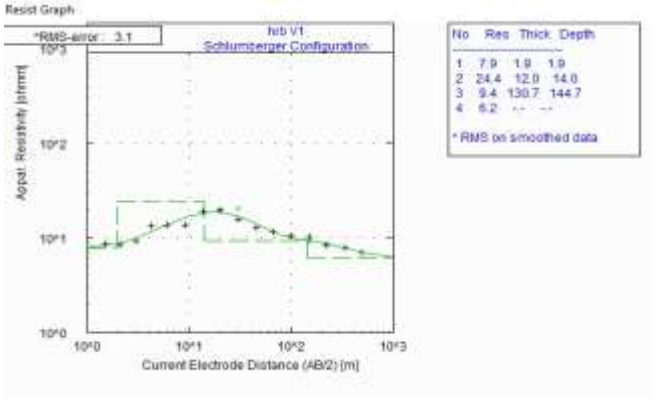
Resist Graph
*RMS-error : 3.1
hrb V1
Schlumberger Configuration
Appar. Resistivity [ohmm]
Current Electrode Distance (AB/2) [m]
No Res Thick Depth
1 7.9 1.9 1.9
2 24.4 12.0 14.0
3 9.4 130.7 144.7
4 6.2 -- --
* RMS on smoothed data

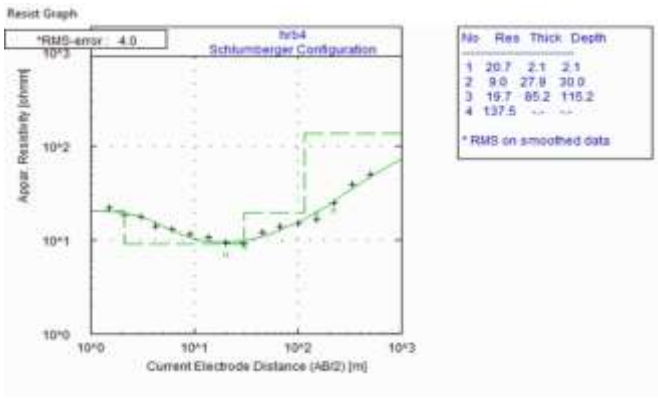
Resist Graph
*RMS-error : 4.0
hrb4
Schlumberger Configuration
Appar. Resistivity [ohmm]
Current Electrode Distance (AB/2) [m]
No Res Thick Depth
1 20.7 2.1 2.1
2 9.0 27.9 30.0
3 19.7 85.2 115.2
4 137.5 -- --
* RMS on smoothed data

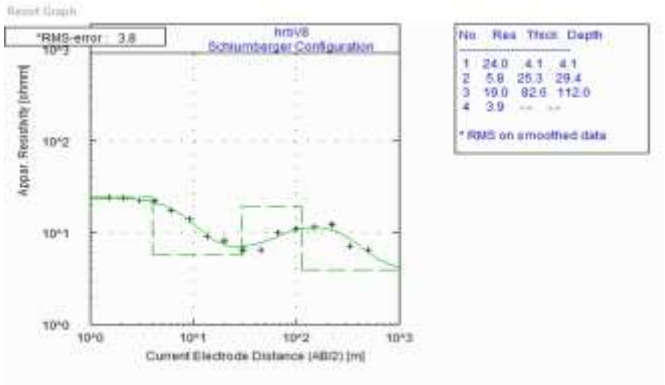
*RMS-error : 3.8
hrbV8
Schlumberger Configuration
Appar. Resistivity [ohmm]
Current Electrode Distance (AB/2) [m]
No Res Thick Depth
1 24.0 4.1 4.1
2 5.8 25.3 29.4
3 19.0 82.6 112.0
4 3.9 -- --
* RMS on smoothed data

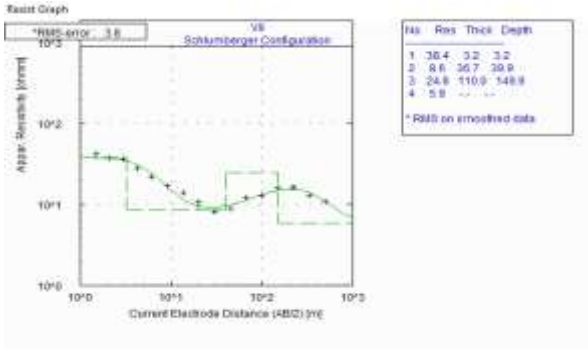
Resist Graph
*RMS-error : 3.8
V8
Schlumberger Configuration
Appar. Resistivity [ohmm]
Current Electrode Distance (AB/2) [m]
No Res Thick Depth
1 38.4 3.2 3.2
2 8.6 36.7 39.9
3 24.8 110.9 148.8
4 5.8 -- --
* RMS on smoothed data

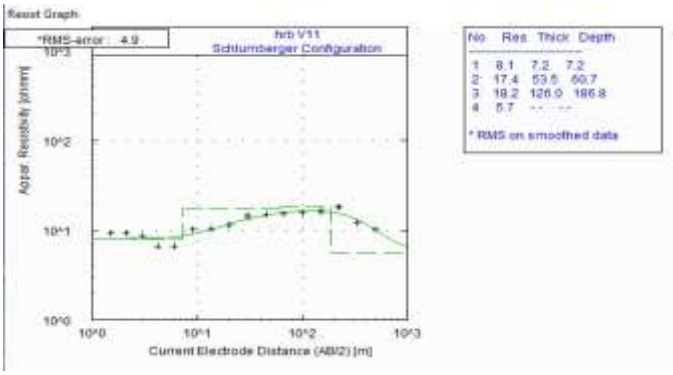
Resist Graph
*RMS-error : 4.9
hrb V11
Schlumberger Configuration
Appar. Resistivity [ohmm]
Current Electrode Distance (AB/2) [m]
No Res Thick Depth
1 8.1 7.2 7.2
2 17.4 53.5 60.7
3 18.2 126.0 186.8
4 5.7 -- --
* RMS on smoothed data

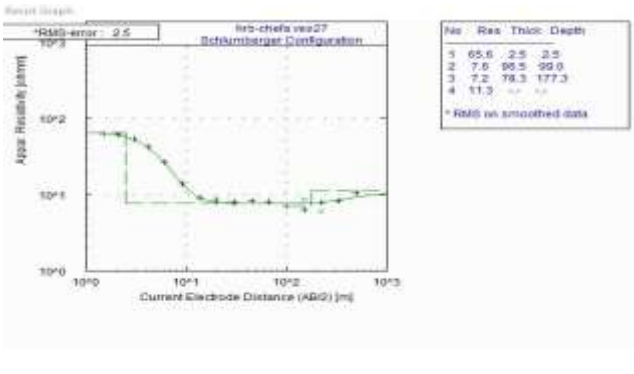
*RMS-error : 2.5
hrb-chefa ves27
Schlumberger Configuration
Appar. Resistivity [ohmm]
Current Electrode Distance (AB/2) [m]
No Res Thick Depth
1 65.6 2.5 2.5
2 7.6 96.5 99.0
3 7.2 78.3 177.3
4 11.3 -- --
* RMS on smoothed data

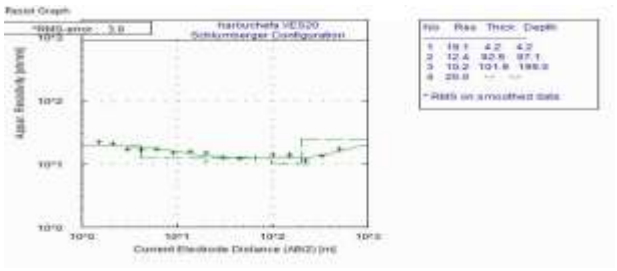
Resist Graph
*RMS-error : 3.9
Schlumberger Configuration
Apparr Resistivity [ohmm]
Current Electrode Distance (AB/2) [m]
No Res Thick Depth
1 19.1 4.2 4.2
2 12.4 92.8 97.1
3 19.2 101.8 198.9
4 28.8 -- --
* RMS on smoothed data

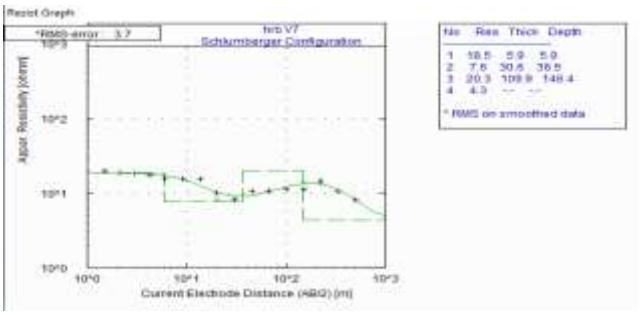
Resist Graph
*RMS-error : 3.7
Schlumberger Configuration
Apparr Resistivity [ohmm]
Current Electrode Distance (AB/2) [m]
No Res Thick Depth
1 18.5 5.9 5.9
2 7.6 30.6 36.5
3 20.3 109.9 146.4
4 4.3 -- --
* RMS on smoothed data

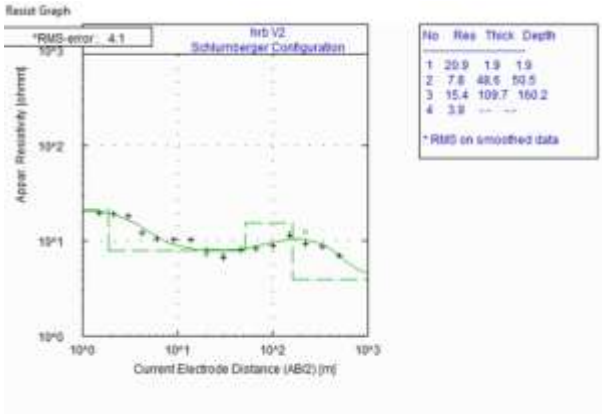
Resist Graph
*RMS-error : 4.1
Schlumberger Configuration
Apparr Resistivity [ohmm]
Current Electrode Distance (AB/2) [m]
No Res Thick Depth
1 20.9 1.9 1.9
2 7.8 48.6 50.5
3 15.4 109.7 160.2
4 3.9 -- --
* RMS on smoothed data

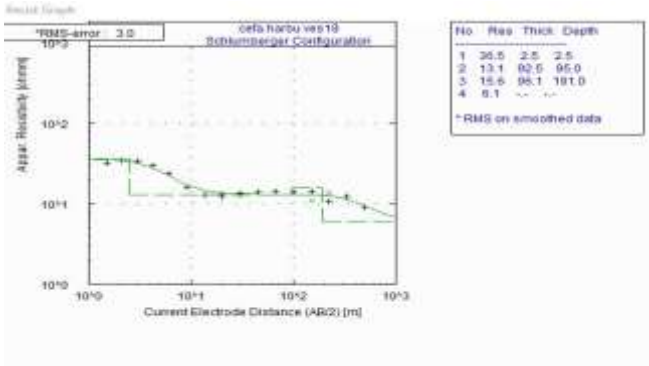
*RMS-error : 3.0
Schlumberger Configuration
Apparr Resistivity [ohmm]
Current Electrode Distance (AB/2) [m]
No Res Thick Depth
1 36.5 2.5 2.5
2 13.1 82.5 85.0
3 15.6 96.1 181.0
4 6.1 -- --
* RMS on smoothed data

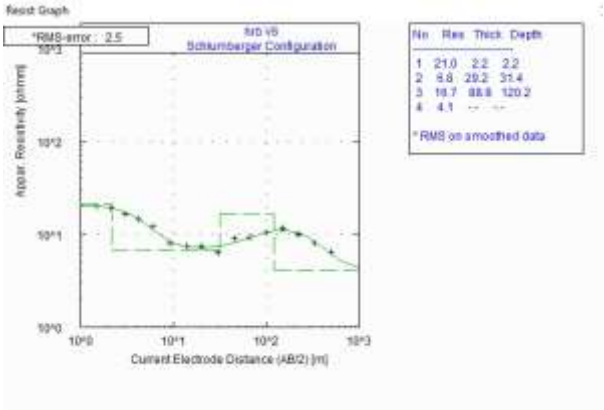
Resist Graph
*RMS-error : 2.5
Schlumberger Configuration
Apparr Resistivity [ohmm]
Current Electrode Distance (AB/2) [m]
No Res Thick Depth
1 21.0 2.2 2.2
2 6.8 29.2 31.4
3 16.7 88.8 120.2
4 4.1 -- --
* RMS on smoothed data